The COS Legacy Archive Spectroscopy Survey (CLASSY) Treasury Atlas

Danielle A. Berg, Bethan L. James, Teagan King, Meaghan Mcdonald, Zuyi Chen, John Chisholm, Timothy Heckman, Crystal L. Martin, Dan P. Stark, Alessandra Aloisi, et al.

The Astrophysical Journal Supplement Series, 261:31 (41pp), 2022 August https://doi.org/10.3847/1538-4365/ac6c03

The COS Legacy Archive Spectroscopy Survey (CLASSY) Treasury Atlas*

Danielle A. Berg[1], Bethan L. James[2], Teagan King[3], Meaghan McDonald[3], Zuyi Chen[4], John Chisholm[1], Timothy Heckman[5], Crystal L. Martin[6], Dan P. Stark[4], and Alessandra Aloisi[3], Ricardo O. Amorín[7,8], Karla Z. Arellano-Córdova[1], Matthew Bayliss[9], Rongmon Bordoloi[10], Jarle Brinchmann[11], Stéphane Charlot[12], Jacopo Chevallard[12], Ilyse Clark[1], Dawn K. Erb[13], Anna Feltre[14], Max Gronke[15], Matthew Hayes[16], Alaina Henry[3,5], Svea Hernandez[2], Anne Jaskot[17], Tucker Jones[18], Lisa J. Kewley[19,20], Nimisha Kumari[2], Claus Leitherer[3], Mario Llerena[7], Michael Maseda[21], Matilde Mingozzi[3], Themiya Nanayakkara[22], Masami Ouchi[23,24,25], Adele Plat[4], Richard W. Pogge[26,27], Swara Ravindranath[3], Jane R. Rigby[28], Ryan Sanders[18], Claudia Scarlata[29], Peter Senchyna[30], Evan D. Skillman[29], Charles C. Steidel[31], Allison L. Strom[32], Yuma Sugahara[23,24,33], Stephen M. Wilkins[34], Aida Wofford[35], and Xinfeng Xu[5]
(The CLASSY Team)
[1] Department of Astronomy, The University of Texas at Austin, 2515 Speedway, Stop C1400, Austin, TX 78712, USA; daberg@austin.utexas.edu
[2] AURA for ESA, Space Telescope Science Institute, 3700 San Martin Drive, Baltimore, MD 21218, USA
[3] Space Telescope Science Institute, 3700 San Martin Drive, Baltimore, MD 21218, USA
[4] Steward Observatory, The University of Arizona, 933 N Cherry Avenue, Tucson, AZ 85721, USA
[5] Center for Astrophysical Sciences, Department of Physics & Astronomy, Johns Hopkins University, Baltimore, MD 21218, USA
[6] Department of Physics, University of California, Santa Barbara, Santa Barbara, CA 93106, USA
[7] Instituto de Investigación Multidisciplinar en Ciencia y Tecnología, Universidad de La Serena, Raul Bitrán 1305, La Serena 2204000, Chile
[8] Departamento de Astronomía, Universidad de La Serena, Av. Juan Cisternas 1200 Norte, La Serena 1720236, Chile
[9] Department of Physics, University of Cincinnati, Cincinnati, OH 45221, USA
[10] Department of Physics, North Carolina State University, 421 Riddick Hall, Raleigh, NC 27695-8202, USA
[11] Instituto de Astrofísica e Ciências do Espaço, Universidade do Porto, CAUP, Rua das Estrelas, PT4150-762 Porto, Portugal
[12] Sorbonne Université, UPMC-CNRS, UMR7095, Institut d'Astrophysique de Paris, F-75014, Paris, France
[13] Center for Gravitation, Cosmology and Astrophysics, Department of Physics, University of Wisconsin Milwaukee, 3135 N Maryland Avenue, Milwaukee, WI 53211, USA
[14] INAF–Osservatorio di Astrofisica e Scienza dello Spazio di Bologna, Via P. Gobetti 93/3, I-40129 Bologna, Italy
[15] Max Planck Institut fur Astrophysik, Karl-Schwarzschild-Straße 1, D-85748 Garching bei München, Germany
[16] Stockholm University, Department of Astronomy and Oskar Klein Centre for Cosmoparticle Physics, AlbaNova University Centre, SE-10691, Stockholm, Sweden
[17] Department of Astronomy, Williams College, MA, USA
[18] University of California, Davis, CA, USA
[19] Research School of Astronomy and Astrophysics, Australian National University, Cotter Road, Weston Creek, ACT 2611, Australia
[20] ARC Centre of Excellence for All Sky Astrophysics in 3 Dimensions (ASTRO 3D), Canberra, ACT 2611, Australia
[21] Department of Astronomy, University of Wisconsin-Madison, 475 N Charter Street, Madison, WI 53706 USA
[22] Swinburne University of Technology, Melbourne, Victoria, Australia
[23] National Astronomical Observatory of Japan, 2-21-1 Osawa, Mitaka, Tokyo 181-8588, Japan
[24] Institute for Cosmic Ray Research, The University of Tokyo, Kashiwa-no-ha, Kashiwa 277-8582, Japan
[25] Kavli Institute for the Physics and Mathematics of the Universe (WPI), University of Tokyo, Kashiwa, Chiba 277-8583, Japan
[26] Department of Astronomy, The Ohio State University, 140 W 18th Avenue, Columbus, OH 43210, USA
[27] Center for Cosmology & AstroParticle Physics, The Ohio State University, 191 W Woodruff Avenue, Columbus, OH 43210, USA
[28] Observational Cosmology Lab, Code 665, NASA Goddard Space Flight Center, 8800 Greenbelt Rd, Greenbelt, MD 20771, USA
[29] Minnesota Institute for Astrophysics, University of Minnesota, 116 Church Street SE, Minneapolis, MN 55455, USA
[30] Carnegie Observatories, 813 Santa Barbara Street, Pasadena, CA 91101, USA
[31] Cahill Center for Astronomy and Astrophysics, California Institute of Technology, MC249-17, Pasadena, CA 91125, USA
[32] Department of Astrophysical Sciences, 4 Ivy Lane, Princeton University, Princeton, NJ 08544, USA
[33] Waseda Research Institute for Science and Engineering, Faculty of Science and Engineering, Waseda University, 3-4-1, Okubo, Shinjuku, Tokyo 169-8555, Japan
[34] Astronomy Centre, University of Sussex, Falmer, Brighton BN1 9QH, UK
[35] Instituto de Astronomía, Universidad Nacional Autónoma de México, Unidad Académica en Ensenada, Km 103 Carr. Tijuana-Ensenada, Ensenada 22860, Mexico
Received 2021 October 3; revised 2022 February 16; accepted 2022 February 17; published 2022 July 27

Abstract

Far-ultraviolet (FUV; ∼1200–2000 Å) spectra are fundamental to our understanding of star-forming galaxies, providing a unique window on massive stellar populations, chemical evolution, feedback processes, and reionization. The launch of the James Webb Space Telescope will soon usher in a new era, pushing the UV spectroscopic frontier to higher redshifts than ever before; however, its success hinges on a comprehensive

* Based on observations made with the NASA/ESA Hubble Space Telescope, obtained from the Data Archive at the Space Telescope Science Institute, which is operated by the Association of Universities for Research in Astronomy, Inc., under NASA contract NAS 5-26555.

understanding of the massive star populations and gas conditions that power the observed UV spectral features. This requires a level of detail that is only possible with a combination of ample wavelength coverage, signal-to-noise, spectral-resolution, and sample diversity that has not yet been achieved by any FUV spectral database. We present the Cosmic Origins Spectrograph Legacy Spectroscopic Survey (CLASSY) treasury and its first high-level science product, the CLASSY atlas. CLASSY builds on the Hubble Space Telescope (HST) archive to construct the first high-quality ($S/N_{1500\,Å} \gtrsim 5$/resel), high-resolution ($R \sim 15{,}000$) FUV spectral database of 45 nearby ($0.002 < z < 0.182$) star-forming galaxies. The CLASSY atlas, available to the public via the CLASSY website, is the result of optimally extracting and coadding 170 archival+new spectra from 312 orbits of HST observations. The CLASSY sample covers a broad range of properties including stellar mass ($6.2 < \log M_\star(M_\odot) < 10.1$), star formation rate ($-2.0 < \log$ SFR $(M_\odot\ \mathrm{yr}^{-1}) < +1.6$), direct gas-phase metallicity ($7.0 < 12+\log(O/H) < 8.8$), ionization ($0.5 < O_{32} < 38.0$), reddening ($0.02 < E(B-V) < 0.67$), and nebular density ($10 < n_e\ (\mathrm{cm}^{-3}) < 1120$). CLASSY is biased to UV-bright star-forming galaxies, resulting in a sample that is consistent with the $z \sim 0$ mass–metallicity relationship, but is offset to higher star formation rates by roughly 2 dex, similar to $z \gtrsim 2$ galaxies. This unique set of properties makes the CLASSY atlas the benchmark training set for star-forming galaxies across cosmic time.

Unified Astronomy Thesaurus concepts: Galaxies (573); Ultraviolet surveys (1742); Emission line galaxies (459); Interstellar line absorption (843); Lyman-alpha galaxies (978); High-redshift galaxies (734)

Supporting material: figure set, machine-readable tables

1. Introduction

The interplay between gas and stars is one of the most fundamental, yet unsettled, drivers of galactic evolution. In the basic picture, gas is accreted onto galaxies from the cosmic web, settles into their gravitational wells, and is converted into stars. The massive stars in star-forming galaxies ionize the surrounding gas, producing nebular emission and driving outflows and radiative shocks. Such feedback drives chemical evolution and can modulate or limit accretion processes, thereby regulating the subsequent growth of galaxies. The far-ultraviolet (FUV), defined here as ∼1200–2000 Å, is arguably the richest wavelength regime in diagnostic spectral features characterizing these processes and will provide an important window onto the first generation of galaxies in the forthcoming era of extremely large telescopes (ELTs) and the James Webb Space Telescope (JWST).

1.1. The Need for a Benchmark FUV Spectral Atlas

While the full FUV spectrum is rich in diagnostic power, studies have thus far largely focused on specific and individual components of the galaxy evolution puzzle. As a result of differing requirements of various studies, the archive has been a piecemeal collection, missing significant pieces that reside in different parts of the FUV spectrum. This incompleteness has prevented us from understanding the interdependent nature of the physical processes in star-forming galaxies and their UV spectroscopic properties. Recently, the spectroscopic studies of $2 < z < 4$ star-forming galaxies have emerged as our most comprehensive rest-FUV spectral data sets (e.g., Rigby et al. 2018; Steidel et al. 2016). Of particular importance to developing a detailed understanding of UV emission lines has been the large-sample VUDS (e.g., Le Fèvre et al. 2015), VANDELS (e.g., McLure et al. 2018), and MUSE (e.g., Schmidt et al. 2021) surveys. However, the proper tool set to interpret these rich data sets has been lacking.

A scientifically useful FUV spectral atlas requires three components. First, it must have broad wavelength coverage to simultaneously probe the continuum, absorption, and emission features that characterize the stellar populations and gas of the galaxy. Second, theory predicts that the velocities of galactic outflows scale with the circular velocities of their host galaxies (e.g., Murray et al. 2005). This means that very high spectral resolution ($R > 10{,}000$ or velocity resolution less than 30 km s^{-1}) is required to measure the impact of stellar feedback in galaxies with low stellar-mass (see, e.g., McGaugh et al. 2001). Third, spectra with high signal-to-noise ratios (S/N) in the continuum are needed to measure faint features.

There are several existing compilations of FUV spectra of local star-forming galaxies. These collections include the Kinney et al. (1993) atlas, which is perhaps the most impactful FUV atlas to date, of 143 star-forming and active galaxies observed with the International Ultraviolet Explorer (IUE), the Leitherer et al. (2002) atlas of 19 galaxies observed with the 0.9 m Hopkins Ultraviolet Telescope (HUT), the Grimes et al. (2009) atlas of 16 galaxies with archival Far Ultraviolet Spectroscopic Explorer Spectrograph (FUSE) spectra, and the Leitherer et al. (2011) atlas of 28 galaxies observed with the Goddard High Resolution Spectrograph (GHRS) and the Faint Object Spectrograph (FOS). Unfortunately, each of these atlases is limited by the properties of the UV spectrograph used and so is insufficient for current science objectives.

The properties characterizing important compilations of FUV spectra are listed in Table 1 in the order of publication. While the Kinney et al. (1993) atlas is the largest and still the most impactful, the resolution (∼6 Å) and S/N (∼1) of its spectra are too low to resolve the FUV spectra features and utilize their diagnostic power. The Leitherer et al. (2002) atlas using the HUT was ground-breaking for the FUV at the time because it pushed blueward down to 912 Å, but suffered from even lower spectral resolution (∼1 Å) than the Kinney et al. (1993) atlas. In contrast, the Grimes et al. (2009) atlas was the first FUV atlas to achieve both high S/N and spectral resolution, but observed only sub-Lyα (< 1215 Å) wavelengths. Finally, the Leitherer et al. (2011) atlas made progress in combining both large-wavelength coverage and moderately high spectral resolution (0.9 Å), but only for a small subsample of 12 galaxies with GHRS observations. Sadly, the limited wavelength coverage, spectral resolution, and S/N of these past compilations are insufficient for the simultaneous study of the stellar, nebular, and outflow properties in star-forming galaxies needed to advance our understanding of galaxy evolution.

Table 1
Important Compilations of FUV Spectra

Survey Reference	No. of Gal.	z	M_B (mag)	12+ log(O/H)	Instrument/ Aperture	Mirror Diameter	Spatial Scale (pc)	Wavelength Coverage (Å)	Resol. (Å)	Ave. S/N[a]
Kinney et al. (1993)	143	−0.001–0.053	14.8–10.1	⋯	IUE/10″ × 20″	0.45 m	600–1.5 × 10^5	1150–3000	6	∼1
Leitherer et al. (2002)	19	0.001–0.029	15.0–2.8	8.0–9.3	HUT/20″[b]	0.90 m	6–1.2 × 10^4	912–1800	1	⋯
Chandar et al. (2004)	18	0.001–0.014	15.5–9.3	7.8–9.2	STIS/0.″2	2.40 m	2–49	1175–3100	1	⋯
Grimes et al. (2009)	16	0.001–0.045	17.2–2.8	7.0–9.0[c]	FUSE/4″ × 0″	0.82 m	330–1.9 × 10^5	905–1187	<0.1	8.8
Leitherer et al. (2011)	12	−0.001–0.058	18.0–2.8	7.0–9.2[c]	GHRS/2″ × 2″	2.40 m	32–756	1050–1700	0.9	6.6
⋯	17	⋯	⋯	⋯	FOS/0.″86 circ.	2.40 m	14–325	1150–5500	6.5	7.4
CLASSY/this work	45	0.002–0.182	19.8–14.8	7.0–8.8	COS/2.″5 circ.	2.40 m	87–1.1 × 10^4	1200–2000	0.1	6.4

Notes. The best FUV collections of spectra are listed here. Column (1) provides the reference for the identified survey or analysis associated with the data. For each of these samples, column (2) lists the number of galaxies, column (3) lists the redshift range, column (4) lists the B-band magnitude range, and column (5) lists the gas-phase oxygen abundance range. The remaining columns provide details of the spectral observations: column (6) names the instrument/telescope (note that STIS, GHRS, FOS, and COS were all on HST) and spectral aperture used, column (8) lists the corresponding spatial scales probed, column (9) gives the mirror diameter of those telescopes, column (10) lists the wavelength coverage, column (11) provides the resolution (at 1500 Å), and column (12) estimates the signal-to-noise ratio measured from the FUV continua of the survey spectra. Note that FUSE had 4 mirrors, so the effective diameter is listed here. If multiple resolutions were available, only the most comparable resolution mode is listed. The GHRS also had a very-high-resolution mode of $R = 100{,}000$, but was limited to observing objects brighter than 14th magnitude. Considering these characterizations, only CLASSY has the combined wavelength coverage, resolution, and signal-to-noise to study both the massive stars and the gas properties in the same galaxies.

[a] S/N given per pixel for Leitherer et al. (2011), per 0.078 Å bin for Grimes et al. (2009), and per resel for CLASSY. S/N was estimated from the average rms of the Kinney et al. (1993) templates. No S/N was provided by Leitherer et al. (2002) or Chandar et al. (2004).

[b] Note that, while a range of aperture sizes were used for the HUT observations of Leitherer et al. (2002; 12″, 20″, 32″, and 10″ × 56″), 20″ was adopted here as an average.

[c] The ranges in gas-phase oxygen abundance sampled by the Grimes et al. (2009) and Leitherer et al. (2011) surveys may be misleading owing to their inclusion of only two very-metal-poor galaxies (I Zw 18 and SBS 0335-052).

1.2. The Cosmic Origins Spectrograph

The installation of the Cosmic Origins Spectrograph (COS) on the Hubble Space Telescope (HST) in 2009 May during Servicing Mission 4 ushered in a new era of higher-sensitivity FUV spectroscopy. It is optimally designed for moderate-resolution UV spectroscopy of faint point sources with a resolving power of $R \sim 15{,}000$ and a FUV spectroscopy channel covering approximately 900–2000 Å. Not only does COS have excellent FUV wavelength coverage and resolution, as shown in Table 1, it also benefits from superior FUV sensitivity over all previous FUV spectrographs. In fact, COS boasts more than 30 times the sensitivity of the Space Telescope Imaging Spectrograph (STIS) for FUV observations of faint objects, allowing its spectroscopic observations to unify the study of FUV stellar and gas-phase properties in a way that would not be possible with STIS[36] or any other past FUV spectrograph.

While COS has been used widely to observe many samples of star-forming galaxies and has enabled key scientific discoveries, it lacks a high caliber atlas in the class of those discussed above. This is due in large part to the piecemeal nature of the current archive, which, as a result, suffers from a variety of deficiencies. For one, archival COS data usually cover only a portion of the FUV owing to the diversity of science goals, the competitive nature of HST, and the narrow wavelength coverage of the individual medium-resolution gratings (∼300 Å). In addition, strong stellar features and interstellar absorption lines are more concentrated in the bluer end of the FUV, while strong emission lines are clustered in the redder portion of the FUV. Consequently, it is impossible to fully connect the properties of the gas and stars within a single-grating spectrum of a given galaxy. Second, the S/N in the continuum, and/or the resolution of archival COS spectra is often too low to accurately measure the interstellar medium (ISM) absorption or stellar features. For example, there are ample programs of low-resolution G140L grating spectra that offer more efficient exposure times over the higher-resolution gratings, but data taken with G140L do not have sufficient spectral resolution to characterize the kinematics of the gas or disentangle the multicomponent emission and absorption features. Third, the highest S/N FUV HST spectra come from nearby galaxies, which can suffer the consequences of foreground Milky Way absorption lines contaminating those intrinsic to a galaxy.

These problems are illustrated by the state of the Hubble Spectral Legacy Archive (HSLA; Peeples et al. 2017), which "provides the community with all raw and associated combined spectra for COS FUV data publicly available in MAST." In the 2018 July HSLA release, the number of nearby ($z < 0.3$) galaxies with high-S/N ($\gtrsim$5 per 100 km s^{-1} resolution element) FUV COS spectroscopy totaled only 101. Of these, only 37 galaxies had observations with more than one grating setting, and poignantly, only two had full FUV 1200–2000 Å coverage.

1.3. The CLASSY Treasury

Here we present the COS Legacy Archive Spectroscopic Survey (CLASSY) as the first high-S/N (>5), high-resolution ($R \sim 15{,}000$) FUV COS spectral atlas of star-forming galaxies. CLASSY fills in the fundamental gaps in the 1200–2000 Å FUV range that will achieve a holistic view of star-forming galaxies and enhance the legacy and utility of the COS archive.

CLASSY combines 135 orbits of new HST data with 177 orbits of archival HST data, for a total of 312 orbits, to complete the first atlas of high-quality rest-FUV COS spectra of 45 local star-forming galaxies. In order to achieve nearly

[36] Note, however, that STIS offers other capabilities over COS. Specifically, STIS has narrow slit settings available that offer higher spatial sampling than COS and optical gratings that provide redder wavelength coverage (1635–10137 Å) than COS (913–3560 Å).

panchromatic FUV spectral coverage with the highest spectral resolution possible, CLASSY efficiently augments the existing archival data with new HST/COS observations, uniting the high-resolution G130M, G160M, and G185M gratings for a sample of galaxies spanning broad parameter space. As a result, CLASSY provides a well-controlled local FUV sample with the requisite sensitivity and spectral resolution to enable the synergistic studies of stars and gas within the *same* galaxies. The rest-FUV coverage of the CLASSY data provides a diversity of spectral features with unparalleled diagnostic power. With a wavelength range of roughly 1200–2000 Å, the CLASSY spectra cover many emission and absorption features important for characterizing the ionizing stellar populations (e.g., metallicity, age), the properties of gas flows (velocities, column densities, ionization phases), and the physical conditions of the multiphase interstellar gas (e.g., metallicity, temperature, ionization) within the same galaxies.

The CLASSY atlas is the benchmark training set for star-forming galaxies across cosmic time, including the earliest galaxies that will be observed with the eminent JWST and the next generation of ELTs. Therefore, CLASSY will provide a number of state-of-the-art data products to the astronomical community via the Mikulski Archive for Space Telescopes (MAST) and HSLA to ensure their enduring value and utility. The primary data products are the high-resolution, high-S/N coadded multigrating FUV spectral templates of the CLASSY sample of 45 star-forming galaxies presented here. Additional planned data products include stellar continuum fits, nebular abundance measurements, improved UV emission line diagnostics, feedback properties, radiative transfer models, and more. With these high-level science products (HLSPs), the CLASSY Treasury will complete the vital picture that is needed to diagnose the suite of star-forming galaxy properties that will be offered to us in the next decade. Given the uncertain future of observed-frame UV capabilities, the CLASSY templates and models embody an indispensable toolset.

Here we present Paper I of the CLASSY Treasury detailing the release of the first HLSP: the CLASSY coadded spectral atlas. In Section 2, we introduce the CLASSY atlas of FUV and optical spectra. We describe the sample selection in Section 2.1, the HST/COS spectroscopic observations and coaddition process in Section 2.2, and the ancillary optical spectra in Section 2.3. The details of the coadded spectra data release are described in Section 3, including the coadded spectra file format (Section 3.1), digital access to the resulting data release (Section 3.2) for ease of utility, and a comparison to previous FUV surveys in (Section 3.3). In order to give a general overview of the CLASSY galaxies and their spectra, we discuss the optical measurements of their host galaxy properties in Section 4. Specifically, we revisit the ancillary optical spectra used in Section 4.1, the emission line measurements (Section 4.2) and their reddening corrections (Section 4.3), and calculations of the electron densities (Section 4.4), temperatures (Section 4.4), oxygen abundances (Section 4.5), ionization parameters (Section 4.6), and stellar mass and star formation rates (SFRs; Section 4.7). The resulting global properties of the CLASSY sample are discussed in Section 5. Finally, a demonstration of the subsequent scientific studies that can be performed with CLASSY is presented in Section 6. A summary of Paper I can be found in Section 7.

We refer the reader to the appendices for additional CLASSY resources. Specifically, Appendix A contains tables of the CLASSY FUV+optical spectral observations (Tables 2 and 4). Appendix B contains tables of the CLASSY galaxy properties derived from optical spectra (Table 5) and photometry (Table 6). Appendix C discusses the details of our spectral energy distribution (SED) fitting. Appendix D compiles useful notes on individual CLASSY galaxies. Finally, Appendix E displays the CLASSY coadded spectrum for each galaxy in the sample. Note that, for consistency, the CLASSY objects are designated by an abbreviation of their sexigesimal coordinates as J`HHMM`$\pm$`DDMM`. A flat ΛCDM cosmology ($H_0 = 70$ km s^{-1} Mpc^{-1}, $\Omega_m = 0.3$) was assumed throughout this work.

2. The CLASSY Atlas of UV+Optical Spectra

The primary community data product of the CLASSY treasury is high-quality, coadded FUV plus optical spectra for the 45 star-forming galaxies in the CLASSY sample. These CLASSY spectra will enable a number of important synergistic studies between the stars and gas of galaxies that will result in additional CLASSY HLSPs (see Section 6) and an untapped wealth of potential community science investigations. Below we describe the CLASSY sample selection in Section 2.1, the HST/COS FUV observations in Section 2.2, and briefly the spectra coaddition process in Section 2.3. We refer the reader to James et al. (2022, hereafter, Paper II) for a detailed discussion of the data reduction and technical details of the coaddition process, along with best practices for COS data of extended sources.

2.1. Sample Selection

Overview. The CLASSY survey was motivated to build an atlas on the shoulders of the HST/COS archive to achieve comprehensive, high-resolution, high-S/N rest-FUV spectra of nearby ($0.002 < z < 0.182$) star-forming galaxies. Using a careful sample selection to achieve these goals, the resulting CLASSY sample spans a wide range of stellar masses ($\log M_\star \sim 6$–$10\ M_\odot$), SFR ($\log$ SFR ~ -2 to $+2\ M_\odot$ yr^{-1}), oxygen abundances (12+log(O/H) ∼ 7–9), electron densities ($n_e \sim 10^1$–10^3 cm^{-3}), and reddening values ($E(B-V) \sim 0.0$–0.7).

In order to assemble an atlas with unprecedented S/N and spectral resolution that efficiently utilizes the archive, we chose a sample of nearby, UV-bright galaxies, with existing high S/N spectra in at least one of the high-spectral-resolution gratings on HST/COS. Note that we selected spectra from a single instrument to ensure a consistent aperture. We also highlight that COS was chosen over STIS due to its higher sensitivity in the FUV. Existing archival spectra were first examined using the HSLA, from which 101 nearby ($z < 0.2$) galaxies were selected based on their high-S/N ($\gtrsim 7$ per 100 km s^{-1} resolution element) COS spectroscopy in at least one medium-resolution grating (G130M, G160M, or G185M). The following selection criteria were then implemented to ensure the efficient completion of high-quality, comprehensive rest-frame FUV spectra for a large, diverse sample of star-forming galaxies:

1. *Star-forming galaxies*. Any targets with secondary classifications of quasi-stellar object (QSO) or Seyfert in the HSLA were removed. The remaining targets were

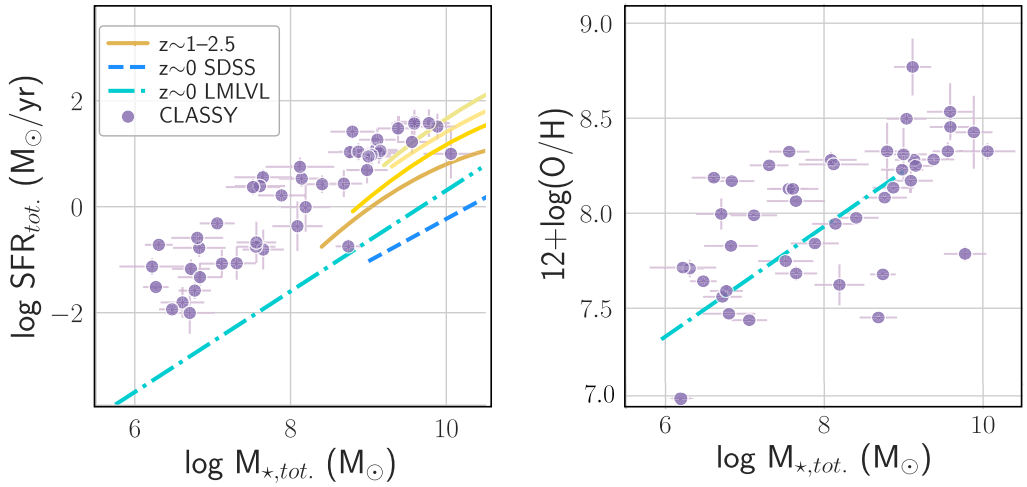

Figure 1. The CLASSY sample covers broad ranges in typical galaxy parameters, as measured from the optical spectra and UV+optical photometry (see Section 4). Property trends are plotted for the total star formation rate vs. total stellar mass (SFMR; left) and gas-phase oxygen abundance vs. total stellar mass, or the mass–metallicity relationship (MZR; right). For comparison, we plot the $z \sim 0$ trends of Chang et al. (2015; SDSS, blue dashed line) and Berg et al. (2012; LMLVL, green dotted–dashed line), as well as the $z \sim 1$–2.5 SFMR trends from Whitaker et al. (2014; yellow lines), for the SFMR, and the Berg et al. (2012; LMLVL, green dotted–dashed line) direct-metallicity trend for the MZR. Clearly the CLASSY MZR is typical of local low-mass star-forming galaxies, but the sample is offset to higher SFRs that are more typical of galaxies at cosmic noon.

visually confirmed to not have obvious broad QSO emission features.

2. *Low redshift*. Redshifts from existing optical spectra of $z < 0.2$ were required to capitalize on the FUV sensitivity of COS, which is significantly higher than the near-UV (NUV) detectors (COS and STIS), but falls off rapidly redward of 1950 Å.
3. *Compact*. Through a visual inspection of the existing HST/COS NUV acquisition images, we selected galaxies with single dominant emission regions and relatively compact morphologies in the sense that the Gaussian distribution of their NUV light had a full-width half-maximum (GFWHM) $<2\farcs5$. This ensured that the COS $2\farcs5$ aperture (optimized for point sources) will capture most of the FUV light from the galaxy. Note, however, that this is a flawed criterion, as COS UV acquisition images are vignetted, and thus the optical sizes of the CLASSY sample are significantly larger for a few galaxies.
4. *UV bright*. We required Galaxy Evolution Explorer (GALEX; GR6; Bianchi et al. 2014) FUV magnitudes of < 20 mag to allow for an efficient observing strategy, resulting in < 3 orbits per grating setting, on average.
5. *Grating efficiency*. From the HSLA, we found three galaxies that had observations of sufficient quality in all of the proposed gratings (J0337-0502, J0942+3547, and J0934+5514). Additionally, 32 galaxies had observations of sufficient quality in two of the proposed gratings, allowing their rest-frame FUV coverage to be completed with the addition of a single grating. Of these, 16 galaxies had existing G130M+G160M observations, and so CLASSY completed their FUV spectra with the addition of G185M and/or G225M observations, while the remaining 16 had G160M+G185M observations and were completed with the addition of G130M observations. Among the galaxies with only single-grating observations (G130M or G160M), we preferentially chose the five with existing high-quality G160M observations because new G130M observations are less time intensive due to the gratings' higher sensitivity.
6. *Broad parameter space coverage*. Measurements from existing optical spectra were used to select broad and efficient coverage of galaxy properties to ensure that the sample is suitable for comparison to star-forming galaxies near and far ($z < 7$): SFRs, specific SFRs (sSFRs), stellar masses, nebular metallicities, and ionization parameter. The ranges of stellar mass, SFR, and metallicity are shown in Figure 1. To better sample the higher nebular densities observed for $z > 1$ galaxies (e.g., Shirazi et al. 2014; Sanders et al. 2016; Kaasinen et al. 2017; Harshan et al. 2020) and directly study the effect of electron density on rest-FUV galaxy properties, we mined the Sloan Digital Sky Survey Data Release 12[37] (SDSS-III DR12; Eisenstein et al. 2011; Alam et al. 2015) and existing literature in order to unearth additional targets with [S II] $\lambda\lambda$6717,6731 densities of $n_e > 400$ cm^{-3}. Although such targets are extremely rare at $z \sim 0$, we were able to compile a sample of 10 galaxies in our so-called "high-density sample" that met criteria (1)–(4). Of these, five galaxies were already in our sample, while the other five had no previous HST/COS observations, and so required new G130M+G160M+G185M observation.

As a result of the search just described, the final CLASSY sample contains 45 nearby ($z < 0.2$), UV-bright ($m_{\rm FUV} < 21$ AB arcsec^{-2}), relatively compact (GFWHM$_{\rm NUV} < 2\farcs5$), galaxies. Note, however, that the COS instrument handbook defines compact objects as those having a GFWHM $< 0\farcs6$; in this sense, the CLASSY sample includes a distribution of compact to extended morphologies. For comparison, we determined the optical size of each galaxy by measuring the average half-light radius (r_{50}) from u- and g-band SDSS, the Dark Energy Survey (DES), and PanSTARRS imaging (listed in Table 6); the optical sizes are $0\farcs22$ larger on average than the UV.

[37] http://www.sdss.org/dr12/

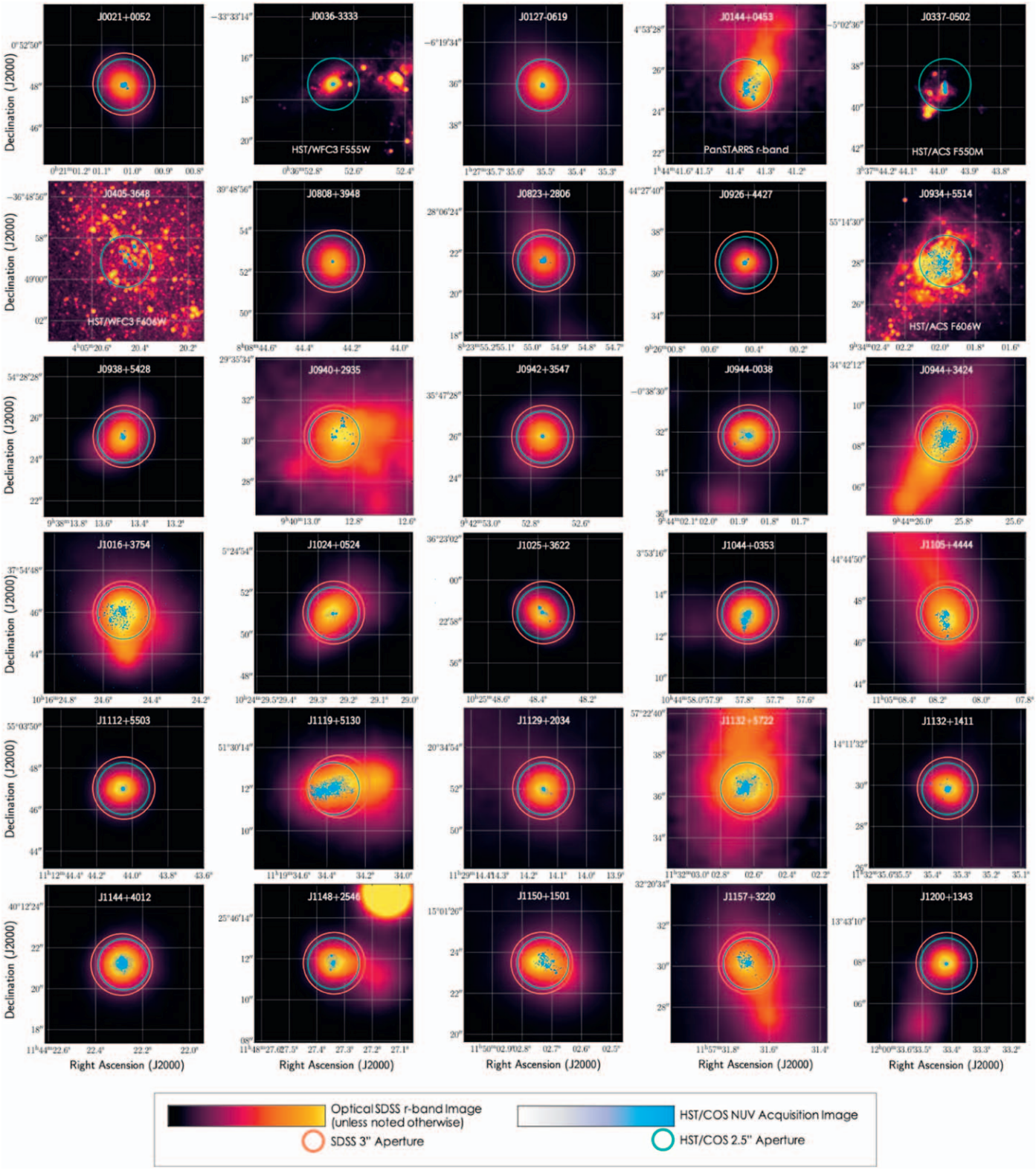

Figure 2. The HST/COS NUV acquisition images of the 45 galaxies in the CLASSY sample are shown in blue, overlaid on top of optical SDSS *r*-band imaging (unless otherwise noted; red–yellow color bar). The 2.″5 COS aperture used for the UV CLASSY spectra is shown as a blue circle and is very similar to the SDSS 3″ aperture in orange. Galaxies missing SDSS optical spectra do not have a 3″ orange circle. Relative to the HST/COS aperture, most of the NUV light is captured, but a significant fraction of the extended optical light, and subsequently nebular emission from strong emitters (e.g., with EW(Hα $\gtrsim 10^3$ Å), may still be missed. (*Continued on next page*.)

The HST/COS NUV acquisition images are shown in comparison to the optical imaging in Figure 2, demonstrating that the peak of the optical and UV surface-brightness profiles are aligned and that most of the stellar light is captured within the COS 2.″5 aperture. While the optical imaging shown is extended due to the mixture of nebular emission (some with

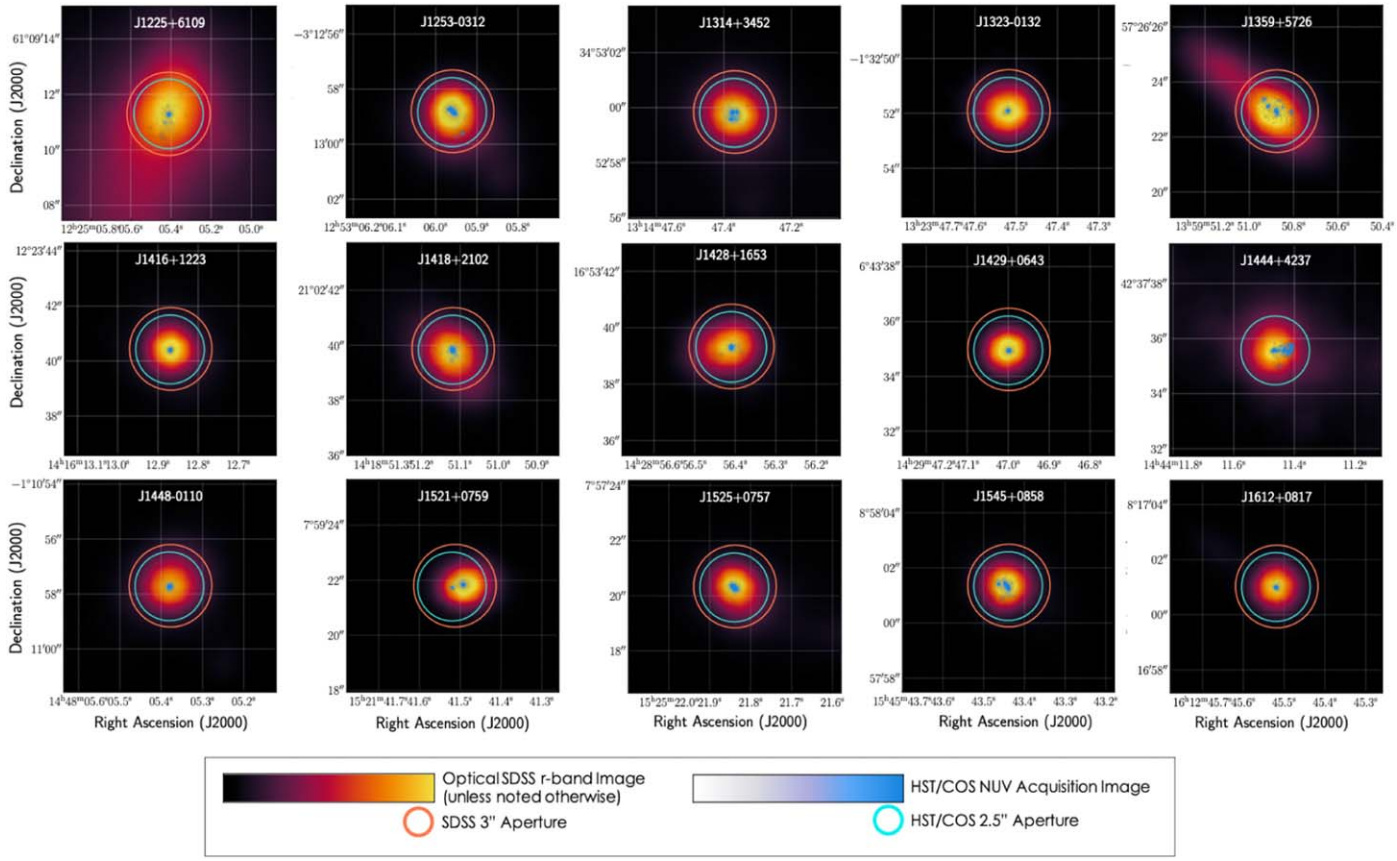

Figure 2. (Continued.)

EW(Hα) $> 10^3$ Å) and light from older (relative to the UV) stellar populations, the similar 2.″5 COS aperture and 3″ SDSS aperture will capture comparable nebular emission in their spectra. This allows the FUV and optical spectra to be used in concordance to characterize the stellar and nebular properties of the CLASSY galaxies. Note, however, that four of the CLASSY galaxies (J0036-3333, J0337-0502, J0405-3648, and J934+5514) have additional knots of star formation clearly outside of the aperture.

Additionally, the CLASSY sample covers a range of galaxy properties, listed in Tables 5 and 6 in Appendix B (see Section 4 for details of property calculations), including stellar masses of $6.22 < \log M_\star(M_\odot) < 10.06$, SFRs of $-2.01 < \log$ SFR ($M_\odot$ yr^{-1}) < 1.60, direct nebular metallicities of $6.98 < 12 + \log(\mathrm{O/H}) < 8.77$, electron densities of $10 < n_e$ (cm^{-3}) < 1120, ionizations, characterized by $\mathrm{O_{32}} = [\mathrm{O\,III}]\,\lambda5007/[\mathrm{O\,II}]\,\lambda3727$, of $0.54 < \mathrm{O_{32}} < 38.0$, and reddening values of $0.001 < E(B-V) < 0.673$. This broad sampling of parameter space allows the CLASSY sample to uniquely serve as templates for interpreting galaxies across all redshifts. However, it is important to note that the CLASSY sample is biased, on average, to more extreme $\mathrm{O_{32}}$ values (25th and 75th percentiles of 7.70 and 8.25), low stellar masses (25th and 75th percentiles of 7.06 and 9.04), higher SFRs (25th and 75th percentiles of -0.78 and 1.03), and compact UV morphologies.

The range of the total stellar masses, SFRs, and oxygen abundances are shown in Figure 1. In comparison to other $z \sim 0$ (e.g., the Low-Mass Local Volume Legacy, hereafter LMLVL; Berg et al. 2012) and $z \sim 2$ (e.g., Whitaker et al. 2014) surveys, the CLASSY sample follows the expected mass–metallicity trend of local galaxies (left panel of Figure 1), but is offset to higher SFRs that are more typical of galaxies at cosmic noon (e.g., Madau & Dickinson 2014, right panel of Figure 1).

2.2. HST/COS FUV Spectroscopy

Archival data. The CLASSY Treasury program was designed to efficiently capitalize on the significant amount of existing FUV COS data in the HSLA. As a result, the CLASSY spectra includes 96 archival data sets[38] compiled from 177 HST orbits. Of these archival data sets, 3 galaxies have full G130M+G160M+G185M coverage (J0337-0502, J0934+5514, and J0942+3547), 17 galaxies have G130M (21 data sets) and G160M (22 data sets) observations, 16 galaxies have G160M (19 data sets) and G185M (16 data sets) observations, and 5 galaxies have G160M (6 data sets) observations. Additionally, six of the CLASSY galaxies have low-resolution G140L spectra (J1016+3754, J1044+0353, J1119+5130, J1323-0132, J1359+5726, and J1418+2102), which were used for checking the relative flux calibration between the medium-resolution gratings and filling in the continuum in the gaps between gratings and grating segments.

New data. In order to complete the FUV spectral coverage of the CLASSY sample, the archival observations were supplemented with 76 new HST/COS spectroscopic data sets of 42 galaxies, compiled over 135 orbits in Cycle 27 as part of PID 15840. These data consist of 27 G130M data sets, 5 G160M

[38] An HST/COS data set refers to a single `x1dsum` fits file, which is the combined 1D extracted spectra for multiple exposures with the same grating, central wavelength, and aperture combining all FP-POS within a given visit.

data sets, 29 G185M data sets, and 8 G225M data sets. Note that the G225M data sets were necessary to ensure coverage of the C III] $\lambda\lambda$1907,1909 emission lines for the 8 galaxies with $z > 0.11$.

Details of all individual data sets are provided in Table 2. For each CLASSY galaxy, the archival and CLASSY observations are denoted by their program ID (PID), followed by their respective acquisition image and FUV spectral observation details.

2.2.1. General Observing Procedure

Target acquisition. The entire CLASSY sample has precise and accurate target coordinates that enabled consistent pointings between archival and new data with a precision of $< 0\farcs1$. For the 37 targets with previous HST/COS observations, the archival data coordinates were used to acquire new data. For the five CLASSY galaxies selected to target high [S II] electron densities ($n_e > 300$ cm^{-3}), no previous HST/COS observations exist. Instead, coordinates from the SDSS were used for four of these high-density galaxies (J0944+3442, J1200+1343, J1253-0312, J1323-0132) and coordinates for J0127-0619 were adopted from the HST/FOS observations of Thuan et al. (1996). The overall excellent positional alignment of the SDSS and COS apertures is shown in Figure 2.

Target acquisitions were performed using the `ACQ/IMAGE` mode with the `PSA` aperture and `MIRRORA` when possible (87 data sets) for the COS/NUV configuration. The resulting NUV images are useful for understanding the spatial structure of light entering COS aperture. However, `MIRRORB` was employed out of caution for five galaxies (J1016+3754, J1105+4444, J1150+1501, J1157+3220, J1359+5726) that are especially bright in the UV. While the use of `MIRRORB` serves to protect the detector, it has the drawback of producing a double-peaked image that impedes our interpretation of the spatial distribution of light.[39] The CLASSY NUV acquisition images are shown in Figure 2, where targets observed with `MIRRORB` are easily recognizable by their more pixelated distribution of blue NUV light and their additional "ghost" peak along the spectral axis (e.g., J1016+3754; see, also, Table 2 and Paper II). Considering the sample as a whole, the peaks of the UV light distributions of the CLASSY galaxies are clearly well aligned with the positioning of the COS $2\farcs5$ aperture (blue circle). As a result, the COS aperture captures the majority of the UV emission of the CLASSY galaxies. In comparison to the GALEX fluxes of the CLASSY sample, we estimate that on average more than 60% of the total UV flux is captured by the COS aperture.

Spectral observations. The HST/COS FUV observations used in the CLASSY survey were all taken in the `TIME-TAG` mode using the $2\farcs5$ `PSA` aperture. Note that no restrictions were placed on the position angle of the new CLASSY data sets; the implications of this decision will be discussed in Paper II. The `FP-POS` = ALL setting was used for most of the data sets to take four spectral images offset from one another in the dispersion direction, increasing the cumulative S/N and mitigating the effects of fixed pattern noise. `TIME-TAG` mode was employed, allowing abnormal detection events to be filtered out, eliminating cosmic rays in the process. For the G130M grating with the `CENWAVE` set to 1291, only `FP-POS` = 3 and 4 were available for the new observations (see the COS2025 guidelines[40] for further information). Each target was observed for the time predicted to reach a S/N $\gtrsim$ 5 per resolution element in the continuum for the G130M and G160M gratings. The input continuum flux was measured at 1500 Å from, in priority order, existing COS spectra, GALEX fluxes, or an extrapolated model fit to existing optical data. For the G185M and G225M gratings, the observation times were determined to detect the C III] $\lambda\lambda$1907,1909 emission lines with a strength of S/N $\gtrsim$ 3, based on observed C/O values for a given metallicity (see, e.g., Berg et al. 2019a), the observed [O III] λ5007 flux, and the theoretical emissivities. All raw data for the new and archival observations were retrieved from the HST archive and were reduced with the CalCOS pipeline (v3.3.10) using the standard `twozone` extraction technique. In Paper II, we provide a detailed discussion on the optimized extraction techniques employed for the extended sources within the CLASSY sample.

2.2.2. Coaddition Process

Overview. Below we describe the main steps in the coaddition process; however, the discussion of the other intermediate analyses and their impact on the reduced spectra are discussed in Paper II.

The primary HLSPs of the CLASSY treasury survey are high S/N multigrating coadded spectra. However, each HST/COS grating has a different spectral resolution that must be accounted for when combining the data from multiple gratings. Additionally, while the CLASSY galaxies have relatively compact stellar clusters, their nebular emission generally fills the COS aperture (at minimum, with diffuse light; see Figure 2), and consequently, experiences varying degrees of vignetting and degradation in spectral resolution depending on the shape of their overall UV light profile entering the COS aperture.

To address the challenges associated with coadding multiple data sets that consist of different grating configurations, exposure times, and resolutions, we developed a custom `python` reduction code (available as a `jupyter notebook` on the CLASSY HLSP website). The main steps followed in the code are depicted in Figure 3 and include the following: (1) joining the segments/stripes of individual grating data sets, (2) coadding any multiples of individual grating data sets, including all cenwave configurations, (3) coadding data sets across gratings, (4) binning the spectra, and (5) correcting for Galactic contamination. Below we describe each step in more detail.

1. Joining grating segments and stripes. The HST/COS CLASSY spectra were acquired across multiple FUV detector segments and NUV detector stripes, so the first step of the coaddition process unifies these components for each data set. For the G130M, G160M, and G140L gratings, the COS FUV detector has two segments (`FUVA`, `FUVB`),[41] while the NUV detector used for the G185M and G225M gratings has three stripes (`FUVA`, `FUVB`, `FUVC`). For each data set, we extracted the `WAVELENGTH`, `FLUX`, `ERROR`, and `DQ_WGT` (or data quality flag weights) columns for each segment or stripe from the `x1dsum` files produced by the CalCOS pipeline and

[39] https://hst-docs.stsci.edu/cosihb/chapter-8-target-acquisitions/8-4-acq-image-acquisition-mode

[40] https://www.stsci.edu/hst/instrumentation/cos/proposing/cos2025-policies

[41] Note, however, that the G140L grating with the 1105 cenwave configuration only utilizes the `FUVA` segment.

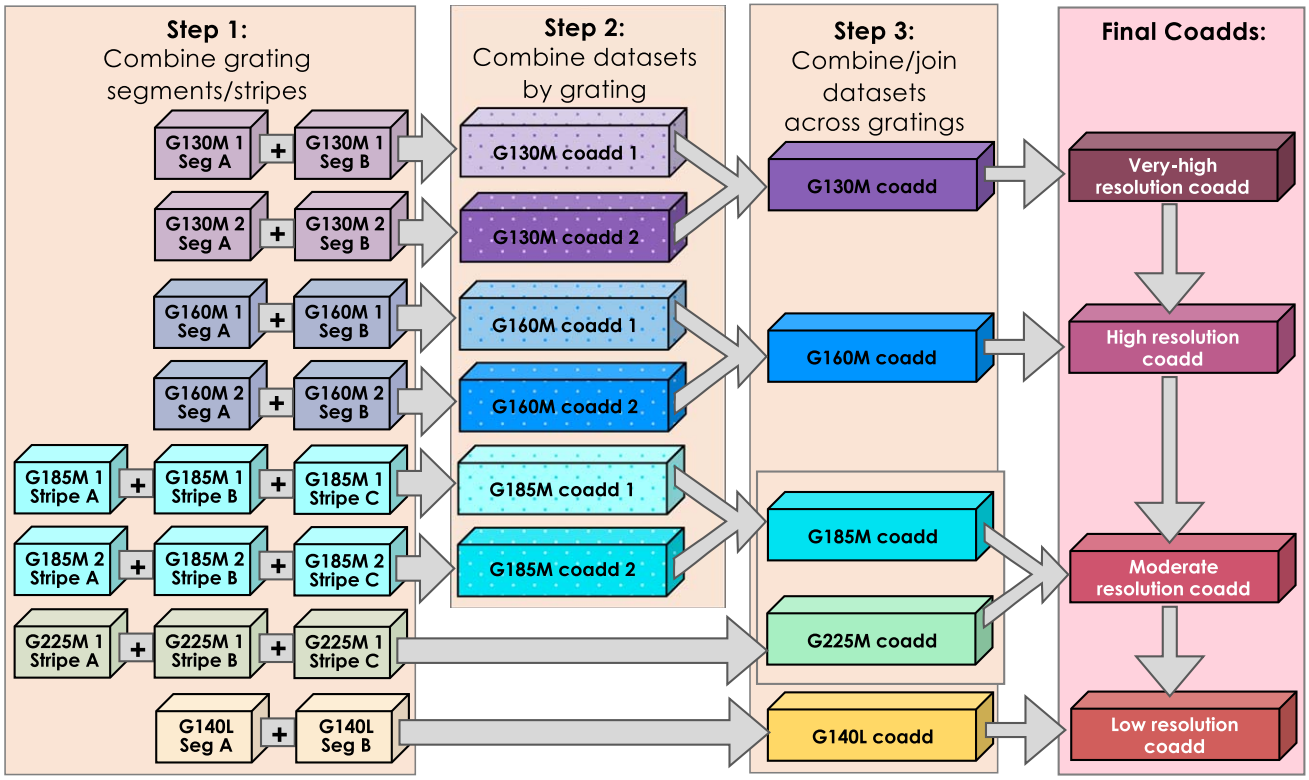

Figure 3. The main steps in the CLASSY coaddition process. The CLASSY spectra are coadded from a combination of G130M, G160M, and one or more of the G185M, G225M, and G140L HST/COS gratings. The first step highlights how the segments of the FUV data sets and the stripes of the NUV data sets are resampled to a common wavelength grid. Then, in step two, any sets of multiple grating data sets for a given galaxy are coadded using the weighting method described in Section 2.3. Finally, to provide the optimal combination of wavelength coverage and spectral resolution for different science cases, the gratings for a given galaxy are coadded into four spectra with different resolutions.

appended them. Because the dispersion varies with wavelength, we then used the `pysynphot` package in `python` (STScI Development Team et al. 2013) to define a source spectrum and interpolate onto a new wavelength grid defined by the largest step in the original wavelength array. Note that there are wavelength gaps between each set of segments/stripes, as well as gainsag holes resulting from detector damage due to extensive airglow emission exposure, so the full spectrum produced for each galaxy is contiguous rather than continuous.

2. Coadding single-grating data sets. If multiple data sets of a given grating exist for an individual target, such as observations acquired over multiple visits or targets observed at multiple central wavelength configurations (`CENWAVE`s), they must be combined in step two of Figure 3 before proceeding. Such collections of grating data sets exist for the G130M observations of one galaxy (J0934+5514/I Zw 18), the G160M observations of five galaxies, and the G185M observations of eight galaxies, or ten CLASSY galaxies in total. These grating data sets were then coadded using a combined, normalized data quality weight (using the `DQ_WGT` array; to filter out or deweight photons correlated with anomalies/bad data) and exposure-time-weighted calibration curve (to preserve the Poisson count statistics). This weighting method was used for all instances where coadding was performed.

3. Coadding multiple grating data sets. Accounting for the change in spectral dispersion between individual gratings, and data sets, is a particularly difficult task. Not only does dispersion change as a function of wavelength across the detector, it also changes as a function of lifetime position on the COS FUV detector (the CLASSY data span all four lifetime positions thus far), and is degraded by extended CLASSY sources depending on their specific UV light profiles and aperture position angles. To take this into account, at each stage of the coadding process, we performed a common resampling of the wavelengths to the highest dispersion of a given combination of gratings. The different spectral dispersion of the coadds allow CLASSY to be used for many scientific studies that require a range of spectral resolutions. Specifically, we produce four spectral coadds for each galaxy with different resolutions:

1. *The very-high-resolution (VHR) coadds.* Consisting of only G130M spectra, which have a nominal point-source resolution of 9.97 mÅ pixel^{-1} or 0.060 Å resel^{-1}; this is the highest spectral resolution of the CLASSY gratings.
2. *The high-resolution (HR) coadds.* Consisting of the CLASSY medium-resolution FUV gratings, or G130M +G160M spectra, with a nominal point-source resolution of 12.23 mÅ pixel^{-1} or 0.073 Å resel^{-1}.
3. *The moderate-resolution (MR) coadds.* Consisting of the CLASSY FUV+NUV medium-resolution gratings, or G130M+G160M+G185M+G225M spectra, with a nominal point-source resolution of 33 mÅ pixel^{-1} or 0.200 Å resel^{-1}.
4. *The low-resolution (LR) coadds.* Consisting of the CLASSY medium- and low-resolution gratings, the possible grating combinations include G130M+G160M+G140L and G130M+G160M+G185M+G225M+G140L, with a nominal point-source resolution of 80.3 mÅ pixel^{-1} or 0.498 Å resel^{-1}.

Note that the flux calibration was performed for each data set during the initial reduction by CalCOS; however, the relative fluxing between gratings was also carefully considered during the coadding process. In short, the G160M spectrum was treated as the flux anchor of each spectrum, and the continuum of all other data sets were fit and scaled to G160M prior to coadding. See Paper II for a detailed discussion of the flux calibration and its effects on the final coadded CLASSY spectra.

4. Binning the spectra. In order to gain S/N, the coadded spectra were also binned in the dispersion direction. The COS medium-resolution gratings have a resolving power of $R \sim 15{,}000$ for a perfect point source, which corresponds to six FUV detector pixels in the dispersion direction. All coadds were binned by a factor of six to reflect this using the `SpectRes` (Carnall 2017) `python` function, which efficiently resamples the spectra and their associated uncertainties onto an arbitrary wavelength grid while preserving flux.

5. Correcting for Galactic contamination. Finally, proper interpretation of UV spectral properties requires the removal of potential contamination from geocoronal emission and Milky Way interstellar absorption. It is important to note that this contamination affects the absorption spectra of the entire CLASSY sample, whether directly by deforming intrinsic features or indirectly by degrading adjacent regions of good continuum. However, the high-ionization Milky Way absorption features (i.e., Si IV and C IV) are typically weak (Savage et al. 2000) relative to the intrinsic profiles, and so they can often be ignored. To correct the CLASSY spectral templates, we create mask arrays assuming central velocities of $v_{\rm cen} = 0$ km s^{-1} and conservative widths of $\Delta v = 500$ km s^{-1} for the very-high-, high-, and moderate-resolution coadds and $\Delta v = 1000$ km s^{-1} for the low-resolution coadds.

The final high-quality CLASSY coadded spectra are shown in Appendix E in Figure 12. These coadds provide both high-resolution spectra over the ∼1200–1700 Å range of each object that is important to studies of stellar and ISM absorption features and contiguous FUV ∼1200–2000 Å wavelength coverage at the low resolution that is necessary to simultaneously interpret the stars and gas. However, due to the varying extended nature of the CLASSY sample, the observed spectral resolutions differ considerably among the four coadditions for different galaxies. Specifically, the extended source distribution causes the nominal point-source line-spread function to broaden in complex, unpredictable ways (see Paper II for further discussion). Therefore, to estimate the observed spectral resolution of each galaxy, we measure the Gaussian FWHM of the best (i.e., cleanest and highest S/N) Milky Way ISM absorption feature present. Note that this measurement assumes unsaturated, unresolved lines. Table 3 lists the nominal and measured spectral resolutions of the CLASSY coadded spectra; 41 galaxies had Milky Way ISM features that were well fit by a Gaussian, while the remaining 4 lacked good Milky Way features to fit. While the choice of coadd data set/spectral resolution is left to the user, Table 3 suggests that the moderate-resolution coadds are the most appropriate spectra for most of the CLASSY sample.

2.3. Optical Spectroscopy

High-quality optical spectra have been compiled for the entire CLASSY sample to ensure uniform determinations of galaxy properties. Initially, much of the sample was selected from the SDSS, and so archival SDSS spectra[42] exist for 38 of the CLASSY galaxies. The exceptions are J0036-3333, J0127-0619, J0144+0453, J0337-0502, J0405-3648, J0934+5514, and J1444+4237. Instead, we use VLT/VIMOS integral field unit (IFU) from James et al. (2009) for J0127-0619, MMT Blue Channel Spectrograph spectra from Senchyna et al. (2019) for J0144+0453 and J1444+4237, Keck/KCWI IFU spectra from Rickards Vaught et al. (2021) for J0337-0502, and VLT/MUSE IFU spectra for the remaining four galaxies.

To ensure robust direct T_e measurements for J0808+3948, J0944+3442, and J1545+0858, very high-S/N optical spectral were obtained using the Multi-Object Double Spectrographs (MODS; Pogge et al. 2010) on the Large Binocular Telescope (LBT; Hill et al. 2010). Simultaneous blue and red MODS spectra were obtained using the G400L (400 lines mm^{-1}, $R \approx 1850$) and G670L (250 lines mm^{-1}, $R \approx 2300$) gratings, respectively. Observations used the $1'' \times 60''$ long slit for 3×900s exposures, or 45 min of total exposure per object. The slits were centered on the same coordinates as the COS apertures. Spectra were reduced, extracted, and analyzed using the beta version of the MODS reduction pipeline[43] that runs within the XIDL[44] reduction package. 1D spectra were corrected for atmospheric extinction and flux-calibrated based on observations of flux standard stars from Oke (1990). Further details of the MODS reduction pipeline can be found in Berg et al. (2015).

We gathered additional optical spectra from archival VLT/MUSE IFU spectra and Keck/ESI spectra from R. L. Sanders et al. (2022), in preparation, and spectra that were prioritized over the SDSS spectra due to their superior S/N and spectral resolution. For galaxies with IFU spectra, we extract a spectrum using a $2\farcs5$ aperture to better match the COS aperture. The details of the ancillary optical spectra adopted for the CLASSY sample are listed in Table 4.

3. Coadded Spectra Data Release

Overview. The result of the coaddition process described in Section 2.3 is the first CLASSY HLSP: a set of high-quality, moderately high-resolution, uniformly calibrated spectral templates with contiguous FUV coverage. The CLASSY atlas spectra are stored as multiextension fits (MEF) files containing up to 20 total extensions of spectra, with four possible spectral resolutions and five extensions per resolution set corresponding to combinations of Galactic reddening and redshift corrections. Any use of the CLASSY spectral atlas should cite this work (Paper I) and Paper II. Below we further describe the coadded spectra HLSPs and how to access them.

3.1. Coadded Spectra File Format

The CLASSY coadded spectra HLSP consists of 45 MEF files, or one for each CLASSY galaxy. For a given galaxy, its MEF file can have up to 21 extensions (0–20), where the first extension (0) is the primary header containing general details relevant to the spectrum, and the remaining 20 extensions contain spectral data tables. Information important to the spectra of a given galaxy are stored in the primary fits header

[42] Note that all CLASSY galaxies have $3\farcs0$ aperture SDSS spectra; none were obtained with the $2\farcs0$ BOSS spectrograph.
[43] http://www.astronomy.ohio-state.edu/MODS/Software/modsIDL/
[44] http://www.ucolick.org/xavier/IDL/

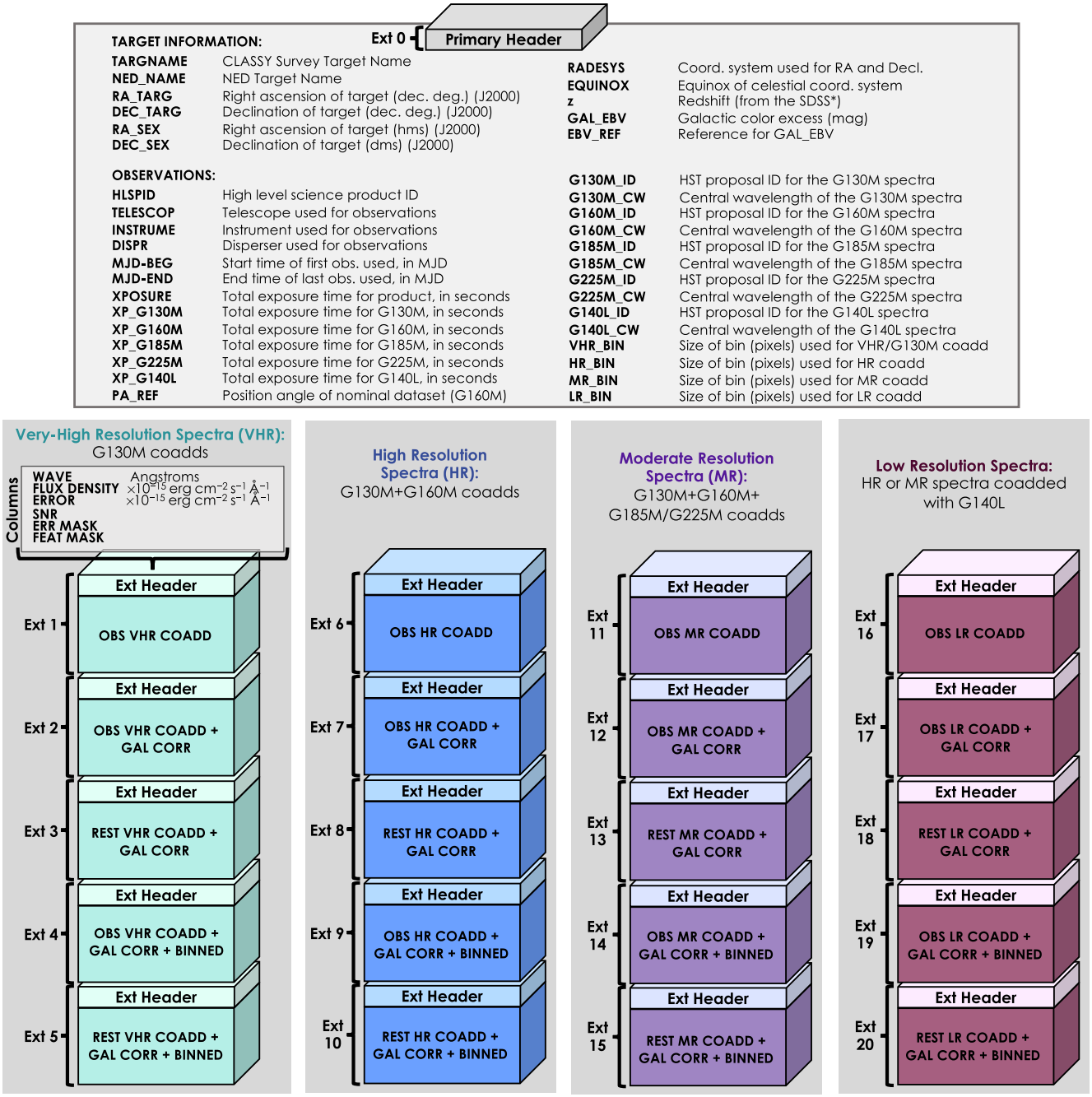

Figure 4. Example multiextension fits (MEFs) file structure for the CLASSY coadd HLSPs. The top shows the informative keywords included in the primary header (extension 0), while the bottom shows the five extensions of spectra formats for each of the four resolution coadds. The extensions can be accessed by extension number or name, as given in each block. Following the HLSP file naming convention, the CLASSY coadded spectra naming template is `hlsp_classy_hst_cos_<target>_scaled_multi_v1_coadded.fits`.

keywords. As shown in Figure 4, there are two groups of keywords that describe either the target or the observations used to produce the coadded spectra.

The CLASSY coadded spectra are stored in many different forms to maximize the convenience for the user depending on their scientific needs. Specifically, for each of the four potential coadd resolutions of a given galaxy, there are a set of five extensions corresponding to the following:

1. *Ext. 1*. The observed-frame coadded spectrum.
2. *Ext. 2*. Ext. 1 + $E(B-V)_{\rm gal}$ corrected: observed-frame coadd, corrected for foreground Galactic extinction.
3. *Ext. 3*. Ext. 2 + z corrected: rest-frame coadd, corrected for foreground Galactic extinction.
4. *Ext. 4*. Ext. 2 + binned: observed-frame coadd, corrected for foreground Galactic extinction, and binned by 6 native COS pixels.
5. *Ext. 5*. Ext. 3 + binned: rest-frame coadd, corrected for foreground Galactic extinction, and binned by 6 native COS pixels.

Extensions 2 and 5 are corrected to the observed frame using the redshifts reported in Table 2, which were adopted from the SDSS, when available. For the galaxies not observed by the

SDSS, redshifts were sourced from another optical spectrum (see adopted references in Table 4). Extensions 4 and 5 contain coadded and binned coadded spectra that were corrected for foreground Galactic extinction. We used the `Python dustmaps` (Green 2018) interface to query the Bayestar 3D dust maps of Green et al. (2015) to determine the total foreground Galactic reddening along the line of sight of the coordinates of each CLASSY galaxy. We note that the Green et al. (2015) map was adopted over more recent versions due to its more optimal coverage of the CLASSY sample. Specifically, the Green et al. (2015) map provides $E(B-V)$ values for all but two galaxies (J0405-3648 and J0036-3333) in the CLASSY sample, whereas the most recent Green et al. (2019) map only covers 16 of the 45 galaxies. Fortunately, for these 16 galaxies covered by both maps, the average difference in $E(B-V)$ is only 0.030 magnitudes, with 25th and 75th percentiles of 0.012 and 0.040 magnitudes, respectively. The foreground Galactic extinction correction was then applied using the Cardelli et al. (1989) reddening law.

As shown in Figure 4, these five extensions form a set of coadded spectra that are repeated for each resolution that exists for a given galaxy. All 45 CLASSY galaxies have VHR and HR coadds, while 42 have MR coadds. One of the three galaxies missing an MR coadd, J1112+5503, is missing G185M observations owing to an observational failure that was not made up as it was the final CLASSY observation. The other two galaxies missing MR coadds, J1044+0353 and J1418+2102, already had significant C III] $\lambda\lambda$1907,1909 detections in their archival G140L spectra that deemed follow-up G185M spectra unnecessary. Including these three galaxies, six of the CLASSY galaxies have G140L spectra and subsequent LR coadds. In summary, four CLASSY galaxies have 20 spectral extensions (VHR, HR, MR, and LR coadds), and the remaining 41 have 15 extensions (VHR, HR, and MR coadds).

Each extension in the CLASSY coadded spectra HLSPs is a simple data table with six columns. The columns correspond to wavelength (Å), flux density, error, S/N ratio, an error mask, and a contamination mask, where the fluxes and errors are given in units of 10^{-15} erg s^{-1} cm^{-2} Å^{-1}. The error mask in the fifth column of each extension denotes the wavelengths of low photon counts (<20) in which the symmetric error propagation used may be inappropriate (for further discussion, see Paper II). Here the default `0` indicates good count levels, while `1` indicates low counts in at least one input data set, and `2` warns of low counts in the coadded data set. Finally, the spectral mask in the sixth column of each extension can be used to remove the regions contaminated by geocoronal emission from Lyα and O I $\lambda\lambda$1301,1305,1306 and Milky Way interstellar absorption features. For most of the CLASSY sample, the redshift is large enough to cleanly separate the geocoronal and Milky Way features from extragalactic features of interest. However, for galaxies with $z \lesssim 0.003$, and depending on the extent of the stellar wind and outflow features in a given galaxy, users should examine features for contamination. Finally, each fits file has a table detailing the individual observations used in the coadds as the last extension. A detailed demonstration of the final CLASSY atlas spectra is shown for an absorption-line galaxy, J0036-3333, and an extreme emission-line galaxy, J1323-0132, in Figures 5 and 6, respectively. These moderate-resolution coadded spectra highlight the diversity of spectral features observed in the CLASSY sample.

3.2. HLSP Digital Access

All CLASSY Treasury HLSPs will be released to the astronomical community in digital form as they are completed. The publication of this paper marks the release of the first HLSP, the CLASSY FUV spectral atlas of star-forming galaxies, on two main platforms.

First, all CLASSY HLSPs will be available via the CLASSY HLSP home page,[45] which also serves as the main website for the CLASSY Treasury and relevant information. Importantly, this website provides simple tarball downloads of individual CLASSY HLSPs, as well as the entire CLASSY HLSP data collection. In addition to full data access, the CLASSY HLSP home page provides machine-readable table downloads for the tables of properties in this paper (Tables 2, 5, and 6), interactive spectra that allow quick-look examination of the coadded spectral features, user-friendly `jupyter` notebook guides to accessing and using the CLASSY HLSPs, and important links such as to the NASA Astrophysics Database System library of CLASSY publications.

The second platform for accessing the CLASSY HLPSs will be the MAST via the CLASSY MAST website.[46] The CLASSY MAST portal will provide a unique search-and-selection method to access the CLASSY HLSPs, where users can select a subsample of the data products based on HLSP type, filename, or target properties such as coordinates or stellar mass. This search tool will continue to be developed based on the specifics of each HLSP release in order to allow more efficient and straightforward access to data products that are of interest to the user. In this manner, appropriate subsets of the CLASSY HLSPs can easily be selected for a given scientific analysis, to match specific survey sample properties, and more.

3.3. Comparison to Previous FUV Spectroscopic Surveys

The CLASSY atlas provides spectral templates with the powerful combination of contiguous 1200–2000 Å FUV wavelength coverage, high resolution ($\lambda/\Delta\lambda = 15{,}000$), and high S/N (average S/N = 6.4 per resolution element). These templates simultaneously probe the interactions between stellar winds, galaxy-scale outflows, and nebular emission and provide a unique data set that probe spatial scales of 0.1–10.7 kpc across the COS aperture at the range of redshifts of the CLASSY sample. As we discussed in Section 1.3, this combination of qualities of the CLASSY survey is unique with respect to previous FUV spectra surveys.

Interestingly, few CLASSY galaxies are in previous FUV spectral atlases, making it difficult to directly compare them. Fortunately, IUE and CLASSY observations both exist for two galaxies: J0337-0502 and J0934+5514. For a visual comparison, the HST and IUE spectra for J0337-0502 are plotted in Figure 7, showing substantial, but expected differences. The smaller aperture of COS relative to the IUE ($10'' \times 20''$ aperture) records lower UV continuum fluxes (however, this would not be expected for most of the NUV-compact CLASSY sample), and some features are present in only the IUE spectrum, which also contains the SE cluster region. For example, there appear to be weak emission features present just blueward of 1400 Å and at 1750 Å, likely N III], that are emitted by the SE region but not the NW region. Perhaps the

[45] https://archive.stsci.edu/hlsp/classy
[46] https://mast.stsci.edu/search/ui/#/classy

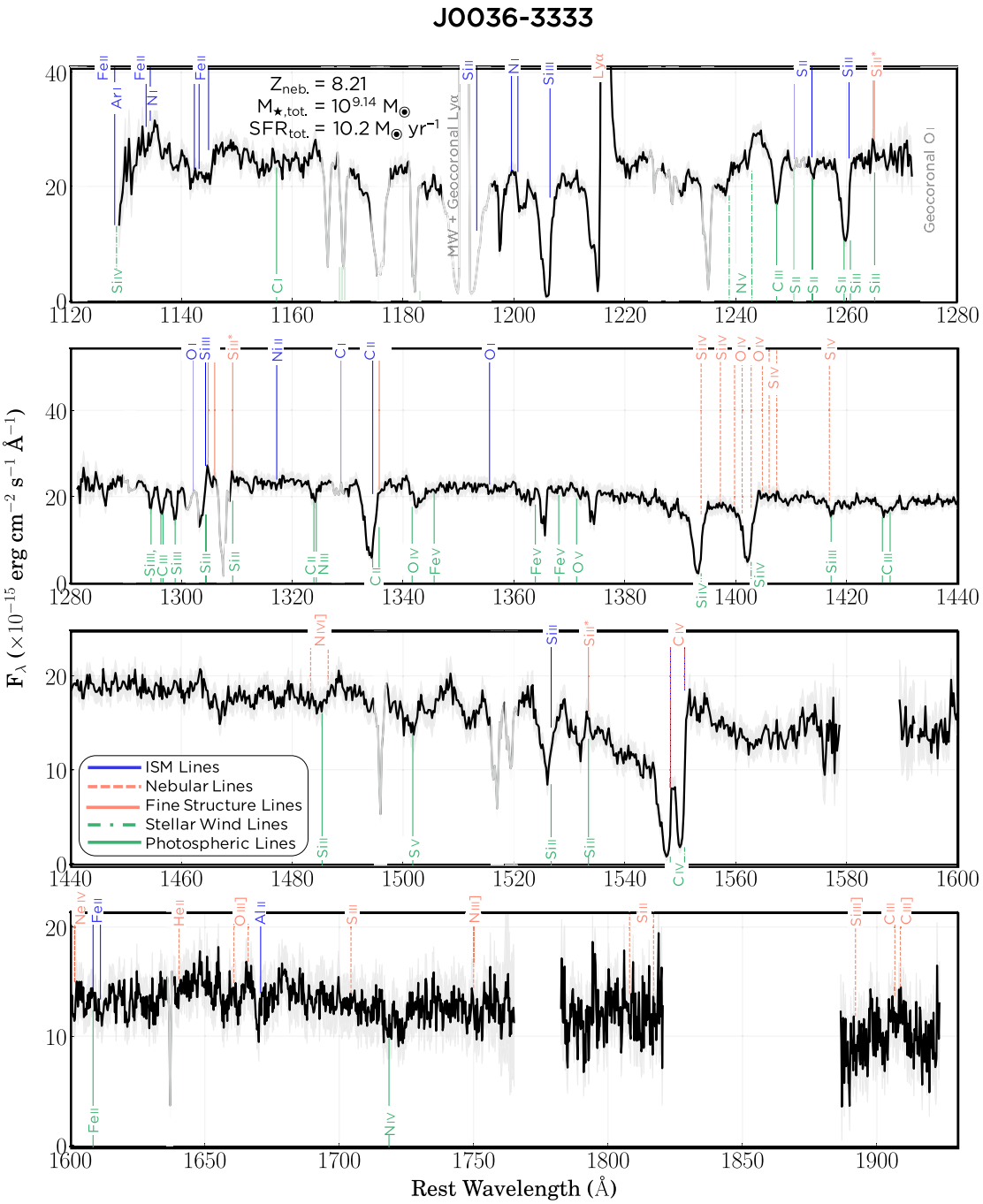

Figure 5. This moderate-resolution coadded CLASSY spectrum for J0036-3333 (black line) is rich with stellar wind features, such as the Si IV and C IV features, and interstellar medium absorption lines, including the strong Si II and C II features. J0036-3333, however, contains no significant UV emission features besides Lyα. Additionally, the flux $\pm$ error spectrum, shown in gray, demonstrates the high S/N of CLASSY and the ability to resolve absorption in J0036-3333 from contamination by geocoronal and Milky Way features (regions where the spectrum/black line is not shown).

most important difference, though, is the significant number of features and details revealed by the higher resolution of the CLASSY spectra ($\sim$0.1 Å resolution compared to the $\sim$6 Å of the IUE spectrum). Specifically, a number of significant ISM absorption lines and nebular emission lines are recovered, such as the O I and Si II lines shown in the left-most inset window of Figure 7 and the C IV, He II, O III], and C III] lines shown in the other three inset windows.

Figure 7 clearly demonstrates that the CLASSY survey provides a dramatic leap forward in FUV spectral atlases and is an invaluable tool for the interpretation and modeling of star-forming galaxies across redshifts.

4. CLASSY Galaxy Properties

Overview. The CLASSY sample of star-forming galaxies was carefully chosen to overcome the common limitations of other surveys introduced by the biases of their samples. Specifically, while CLASSY only targets relatively FUV-bright galaxies (GALEX $m_{\rm FUV} < 20$ and $F_{1500} \gtrsim 1 \times 10^{-15}$ erg s^{-1}

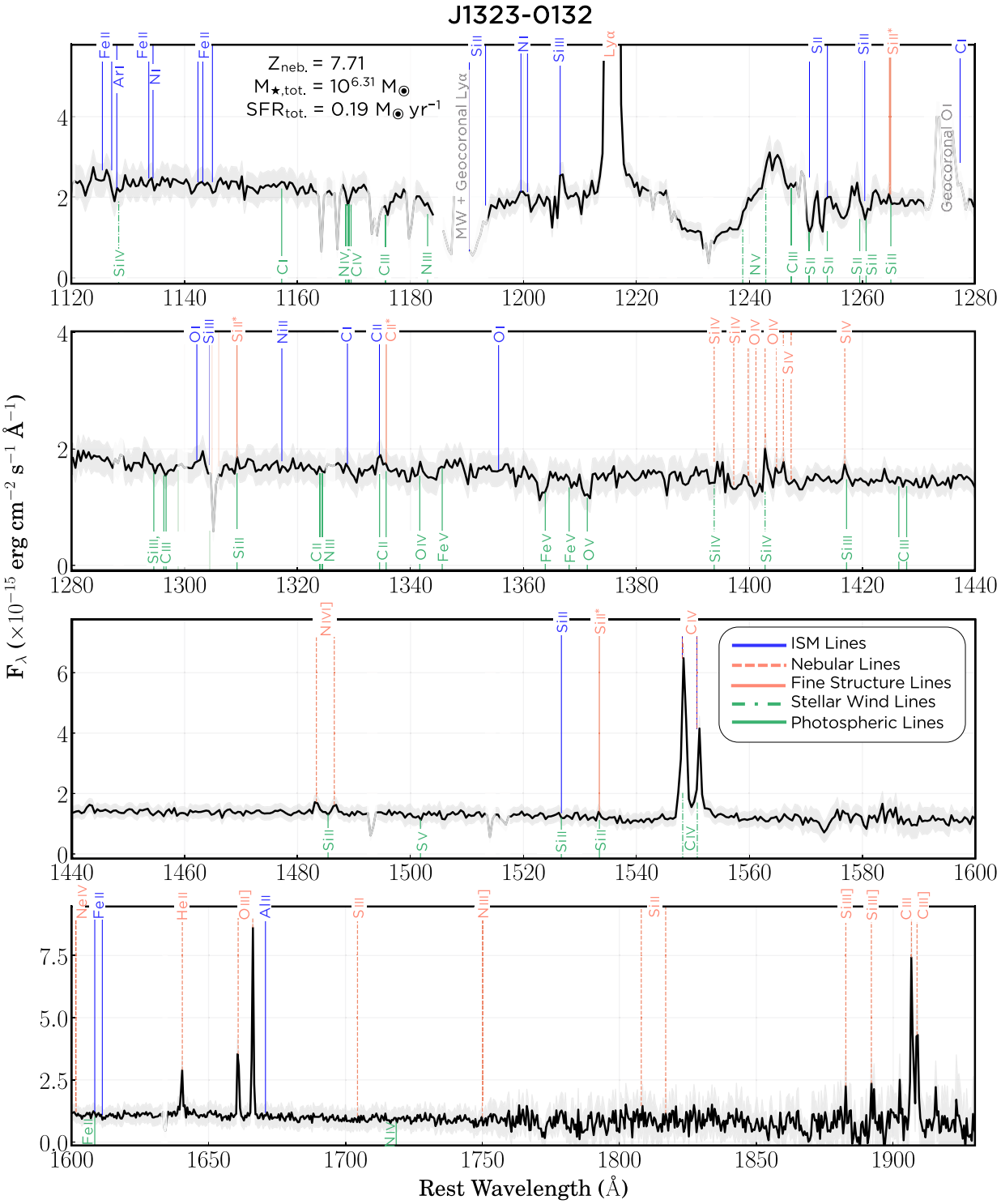

Figure 6. This moderate-resolution coadded CLASSY spectrum for J1323-0132 (black line) is strikingly different than that of J0036-3333 in Figure 5, highlighting some of the emission lines that are observed at varying strengths for a subset of the CLASSY sample. The spectrum has particularly strong emission features from Lyα, C IV, He II, O III], and C III]; additional weak detections from the high-ionization O IV, S IV, and N IV] lines; but minimal absorption features. Note the high S/N of this spectrum is shown by the gray flux $\pm$ error spectrum, while the spectrum/black line is not shown for regions contaminated by geocoronal and Milky Way features.

cm^{-2}), which also ensures the presence of young stellar populations, it probes a broad parameter space in stellar mass, SFR, gas-phase abundance, ionization parameter, and gas-phase electron density in a nearly uniform manner.

Below we describe the measurements of CLASSY nebular quantities and their resulting trends. All physical property calculations used the emission line ratios measured from the optical spectra listed in Table 4 and the PYNEB package in

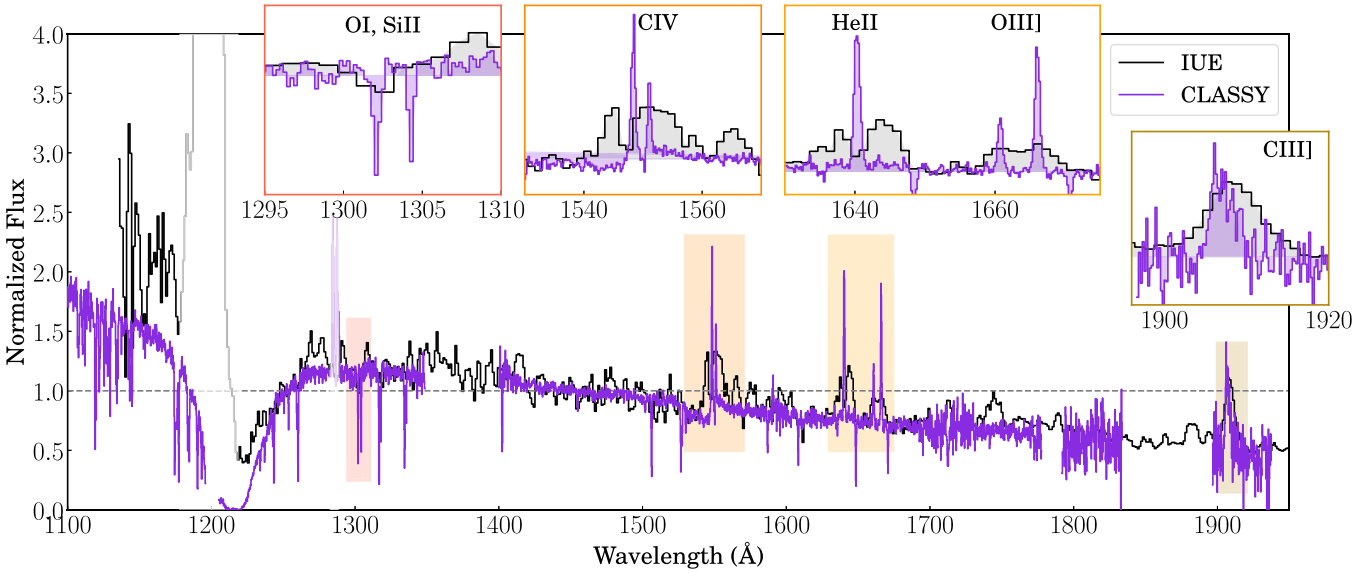

Figure 7. Comparison of rest-frame spectra for J0337-0502 to demonstrate the improvement of CLASSY over previous FUV spectral atlases. The IUE spectrum is relatively low resolution ($\lambda/\Delta\lambda \sim 300$) and consists of the integrated light within its large $10'' \times 20''$ aperture. In contrast, the CLASSY coadded spectral templates are characterized by an unrivaled combination of contiguous 1200–2000 Å FUV wavelength coverage, high spectral resolution ($\lambda/\Delta\lambda = 15,000$), and high S/N (average S/N = 6.4 per resel) for much more compact regions that can be targeted with the $2\farcs5$ COS aperture. Both spectra are normalized at 1450 Å. Note that the breaks in the CLASSY spectrum are due to chip gaps and that the geocoronal Lyα and O I emission have been whited-out. While few features are apparent in the IUE J0337-0502 spectra, the CLASSY spectrum reveals a significant number of absorption and emission features that enable simultaneous studies of the massive stellar population, ISM outflows, and nebular emission.

PYTHON (Luridiana et al. 2012, 2015) with the atomic data adopted in Berg et al. (2019a).

4.1. Contiguous FUV+ Optical Spectra

A benefit of the CLASSY sample is the availability of ample ancillary data, including excellent optical spectra for the entire sample. Optical spectra have long been the gold standard source for calculating important nebular properties, including the oxygen abundance, density, and reddening tabulated in Table 1. As discussed in Section 2.3, the majority of the CLASSY sample was also observed as part of the SDSS, which provides the full optical spectra using a similar aperture ($3''$) to that of the COS UV spectra. Additionally, eight of the CLASSY galaxies have IFU spectroscopy from either VLT/MUSE, VLT/VIMOS, or Keck/KCWI, while nine of the CLASSY galaxies have LBT/MODS or Keck/ESI longslit spectra (see Table 4). We take advantage of these high-S/N spectra in order to calculate direct T_e abundances when the SDSS spectra had insufficient S/N.

There are obvious differences in the aperture sizes between the longslit optical spectra and the circular COS aperture, yet these differences do not result in significant changes in the nebular properties calculated. A full analysis of the aperture effects on the nebular properties of CLASSY galaxies with multiple sources of optical spectra will be discussed in a forthcoming paper by Arellano-Córdova et al. (2022). However, even when the UV and optical spectra have similar apertures, one significant difference is the vignetting of the COS aperture for the UV spectra. Fortunately, for the current purpose of deriving galaxy properties, only the relative flux ratios are needed, and so the absolute flux calibration is irrelevant.

4.2. Emission-line Measurements

Several of the galaxy properties of interest are best measured from the photoionized nebular emission lines present in the adopted optical spectra of CLASSY galaxies. Here in Paper I we focus on measuring the redshift (z), intrinsic dust reddening ($E(B-V)$), nebular electron density (n_e) and temperature (T_e), and gas-phase metallicity (12+log(O/H)) that characterize the CLASSY sample. More detailed discussions of the optical and UV line measurements, their analysis, and their resulting HLSPs (see HLSPs 4, 6, 7, 8, and 9 in Section 5) will be presented in forthcoming papers by Arellano-Córdova et al. (2022) and Mingozzi et al. (2022). Below we briefly describe the CLASSY optical emission line measurements.

For the purposes of calculating the nebular properties of the CLASSY sample, we measured the strength of as many of the optical emission lines necessary to determine the following:

1. $E(B-V)$: Hδ λ4101, Hγ λ4340, Hβ λ4861, Hα λ6563.
2. n_e: [S II] $\lambda\lambda$6717,6731.
3. T_e: [O III] λ4363 + $\lambda\lambda$4959,5007,
   [S III] λ6312 + $\lambda\lambda$9069,9532,
   [N II] λ5755 + $\lambda\lambda$6548,6584, or
   [O II] $\lambda\lambda$3727,3729 + $\lambda\lambda$7320,7330.
4. 12+log(O/H): the required lines are listed above.

For all of the optical spectra, regardless of telescope and instrument used, we first modeled the stellar continuum using the Starlight[47] spectral synthesis code (Fernandes et al. 2005) using the stellar models from Bruzual & Charlot (2003). This step is important for removing any absorption component present in the Balmer emission lines. Emission lines were then fit in the continuum-subtracted spectrum with Gaussian profiles using MPFIT (Markwardt 2009). The fit parameters (i.e., velocity width, line center) of neighboring lines were tied together, allowing weak or blended features to be measured simultaneously. The uncertainty on the flux measurements is assumed to be the uncertainty on the fit returned from the

[47] www.starlight.ufsc.br

Monte Carlo minimization code. The complete database of measured emission line fluxes will be released in a forthcoming HLSP via Arellano-Córdova et al. (2022) and Mingozzi et al. (2022).

We note that the dominant emission component is a narrow, nebular component for the optical emission lines measured for the CLASSY sample. However, broad emission can occur in the presence of stellar winds, outflows, and shocks, and is often clearly visible at the base of the strongest emission features. Because the broad components only contribute a small fraction to the total line flux, we restrict the present analysis to the narrow components only and reserve the analysis of multi-component fits for the forthcoming work of Mingozzi et al. (2022).

4.3. Reddening Corrections

Following the same method discussed in Section 3.1 for the UV spectra, the flux measurements for the optical emission lines were first corrected for Galactic extinction using the Cardelli et al. (1989) reddening law with values queried from the Green et al. (2015) extinction map using the `PYTHON DUSTMAPS` interface (Green 2018). Subsequently, the emission lines were corrected for their corresponding intrinsic galaxy dust reddening. The dust reddening values, $E(B-V)$, were determined using the relative intensities of the strongest Balmer lines available in a given spectrum (i.e., Hα/Hβ, Hγ/Hβ, Hδ/Hβ) with an iterative application of the Cardelli et al. (1989) reddening law, parameterized by an $A_v = 3.1 \times E(B-V)$. Note that Wild et al. (2011) found that the nebular attenuation curve has a slope similar to the Milky Way extinction curve, rather than that of the SMC or the Calzetti et al. (2000) curve, and so the Cardelli et al. (1989) extinction law is appropriate for correcting the CLASSY emission line fluxes. The iterative approach allows for a careful consideration of deviations due to electron temperature and density. The initial reddening seed was determined from the Balmer line ratios using theoretical values from PYNEB, assuming a starting temperature of $T_e = 10^4$ K and $n_e = 10^2$ cm^{-3} for Case B recombination. In turn, this reddening value is then used to determine an initial estimate of the electron density and temperature (using the best-measured auroral line available in a given spectrum). This process is then repeated iteratively to modify the $E(B-V)$, T_e, and n_e values until the electron temperature changes by less than 20 K between iterations. The final reddening estimate is an error-weighted average of the Hα/Hβ, Hγ/Hβ, and Hδ/Hβ reddening values and was used to reddening-correct the optical emission line intensities.

4.4. Electron Densities and Temperatures

Detailed understanding of the nebular properties of star-forming galaxies requires knowledge of the electron temperature, T_e, and density n_e structure in a galaxy compiled from the values in each ionization zone. Such a detailed examination of the physical properties across a nebula and comparison of different T_e and n_e measurements will be the focus of a later work. Here in Paper I, we seek only to measure a characteristic T_e and n_e value for each CLASSY galaxy. To do so, a standard three-zone ionization model is adopted (for a thorough discussion, see Berg et al. 2021), and the high-ionization zone (characterized by O^{++}) is assumed to dominate in the young H II regions of the CLASSY galaxies.

The optical spectra compiled for the CLASSY sample are not uniform — the individual spectra vary significantly in their S/N, resolution, and wavelength coverage. While it is desirable to calculate T_e values in the best and most consistent manner for the entire sample, no single T_e-sensitive auroral line is uniformly detected for the CLASSY sample. As such, direct T_e values were determined using the highest S/N auroral line detection for each galaxy. In general, the [O III] λ4363/λ5007 ratio is prioritized for metal-poor galaxies (12+log(O/H) < 8.0) with blue wavelength coverage, while the [S III] λ6312/$\lambda\lambda$9069,9532 ratio is prioritized in more metal-rich galaxies and/or spectra with red wavelength coverage, and the [N II] λ5755/λ6584 ratio is useful for lower-ionization and more metal-rich galaxies. The [O II] $\lambda\lambda$3727,3729/$\lambda\lambda$7320,7330 ratio was only used if no other T_e measurements were possible, as the red [O II] lines are sensitive to contamination from dielectric recombination at relatively low densities ($n_e > 300$ cm^{-3}). Additionally, the red [S III] lines are susceptible to contamination from atmospheric lines, and so they were visually checked and corrected to the theoretical emissivity ratio when needed.

For simplicity, a single, uniform density is assumed and derived from the n_e-sensitive [S II] λ6717/λ6731 ratio. The [S II] ratios measured for H II regions are typically consistent with the low-density limit ($n_e < 10^2$ cm^{-3}). In this regime, fluctuations on the order of the ratio uncertainty have negligible impact on abundance calculations, and thus support the assumption of a homogeneous density distribution expected to be $n_e \sim 100$ cm^{-3} throughout a nebula.

The uncertainties on the CLASSY T_e and [S II] n_e measurements were determined using a Monte Carlo simulation: An array of temperatures/densities were calculated for a 2D normal distribution of values generated with 500 values in each dimension, with centers and widths corresponding to the values and 1σ uncertainties, respectively, of the measured emission line flux ratio and electron temperature/density. The uncertainty was then taken as the standard deviation of the calculated resulting distribution. The ionic temperatures used and calculated densities are reported in Table 5 in Appendix B.

4.5. Metallicities

Here we determine the total oxygen abundances, 12 + log(O/H), for the purpose of characterizing the gas-phase metal content of the CLASSY galaxies. The determination of a complete database of UV and optical ionic abundances and relative abundances will be reserved for forthcoming papers by Arellano-Córdova et al. (2022) and Mingozzi et al. (2022).

The total oxygen abundance relative to hydrogen is calculated by summing the abundances of the individual ionic species (X^i) together relative to hydrogen as follows:

$$\frac{N(X)}{N(\mathrm{H})} = \sum \frac{N(X^i)}{N(H^+)} = \sum \frac{I_{\lambda(i)}}{I_{\mathrm{H}\beta}} \frac{j_{\mathrm{H}\beta}}{j_{\lambda(i)}}, \quad (1)$$

where the emissivity coefficients, $j_{\lambda(i)}$, are determined assuming the characteristic T_e and n_e of the corresponding ionization zone. To determine the temperature of an ionization zone not directly measured, we adopt the appropriate temperature relationships based on the O_{32} ratio (Yates et al. 2020). For the high-ionization ($O_{32} > 1.25$), high-temperature ($T_e > 2 \times 10^4$ K; low-metallicity) galaxies, we adopt the theoretical $T_e - T_e$ relationships of Garnett (1992), while for the lower-

ionization ($O_{32} < 1.25$), lower-temperature ($T_e < 2 \times 10^4$ K; higher-metallicity) galaxies, we adopt the empirical $T_e - T_e$ relationships of Berg et al. (2020). To be precise, the total oxygen abundances (O/H) should be calculated from the sum of four ionization species that can be present and observed in H II regions:

$$\frac{O}{H} = \frac{O^0}{H^+} + \frac{O^+}{H^+} + \frac{O^{+2}}{H^+} + \frac{O^{+3}}{H^+} \quad (2)$$

However, the ionization energy ranges of O^+ and O^{+2} span the full range of a standard 3-zone ionization model H II region, and the contributions from O^0 and O^{+3} are typically negligible, even in very-high-ionization nebulae (Berg et al. 2021). Therefore, the generalized oxygen abundances for the CLASSY sample calculated here sum only the dominant ionic abundances, O^+/H^+ and O^{+2}/H^+, determined from either the [O II] λ3727 or [O II] $\lambda\lambda$7320,7330 lines and the [O III] $\lambda\lambda$4959,5007 lines.

The resulting oxygen abundances and their uncertainties are tabulated in Table 5 in Appendix B. Note that the uncertainties were simply propagated from the emission line measurements in Section 4.2, accounting for errors in the continuum subtraction, flux calibration, and dereddening. It may be appropriate to consider an additional systemic uncertainty of $+0.1 - 0.2$ dex to account for potential depletion onto dust grains (larger at higher metallicities) and biases due to temperature inhomogeneities (larger at lower metallicities).

4.6. Ionization Parameters

An important parameter for characterizing the physical nature of the ionized gas in a galaxy is the ionization parameter, q, or the flux of ionizing photons (cm^{-2} s^{-1}) per volume density of H, n_H (cm^{-3}). Typically the dimensionless, volume-averaged ionization parameter, log$U$, is used and defined as $U = q/c$. Using the photoionization model prescriptions from Table 3 of Berg et al. (2019b), log$U$ values for the CLASSY sample were inferred from the relationship with the observed light-weighted optical [O III] λ5007/[O II] λ3727 ratio. Typical star-forming regions have been found to have average log$U$ values between -3.5 and -2.9 (e.g., Dopita et al. 2000; Moustakas et al. 2010). In comparison, for the CLASSY sample, we measure ionization parameters of $-3.1 < \log U < -1.6$. The range of CLASSY ionization parameters extend to much high values than typical star-forming regions, likely due to their enhanced SFRs (see Figure 1) and ensuing extreme nebular conditions.

4.7. Stellar Masses and Star Formation Rates

Stellar mass ($M_\star$) and SFRs were determined for the CLASSY sample by constraining the broadband SED fitting via the Bayesian Analysis of Galaxy SEDs (BEAGLE, v0.24.0, Chevallard & Charlot 2016) code with UV+optical photometry. Importantly, BEAGLE models both the stellar populations and the nebular emission. Two sets of stellar mass and SFR parameters were computed assuming a constant star formation history (SFH): (1) an aperture set focused on the star-forming regions within the COS 2.″5 aperture and (2) a galaxy set that characterizes entire host galaxies. Details of the SED fitting process, model assumptions (e.g., a Chabrier (2003) Galactic initial mass function, hereafter IMF, was assumed), and tests are discussed in Appendix C.

The resulting stellar masses and SFRs are reported in Table 6 in Appendix B for both the aperture and total galaxy sets. We also measure the time since the onset of constant SFR, which we refer to here as the galaxy age. For host galaxies, we find the ages of the constant SFH of our sample spanning <5 Myr to 5 Gyr, with a 16%–50%–84% range of $\log \mathrm{Age/yr} = 8.18^{+0.33}_{-0.75}$. According to these results, the youngest galaxy is J1323-0132, (an extreme emission-line galaxy with EW Hβ = 251 Å) with an age of only $3.2^{+19.5}_{-1.7}$ Myr. The other corresponding property ranges for CLASSY are $6.77 < \log M_\star/M_\odot < 9.15$, with a median of $\log M_\star/M_\odot = 8.12$, $-2.01 < \log \mathrm{SFR}/(M_\odot\ \mathrm{yr}^{-1}) < 1.60$, with a median of $\log \mathrm{SFR}/(M_\odot\ \mathrm{yr}^{-1}) = 0.39$, and $-9.49 < \log \mathrm{sSFR/Gyr}^{-1} < -7.03$, with a median of $\log \mathrm{sSFR/Gyr}^{-1} = -8.05$. Typical uncertainties for host galaxy measurements are $\sigma_{\log M_\star/M_\odot} = 0.27^{+0.06}_{-0.04}$ and $\sigma_{\log \mathrm{SFR}/(M_\odot \mathrm{yr}^{-1})} = 0.18^{+0.13}_{-0.05}$.

For aperture measurements, we find $\log \mathrm{age/yr} = 7.84^{+0.55}_{-0.86}$, $4.91 < \log M_\star/M_\odot < 9.74$, with a median of $\log M_\star/M_\odot = 7.39$, $-3.04 < \log \mathrm{SFR}/(M_\odot\ \mathrm{yr}^{-1}) < 1.43$, with a median of $\log \mathrm{SFR}/(M_\odot\ \mathrm{yr}^{-1}) = -0.05$, and $-8.66 < \log \mathrm{sSFR/Gyr}^{-1} < -7.03$, with a median of $\log \mathrm{sSFR/Gyr}^{-1} = -7.78$. The typical uncertainties are $\sigma_{\log M_\star/M_\odot} = 0.29^{+0.05}_{-0.04}$ and $\sigma_{\log \mathrm{SFR}/(M_\odot \mathrm{yr}^{-1})} = 0.17^{+0.08}_{-0.06}$, similar to the values found for the host galaxy measurements. The fact that the aperture measurements lack UV photometry is partly mitigated by the large excesses in broadband flux caused by strong nebular emission from the starburst, and BEAGLES' ability to account for this emission in its models. This excess is most evident in aperture flux, while in measuring the total flux it is degraded by the relatively older stellar population outside of the aperture. Note that we have adopted a simple constant SFH for simplicity and consistent comparison with high-redshift galaxies; however, this method can result in large systematic uncertainties (see, e.g., Lower et al. 2020). We will further assess the SED parameters relative to the optical spectra derived properties, as well as explore the effects of different attenuation models, in a future paper.

5. Global Properties of the CLASSY Galaxies

By design, the CLASSY sample broadly probes many galaxy parameters. Specifically, the CLASSY sample spans approximately four orders of magnitude in both SFR and $M_\star$, roughly two orders of magnitude in both sSFR and gas-phase oxygen abundance, one order of magnitude in the O_{32} ionization ratio, and two orders of magnitude in gas-phase electron density. This broad sampling of parameter space is demonstrated in Figure 8 by plotting the properties calculated from the optical spectra and UV+optical photometry described in Section 4.

5.1. The SFR–M$_\star$ Relationship

The upper row of Figure 8 shows that the SFRs and stellar masses of the CLASSY sample form a tight, increasing trend when both the total galaxy properties (left) and the total galaxy surface density properties (right) are considered. To parameterize the CLASSY stellar mass versus SFR relationship, we used the pythonLINMIX Bayesian linear regression code. LINMIX implements a linear mixture model algorithm (Kelly 2007) to fit data with uncertainties on two

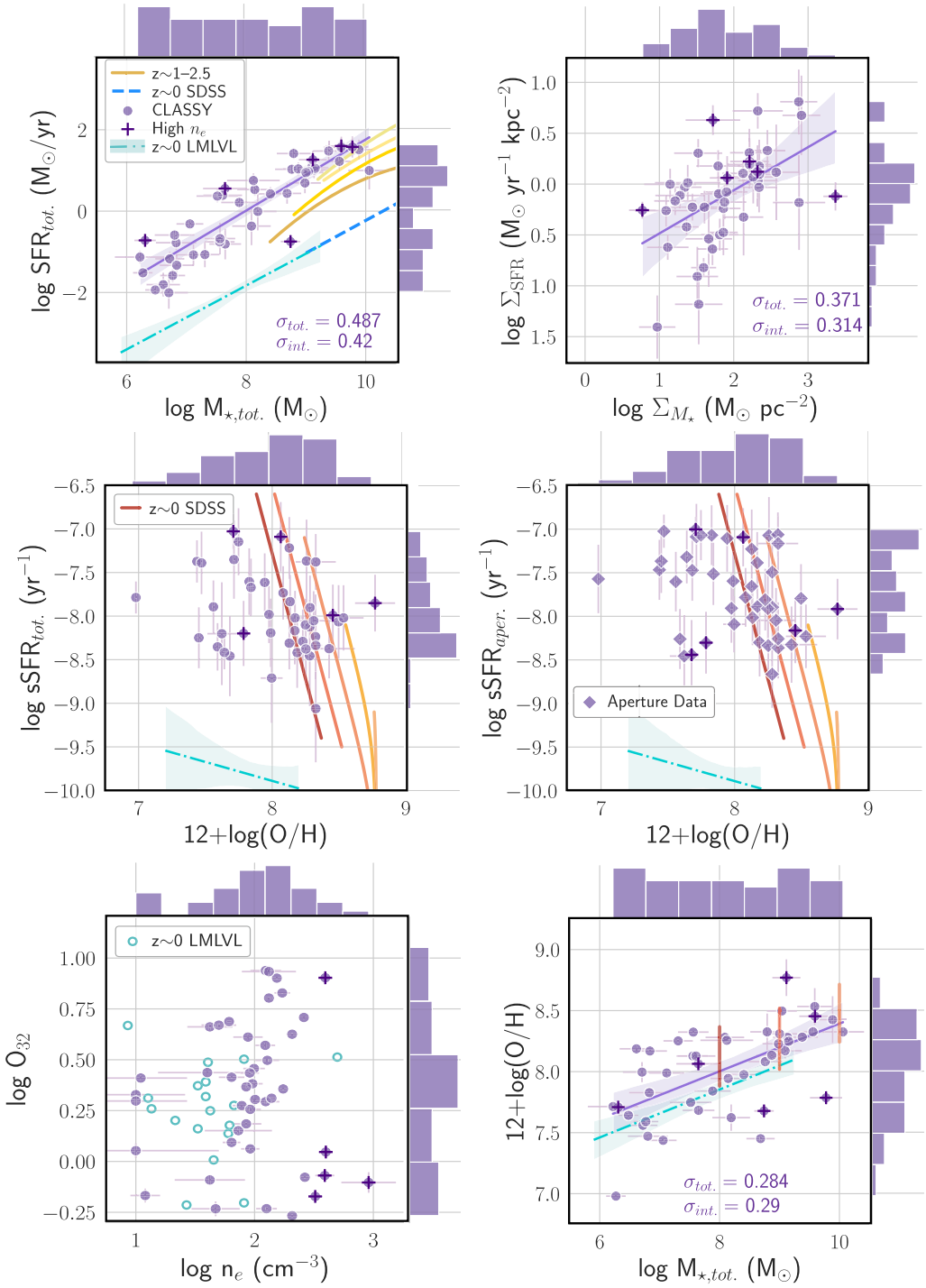

Figure 8. The CLASSY sample properties, as measured from the optical spectra and UV+optical photometry described in Section 4, span a broad range of parameter space. Top row: star formation rate is plotted vs. stellar mass for both the entire galaxy (left) and in terms of surface density (right). The left plot shows a trend that extends to lower masses and star formation rates, but lies above the previous galaxy sample studies at $z \sim 0$ (SDSS; Chang et al. 2015, blue dashed line and LMLVL; Berg et al. 2012 and Lee et al. 2009, cyan dotted–dashed lines) and $z \sim 1$–2.5 (Whitaker et al. 2014, yellow lines). The total and intrinsic scatter of the observed trend are given as $\sigma_{\rm tot.}$ and $\sigma_{\rm int.}$, respectively. Middle row: specific star formation rate is plotted against gas-phase oxygen abundance, using the total stellar mass and SFR on the left and the aperture values on the right. Here, the majority of the CLASSY sample aligns with or extends from the Curti et al. (2020) relationships for $10^8 < M_\star/M_\odot < 10^{11}$ (red to yellow lines, respectively) star-forming SDSS galaxies, but lies well above the dwarf galaxies of the LMLVL (Berg et al. 2012; Lee et al. 2009). Bottom row: oxygen ionization ratio is plotted vs. density in the left-hand plot, showing the wide range in nebular conditions of the CLASSY sample. In the bottom right-hand plot, gas-phase oxygen abundance is plotted relative to total stellar mass, showing the well-known mass–metallicity relationship. The CLASSY sample seems to follow the same trend as other normal star-forming galaxies (e.g., Berg et al. 2012; Curti et al. 2020), but with larger scatter.

variables, and includes an explicit treatment of the intrinsic scatter. Using this analysis, we fit the linear relationship and determined the 1σ dispersion. As a result, we find a relationship for the total galaxy properties of

$$\log \mathrm{SFR_{tot}} = (0.91 \pm 0.07) \times \log M_{\star,\mathrm{tot}} - (7.25 \pm 0.61),$$

with a total scatter of $\sigma_{\rm tot} = 0.49$ dex and an intrinsic scatter of $\sigma_{\rm int} = 0.42 \pm 0.07$. For the surface density properties, we find

$$\log\Sigma_{\rm SFR_{tot}} = (0.44 \pm 0.13) \times \log\Sigma_{M_{\star,\rm tot}} - (0.92 \pm 0.25),$$

with a total scatter of $\sigma_{\rm tot} = 0.37$ dex and an intrinsic scatter of $\sigma_{\rm int} = 0.31 \pm 0.05$. Due to the relatively small errors determined for the stellar mass and SFR measurements, the scatter seems to be largely intrinsic, accounting for roughly 80% of the total scatter. However, these uncertainties do not incorporate the contributions from the uncertainties in the stellar models, IMF, or attenuation curve assumptions, and so they may be misleading.

The small dispersion in the CLASSY SFR–$M_\star$ relationship is unsurprising: star-forming galaxies are known to follow the star-forming main sequence (MS; e.g., Brinchmann et al. 2004; Noeske et al. 2007; Salim et al. 2007). The MS has further been identified as a plane in the fundamental metallicity relationship (Mannucci et al. 2010). The tightness of the MS is thought to result from self-regulation that significantly slows the conversion of gas to stars (e.g., Bouché et al. 2010; Davé et al. 2012). Galaxies with elevated SFRs appear as shifted-up outliers from the star-forming MS. It is, therefore, informative to compare CLASSY to the MS.

To this end, we consider both the nearby and intermediate redshift samples for comparison MSs. At $z \sim 0$, we consider two samples: first, the Chang et al. (2015) sample, which derived stellar masses and SFRs for approximately 10^6 SDSS +WISE galaxies; second, and perhaps the best comparison sample, is the 19-galaxy low-mass subsample of the Local Volume Legacy (LVL; Kennicutt et al. 2008) analyzed to have direct abundances and improved mass measurements by Berg et al. (2012). While most other surveys comprehensively cover massive, high-surface-brightness systems in flux-limited samples, the LVL survey provides a multiwavelength inventory of a statistically robust, approximately volume-limited sample of star-forming galaxies, which provides an essential baseline of "typical" galaxies with a similar stellar mass range as the CLASSY sample. Plotted in the upper left panel of Figure 8, the Chang et al. (2015) SFR–$M_\star$ trend (dashed blue line) aligns well with and extends the LMLVL (dotted–dashed cyan line) trend to higher masses, forming the $z \sim 0$ MS. For the intermediate redshift ($0.5 < z < 2.5$) MS, we use the Whitaker et al. (2014) mass-complete sample of approximately 4×10^4 star-forming galaxies in the CANDELS fields (gold lines).

We note that it is important to compare properties derived using the same methodology. The present work, Chang et al. (2015) sample, and Whitaker et al. (2014) sample all use a Chabrier (2003) IMF and SED fitting to determine masses and SFRs. On the other hand, the low-mass LVL (LMLVL) sample adopted the Salpeter (1955) IMF and used Hα + [N II] fluxes to determine the SFRs (Lee et al. 2009). We, therefore, converted the LMLVL SFRs to a Chabrier (2003) IMF using the scaling from Kennicutt & Evans (2012). Additionally, we also consider the Hα SFRs determined for the CLASSY sample (see Section 4.7) for proper comparison to the LMLVL SFRs. Interestingly, the CLASSY Hα SFRs determined in Appendix C are 0.22 dex larger on average than the aperture SED-derived values, but with a large standard deviation of 1.16 dex, and so they would only serve to slightly increase the average offset of the CLASSY sample from the $z \sim 0$ MS in Figure 8.

The CLASSY SFR–$M_\star$ relationship in the upper left panel of Figure 8 lies above the $z \sim 0$ and $0.5 < z < 2.5$ MSs trends. The CLASSY trend has a similar slope to the $z \sim 0$ MS, but lies roughly 2 dex higher in SFR, while the intermediate-z MS relationships begin to approach the CLASSY relationship with increasing redshift. This shows that CLASSY galaxies, selected to be compact and UV bright, have significantly enhanced sSFRs relative to their star-forming MS counterparts at $z \sim 0$; rather the CLASSY sSFRs are more comparable to a $z \sim 2$ galaxy population.

The middle row of Figure 8 shows the total specific SFRs (left) and the aperture sSFRs (right) versus the direct T_e-method gas-phase oxygen abundances of the CLASSY sample. Here, the majority of the CLASSY sample aligns with or extends from the Curti et al. (2020) relationships for $10^8 < M_\star/M_\odot < 10^{11}$ (red to yellow lines, respectively) star-forming SDSS galaxies, but lies 1–3 dex above the LMLVL trend. Given that both Curti et al. (2020) [48] and Berg et al. (2012) used direct T_e methods for their oxygen abundance determinations, this offset in sSFR is likely due to the boosted SFR of the CLASSY sample (see the SFR–$M_\star$ trend).

5.2. Ionization Parameter and Density Properties

The bottom left-hand panel of Figure 8 shows that the CLASSY galaxies also probe a broad range of ionization parameter, as indicated by the oxygen ionization ratio, $O_{32} = [\text{O III}]\lambda5007/[\text{O II}]\lambda3727$, and gas-phase electron density. Most H II regions have measured densities near the low-density limit ($\sim$100 cm^{-3}); this can be seen by the LMLVL sample (blue circles), where all but one galaxy have $n_e < 100$ cm^{-3}. On the other hand, seven CLASSY galaxies have $n_e > 300$ cm^{-3} (purple plus symbols; the high-density CLASSY sample), where additional effects such as dielectric recombination can become important. Given the evidence that higher nebular densities may be more common at higher redshifts (e.g., Sanders et al. 2016, median $n_e \sim 250$ cm^{-3} at $z \sim 2.3$), this high-density sample was included in CLASSY to investigate the role of density.

5.3. The $M_\star$–Z Relationship

In the bottom right-hand panel of Figure 8, the gas-phase oxygen abundance is plotted relative to the total stellar mass, showing the well-known mass–metallicity relationship (MZR; e.g., Tremonti et al. 2004). Interestingly, the CLASSY sample closely follows the Berg et al. (2012) direct-metallicity MZR measured for the LMLVL, but with larger scatter. To quantify the comparison, we employ the Kelly (2007) LINMIX fitting method and find the CLASSY MZR to be

$$12 + \log(\text{O/H}) = (0.20 \pm 0.04) \times \log M_{\star,\rm tot} + (6.40 \pm 0.35),$$

where $M_\star$ has units of $M_\odot$, and the total scatter is $\sigma_{\rm tot} = 0.28$ dex and consistent intrinsic scatter. This suggests that the CLASSY sample, while biased to target UV-bright galaxies, is consistent with typical star-forming galaxies evolving along the MZR. The trends plotted in Figure 8 demonstrate the expansive galaxy properties and nebular conditions of the CLASSY sample that allow it to uniquely serve as templates for

[48] Curti et al. (2020) employed a T_e-anchored method based on galaxy stacks, but did not measure T_e abundances for each galaxy directly.

interpreting the galaxies with significant star formation episodes across all redshifts.

6. Potential Science with CLASSY

Overview. The main objective of CLASSY is to use FUV spectra to unify stellar and gas-phase physics, allowing a holistic understanding of massive stars as the drivers of the gaseous evolution of star-forming galaxies. Naturally, the pursuit of this goal will produce a number of additional HLSPs, beyond the coadded spectra, that will be useful to the astronomical community. The enduring value and utility of CLASSY will reside in these state-of-the-art HLSPs products. Below we summarize the main HLSPs that the CLASSY team plans to produce and the scientific objectives they will enable studies of.

The summary of planned CLASSY HLSPs is as follows:

1. CLASSY spectral atlas.
2. Compiled ancillary data.
3. CLASSY stellar continuum fits.
4. Database of emission and absorption feature properties.
5. Database of Lyα emission profile fits.

Additionally, user-friendly CLASSY tutorials on interacting with and utilizing the data products will be released in tandem with corresponding HLSPs. These HLSPs will be used to diagnose a vast array of science objectives, including the (1) massive star astrophysics, (2) physical properties of outflows, (3) Lyα physics, (4) chemical evolution of galaxies, and (5) physics of reionization. Below we provide an early glimpse of the individual science cases that CLASSY will explore and motivate some of the upcoming science that can be done with the data.

6.1. Understanding the Massive Star Properties

Massive stars influence all facets of their host star-forming galaxies including the shape of their UV spectra: massive stars produce copious amounts of high-energy photons that are reprocessed in the ISM and power the nebular emission lines that trace the gaseous physical conditions (e.g., Strömgren 1939; Seyfert 1943; Tinsley 1980); massive stars may have been important contributors to the ionizing photon budget that reionized the early universe (e.g., Ouchi et al. 2009; Robertson et al. 2013, 2015; Finkelstein et al. 2019); massive star winds disrupt the gas cycle in galaxies and drive out multiphased material and more. Despite the obvious importance of massive stars in understanding the evolution of galaxies and the early universe, their ionizing spectra are not well understood. Thus, uncertainties in the shape of the ionizing spectrum have a significant effect on the interpretation of UV spectra, including gas properties, stellar feedback, the production of H-ionizing photons, and the effects of dust. While the implementation of new physics in stellar population synthesis (SPS) models (i.e., rotation, binaries) continues to improve the predictions of the extreme UV (EUV) radiation fields (e.g., Levesque et al. 2012; Eldridge et al. 2017; Götberg et al. 2018), the shape of the ionizing spectrum remains poorly constrained for the metal-poor ($Z/Z_{\odot} < 0.2$) stellar populations that come to dominate at high-z. This shortcoming thwarts our understanding of current moderate-redshift ($z \sim 2$–5) studies and future spectra of high-redshift galaxies expected from ELTs and the JWST.

The CLASSY survey provides an important opportunity for progress: with high-resolution, high-S/N spectra covering the entire FUV (although, not the ionizing continuum directly), CLASSY probes a large suite of emission and absorption features shaped by massive stars. These spectra include the N V $\lambda\lambda$1238,1242, Si IV $\lambda\lambda$1393,1402, and C IV $\lambda\lambda$1548,1550 stellar wind features and the weak Si III $\lambda\lambda$1290,1417, C III $\lambda\lambda$1247,1426,1428, and S V λ1502 photospheric features, both of which are distinctly sensitive to either age or metallicity of the stellar population (e.g., de Mello et al. 2000; Vidal-García et al. 2017; Chisholm et al. 2019), but are also broadly distributed in wavelength space (across 12401900 Å).

The power of these lines to characterize massive star populations is demonstrated in the top row of Figure 9 for J0036-3333. The CLASSY spectrum is well fit by a light-weighted combination of Starburst99 (SB99; Leitherer et al. 1999, 2010) SPS models following the method of Chisholm et al. (2019; shown in turquoise). Such stellar fits can determine the light-weighted metallicity, age, and reddening of the the massive star population.

Recent $z \sim 0$–3 studies have presented the first demonstrations that the combination of UV stellar and nebular spectral features can be used to constrain the shape of the otherwise unseen ionizing spectra in the EUV (e.g., Steidel et al. 2016, 2018; Olivier et al. 2021). Building on this powerful tool, the CLASSY sample and its superior spectra will open an unprecedented window on the stellar populations that form in a range of environments, including the low metallicity systems that dominate at high redshift. The CLASSY spectra will enable measurements of the stellar photospheric and wind features that can be used as important direct constraints on the metallicity and age of the massive stars and the EUV radiation field they power. In turn, the CLASSY modeled intrinsic ionizing continua can provide the community with the key to understanding how massive stars influence the feedback, the ionization and enrichment of nebular gas, and the conditions leading to the escape of ionizing radiation.

6.2. The Physical Properties of Outflows

The kinematics of the galaxy-scale outflows of gas driven by the massive stellar populations are encoded into the Lyα profiles and ISM resonant absorption lines observed in the FUV. These features currently provide the majority of the data on outflows at both low and high redshift. The crucial question is how these outflows affect the evolution of galaxies. Answers require the determination of the basic properties of the outflows (velocities, outflow rates, ionization state, etc.) and how these depend on the properties of the starburst and its host galaxy (SFR, stellar mass, size, etc.).

The FUV spectral region covered by CLASSY contains a suite of resonance lines from atoms and ions spanning a large range in ionization potential. While several studies addressing the properties derived from the FUV exist (Heckman et al. 2015; Chisholm et al. 2015, 2017), CLASSY represents the opportunity for a major advance. Because CLASSY spans about four orders of magnitude in both stellar mass and SFR (see Figure 7), it is the benchmark sample for investigations of how outflow and galaxy properties scale together in the low-redshift universe. Very few measurements of outflow velocities and mass outflow rates exist for galaxies with masses below $10^9 M_{\odot}$ (e.g., Martin 1999; Martin et al. 2005; Heckman et al. 2015; Bordoloi et al. 2016; Heckman & Borthakur 2016),

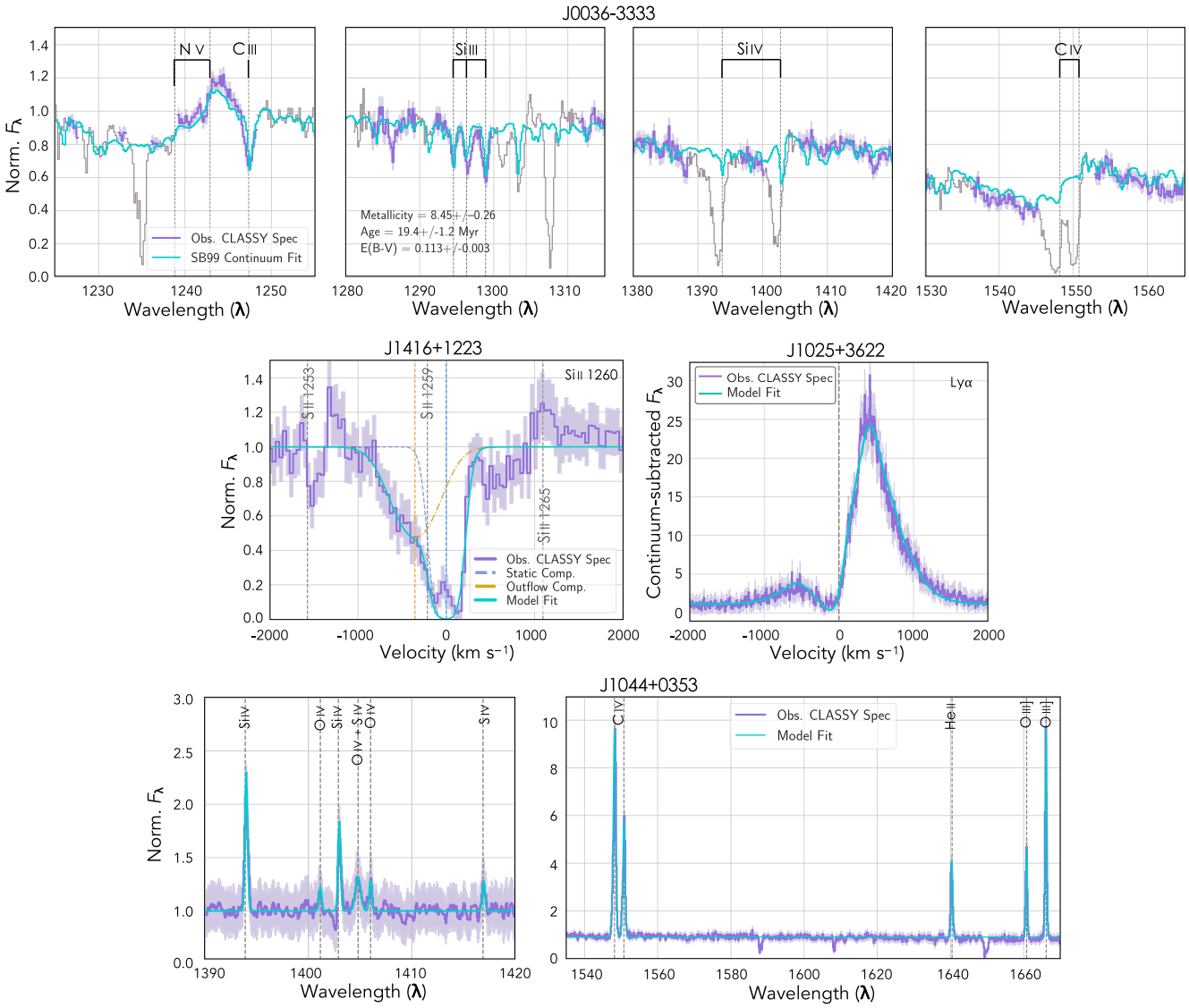

Figure 9. Demonstrations of science that can be derived from model fits to the CLASSY spectra. Top row: the high-resolution coadded spectrum of J0036-3333 is well fit by a light-weighted combination of Starburst99 stellar population synthesis models (turquoise line). The regions of the continuum included in the fit are shown in purple, while masked regions are plotted in gray. The high S/N and spectral resolution of the CLASSY spectra allow both stellar wind (N V $\lambda\lambda$1238,1242, Si IV $\lambda\lambda$1393,1403, C IV $\lambda\lambda$1548,1550) and stellar photospheric (C III λ1247, Si III $\lambda\lambda$1295,1297,1299) features to be fit. Middle left: the Si II λ1260 interstellar absorption feature can be characterized in the high-resolution coadded spectrum of J1416+1223 using a double Gaussian fit. This total fit (solid green line) includes a static component (dashed blue line) that is matched to the line-spread function and an outflowing component (dotted–dashed gold line) that characterizes the kinematics of the low-ionization gas. Middle right: the Lyα profile in the very-high-resolution coadded spectrum of J1025+3622 is well fit by a `tlac` (Gronke & Dijkstra 2014) radiative transfer model. This model can be used to constrain the depth and kinematics of the neutral H gas. Bottom row: the high-resolution spectrum of J1044+0353 contains many high-ionization UV emission lines that are well fit by narrow, nebular Gaussian profiles. These lines, including the Si IV $\lambda\lambda$1393,1403, O IV $\lambda\lambda$1401,1405,1407, S IV $\lambda\lambda$1405,1406,1417, C IV $\lambda\lambda$1548,1550, He II λ1640, and O III] $\lambda\lambda$1661,1666 lines shown, can be used as nebular diagnostics.

where gravitational potential wells are the smallest, and thus the galaxies are most impacted by supernovae feedback (Dekel & Silk 1986).

Some absorption lines also have associated nonresonant fluorescence lines produced by radiative decay into a fine structure level just above the ground state. These lines are seen at both low and high redshifts (e.g., Shapley et al. 2003; Martin et al. 2012; Erb et al. 2012; Jones et al. 2012; Henry et al. 2015; Scarlata & Panagia 2015; Bordoloi et al. 2016; Finley et al. 2017; Wang et al. 2020), where the relative strengths of the fluorescent and absorption lines encode information about the size/structure, geometry, and dust content of the outflow (Prochaska et al. 2011; Scarlata & Panagia 2015; Carr et al. 2018; Wang et al. 2020; Carr et al. 2021). The CLASSY spectra will enable robust measurements of fluorescent emission that can provide a powerful diagnostic of the structure and physical properties of outflows.

The ability to model the complex outflow signatures in the CLASSY galaxies is demonstrated in the middle left panel of Figure 9. The combination of CLASSY's high spectral resolution and S/N enables outflowing gas to be distinguished from static gas in the ISM and absorption profiles to be corrected for the effects of in-filling by resonance scattering (Prochaska et al. 2011; Scarlata & Panagia 2015). For the Si II λ1260.42 absorption feature in J1416+1223, a double Gaussian can be fit to the continuum-normalized spectrum to account for the static ISM component (dashed blue line) and characterize the outflow (dotted–dashed gold line) kinematics

of the low-ionization gas. Absorption-line fits are presented in CLASSY III (Xu et al. 2022). Such detailed absorption-line analysis can then be used to analyze covering fractions, ion column densities, and outflow rates. These measurements will constrain the stellar feedback on a wide-assortment of galaxy types, opening a new window onto the impact of stellar feedback on galaxy evolution with a specific emphasis on very low stellar mass galaxies.

6.3. Lyα Physics

Outflows are predicted to promote the escape of Lyα photons before they are absorbed by interstellar dust. The shapes of the emergent Lyα line profiles therefore contain information about the physical properties of outflows. A comparison of outflow properties measured from Lyα emission lines and resonance absorption lines is a key CLASSY objective.

The CLASSY spectra cover Lyα for all targets, revealing a broad diversity of Lyα profiles. Geocoronal emission from Lyα and O I compromise a few Lyα profiles. Additionally, a significant fraction of the CLASSY spectra show broad Lyα absorption troughs underneath the Lyα emission that make continuum placement challenging, particularly in the lowest redshift targets where it blends with damped H I absorption from the Milky Way. For the majority of the CLASSY sample, however, radiative transfer models can be used to fit their complex Lyα profiles. This technique is demonstrated for J1025+3622 in the middle-right panel of Figure 9, where a Voigt profile was used to remove the underlying absorption, and the Lyα emission was modeled using the "shell-model" (e.g., Verhamme et al. 2006, 2008). Specifically, we employed the fitting pipeline described in Gronke et al. (2015), which builds upon models computed by the Monte-Carlo radiative transfer code `tlac` (Gronke & Dijkstra 2014). The details of such Lyα models offer the opportunity to constrain how the ISM and CGM modify the intrinsic Lyα emission through resonance scattering (Gronke et al. 2015).

Photons emitted by a central source in a simple shell-model are scattered by an expanding shell of neutral hydrogen with variable dust opacity (Gronke et al. 2015). The fitted shell velocity and H I column density have frequently been used to constrain galaxy properties (e.g., Kulas et al. 2012; Martin et al. 2015; Gronke 2017). Yet direct comparisons to outflow properties derived from other spectral diagnostics remain limited to small samples (Orlitová et al. 2018; Carr et al. 2021). The combined Lyα, resonance absorption, and fluorescent emission profiles of the CLASSY sample will therefore allow discrepancies in outflow parameters to be addressed via forward modeling of Lyα profiles with, e.g., the Semi-Analytical Line Transfer code (SALT; Scarlata & Panagia 2015) and the Radiation Scattering in Astrophysical Simulations code (RASCAS; Michel-Dansac et al. 2020).

A key goal of CLASSY is to determine the strongest scaling relations between Lyα emission and galaxy properties. Many CLASSY spectra show double-peaked Lyα emission-line profiles, an indication of low H I column density channels (Verhamme et al. 2017). These profiles can be used to measure peak-to-peak velocity separations and, more generally, Lyα velocity offsets relative to galaxy redshifts. Given that the peak-to-peak separation appears to be a promising indirect indicator of Lyman continuum (LyC) leakage (Verhamme et al. 2015; Izotov et al. 2018; Jaskot et al. 2019), the CLASSY peak separations along with measurements of partial covering (via UV resonance lines), the age and metallicity of the massive star population, and the ionization structure inferred from UV and optical emission lines can be used to investigate this escape fraction indicator. Examining the same galaxies from all these perspectives will provide unique insight into escape fractions, clarifying their relationship to radiative and mechanical feedback. A limitation imposed by the targets' proximity and the solid angle subtended by the COS PSA is that the measured equivalent widths and Lyα escape fractions will be aperture limited.

Looking back to the epoch of reionization (EoR), the increasing fraction of neutral hydrogen blocks Lyα transmission. The declining volume density of Lyα emitters at high-z constrains the reionization history, and a better understanding of Lyα velocity offsets, specifically their dependence on galaxy properties, will reduce the potential systematic errors on the inferred neutral fractions (Mason et al. 2018, 2019; Naidu et al. 2020). The CLASSY sample includes extreme emission-line galaxies, the closest local analogs of EoR galaxies, making them excellent environments to study the star-gas interplay that shaped cosmic reionization.

6.4. UV Diagnostics of Chemical Evolution

The CLASSY spectra contain strong UV emission lines that characterize a plethora of gas properties, including temperature, density, and metal content (both nebular and ISM, e.g., James et al. 2014; Byler et al. 2018, 2020), as well as reflecting the shape and hardness of the ionizing spectrum. The bottom panel of Figure 9 demonstrates Gaussian fits to several high-ionization nebular emission lines in the continuum-subtracted spectrum of J1044+0353. The full suite of emission-line measurements for the CLASSY sample will be released as HLSPs as part of the forthcoming CLASSY papers by Mingozzi et al. (2022) and Arellano-Córdova et al. (2022).

Such detailed emission line analyses can be used to provide diagnostics of the chemical and physical properties of the CLASSY systems. These include several temperature and density-sensitive line ratios. When combined with optical line diagnostics afforded by the ground-based data, the CLASSY spectra will provide guidance on interpreting purely UV-based diagnostics of high-redshift galaxies. For example, the agreement of electron temperatures derived from the UV auroral O III] $\lambda\lambda$1660,1666 emission lines with those derived from [O III] in the optical can be tested.

Recently, significant efforts have been invested into photoionization modeling of nebular UV emission lines to constrain the radiation fields, ionization sources, and metal content within star-forming galaxies (e.g., Byler et al. 2018; Nakajima et al. 2018; Berg et al. 2021; Olivier et al. 2021). The CLASSY UV emission-line ratios can be calibrated against the well-understood diagnostics from the existing optical spectra to provide the first stringent tests of proposed UV diagnostics, over a large range of physical environments (i.e., SFR, stellar mass, metallicity, gas density). The high-S/N detections of important combinations of UV emission lines, such as C IV $\lambda\lambda$1548,1550/He II λ1640 versus O III] $\lambda\lambda$1661,1666/He II λ1640, are shown in Figure 9. With these lines, CLASSY can assess the utility of proposed UV diagnostics such as the UV versions of the canonical "BPT" diagram (e.g., Feltre et al. 2016; Nanayakkara et al. 2019) to distinguish ionizing sources, C III] $\lambda\lambda$1907,1909 equivalent widths to infer stellar age and

nebular metallicity (e.g., Rigby et al. 2015; Jaskot & Ravindranath 2016; Senchyna et al. 2017; Ravindranath et al. 2020), and resonant emission lines, such as Ly$\alpha\lambda$1215 and C IV $\lambda\lambda$1548,1550 as indicators of ionizing photon escape (e.g., Verhamme et al. 2015; Berg et al. 2019a).

Uniquely, the CLASSY sample also includes a subset of high-density galaxies ($n_e > 300$ cm^{-3}), with which a detailed study of the effects of density on FUV properties can be investigated. Altogether, CLASSY seeks to establish the essential UV diagnostic toolset needed to understand fundamental questions concerning the evolution, physical conditions, and ionization structure of star-forming galaxies across cosmic time.

6.5. Reionization Physics

At redshifts between $z = 6$–10, ionizing photons escaped from galaxies to reionize the universe (Fan et al. 2006). Determining the sources of cosmic reionization is one of four key science goals of JWST. However, neither JWST nor ELTs will directly observe the LyC during the EoR owing to the increasing opacity of the intergalactic medium with redshift. The CLASSY survey will provide templates to understand the gaseous conditions in galaxies similar to high-redshift galaxies. The high S/N and spectral resolution CLASSY observations will reveal complex geometric constraints and their relations to observables like the Lyα emission or the metal covering fraction. Further, the stellar continua observations of the massive star populations can be combined with SPS models (highlighted in Figure 9 to predict the intrinsic number of ionizing photons produced by massive stars (Q) and the production efficiency of ionizing photons ($\xi_{\rm ion} = Q/L_{\rm UV}$). Extrapolating from the CLASSY stellar continuum fits, we will predict $\xi_{\rm ion}$ and investigate the correlation with UV emission lines (e.g., Jaskot & Ravindranath 2016; Schaerer et al. 2018; Ravindranath et al. 2020). Finally, the comparisons between the FUV reddening and the reddening from the optical emission lines will inform about complex geometries and the origin of dust extinction. These results can then be compared to predictions from simulations to test how galaxies contribute to reionization (e.g., Fletcher et al. 2019; Finkelstein et al. 2019).

Theoretical arguments and small observational samples suggest that UV nebular emission and absorption features trace the escape fraction. CLASSY will indirectly infer escape fractions of a statistically significant sample using UV diagnostics accessible by ELTs and JWST: Lyα emission (Verhamme et al. 2015; Steidel et al. 2018; Izotov et al. 2018), the depth of low-ionization absorption lines (Heckman et al. 2011; Chisholm et al. 2018), and the strength of high-ionization emission lines (Nakajima et al. 2018). The middle left panel of Figure 9 demonstrates that the CLASSY absorption lines estimate the porosity (or covering fraction) of the foreground neutral gas. In this example, the high S/N data suggests that the Si II gas does not fully cover the background stellar continuum because the flux never reaches a value of zero. This implies that there are small regions of the stellar emission that propagate out of J1416+1223 without being absorbed by Si ions. Similarly, the `tlac` Lyα models in the middle right of Figure 9 emphasize how the neutral gas geometries can be estimated from the CLASSY profiles. These constraints will illustrate the neutral gas content in galaxies and provide a template to determine the escape of Lyα and ionizing photons at high redshift.

7. Summary

We have presented a new spectral atlas consisting of high-resolution, high-S/N contiguous FUV spectra of 45 local star-forming galaxies obtained with HST/COS as part of the COS Legacy Archival Spectroscopic Survey (CLASSY). As a result, the CLASSY atlas reaches far beyond the previous FUV spectral libraries. One of the considerable strengths of the CLASSY project is the careful selection of the sample so that the value of the existing HST archival spectra was maximized. As such, the CLASSY atlas was constructed from 94 archival spectra from 177 orbits and 76 new spectra from 135 orbits (170 spectra total from 312 orbits) of HST observations, or more than 600 total COS spectral images. Further, we uniformly reduced and coadded the combined archival and new observations of the CLASSY atlas, producing full far-UV spectra that allow a large number and broad range of scientific analyses to follow. The resulting CLASSY spectral atlas is the first of the CLASSY Treasury high-level science products to be made publicly available to the astronomical community via the CLASSY HLSP website, https://archive.stsci.edu/hlsp/classy, and the CLASSY MAST portal, https://mast.stsci.edu/search/ui/#/classy.

We have also compiled an ancillary set of high-quality optical spectra and photometry and used them to derive updated galaxy properties for the CLASSY galaxies. As a result, we report the properties for the CLASSY sample that span broad ranges in stellar mass ($6.2 < \log M_\star/M_\odot < 10.1$), SFR ($-2.0 < \log$ SFR ($M_\odot$ yr^{-1}) $< +1.6$), direct gas-phase metallicity ($7.0 < 12+\log({\rm O/H}) < 8.8$), ionization ($0.5 < {\rm O}_{32} < 38.0$), reddening ($0.01 < E(B-V) < 0.12$), and nebular density ($10 < n_e$ (cm^{-3}) < 1120). With these data, we showed that the CLASSY sample is consistent with the typical evolution of star-forming galaxies along the MZR in the Local Volume, but seems to be currently experiencing a strong burst of star formation that mimics the SFRs of moderate- to high-redshift galaxies. Thus, the CLASSY spectral templates provide a unique data set to study both local star-forming galaxies due to the specific spatial scales that they probe and distant galaxies due to their enhanced SFRs.

Looking to the future, the CLASSY Treasury will provide a suite of high-level science products to help the community prepare for future observatories and empirically connect the stellar and gas-phase properties of star-forming galaxies for the first time using a suite of UV absorption and emission line diagnostics, added to optical emission line measurements.

The CLASSY team thanks the referee for thoughtful feedback that significantly improved both the paper and the HLSPs. D.A.B. is grateful for the support for this program, HST-GO-15840, that was provided by NASA through a grant from the Space Telescope Science Institute, which is operated by the Associations of Universities for Research in Astronomy, Incorporated, under NASA contract NAS5-26555. B.L.J. is grateful for support from the European Space Agency (ESA). The CLASSY collaboration extends special gratitude to the Lorentz Center for useful discussions during the "Characterizing Galaxies with Spectroscopy with a view for JWST" 2017 workshop that led to the formation of the CLASSY collaboration and survey.

Funding for SDSS-III has been provided by the Alfred P. Sloan Foundation, the Participating Institutions, the National

Science Foundation, and the U.S. Department of Energy Office of Science. The SDSS-III website is http://www.sdss3.org/.

SDSS-III is managed by the Astrophysical Research Consortium for the Participating Institutions of the SDSS-III Collaboration including the University of Arizona, the Brazilian Participation Group, Brookhaven National Laboratory, Carnegie Mellon University, University of Florida, the French Participation Group, the German Participation Group, Harvard University, the Instituto de Astrofisica de Canarias, the Michigan State/Notre Dame/JINA Participation Group, Johns Hopkins University, Lawrence Berkeley National Laboratory, Max Planck Institute for Astrophysics, Max Planck Institute for Extraterrestrial Physics, New Mexico State University, New York University, Ohio State University, Pennsylvania State University, University of Portsmouth, Princeton University, the Spanish Participation Group, University of Tokyo, University of Utah, Vanderbilt University, University of Virginia, University of Washington, and Yale University.

This work also uses the services of the ESO Science Archive Facility, observations collected at the European Southern Observatory under ESO programmes 096.B-0690, 0103.B-0531, 0103.D-0705, and 0104.D-0503, and observations obtained with the Large Binocular Telescope (LBT). The LBT is an international collaboration among institutions in the United States, Italy, and Germany. LBT Corporation partners are as follows: The University of Arizona on behalf of the Arizona Board of Regents; Istituto Nazionale di Astrofisica, Italy; LBT Beteiligungsgesellschaft, Germany, representing the Max-Planck Society, The Leibniz Institute for Astrophysics Potsdam, and Heidelberg University; The Ohio State University, University of Notre Dame, University of Minnesota, and University of Virginia.

This paper made use of the modsIDL spectral data reduction pipeline developed in part with funds provided by NSF grant AST-1108693 and a generous gift from OSU Astronomy alumnus David G. Price through the Price Fellowship in Astronomical Instrumentation. This research has made use of the HSLA database, developed and maintained at STScI, Baltimore, USA.

Facilities: HST (COS), LBT (MODS), Astrophysical Observatory of the Smithsonian Institution (APO;SDSS), KECK (ESI), Very Large Telescope (MUSE, VIMOS).

Software: astropy (The Astropy Collaboration 2013, 2018); BEAGLE (Chevallard & Charlot 2016); CalCOS (STScI); dustmaps (Green 2018); jupyter (Kluyver et al. 2016); LINMIX (Kelly 2007); MPFIT (Markwardt 2009); MODS reduction Pipeline, Photutils (Bradley et al. 2021); PYNEB (Luridiana et al. 2012, 2015); python, pysynphot (STScI Development Team et al. 2013); RASCAS (Michel-Dansac et al. 2020); SALT (Scarlata & Panagia 2015); STARLIGHT (Fernandes 2005); tlac (Gronke & Dijkstra 2014); XIDL.

Appendix A
CLASSY FUV+Optical Spectral Observations

Here we present the details of the CLASSY FUV HST/COS spectroscopic observations in Tables 2 and 3 and the optical spectroscopic observations in Table 4.

Table 2
CLASSY New+Archival HST/COS Observations

			NUV Acq. Images					FUV Spectra					
Target	z_{em}	PID	Data Set	t_{exp} (s)	Mirror	PA (deg)	GFWHM (″)	Dataset	Grating	λ_{cen} (Å)	LP	t_{exp} (s)	Rest λ (Å)
1. J0021+0052	0.09839	13017	lc3402s0q	400	B	111	NA	LC3402010	G130M	1291	2	1060	1031.2−1305.7
							NA	LC3402020	G160M	1611	2	2379	1291.7−1629.6
		15840	le2404uwq	43	A	110	0.32	LE2404020	G185M	1913	NA	882	1631.0−1855.1
							0.32	LE2404010	G185M	1986	NA	881	1702.2−1923.8
													1031.2–1923.8
2. J0036−3333	0.02060	13017	lc3401luq	30	B	259	NA	LC3401010	G130M	1309	2	1536	1128.6−1423.8
							0.24	LC3401020	G160M	1623	2	2363	1402.0−1765.3
		15840	le2401j0q	22	A	88	0.23	LE2401010	G185M	1835	NA	944	1679.9−1923.7
													1128.6–1923.7
3. J0127−0619	0.00540	15840	le2446ieq	55	A	106	0.12	LE2446030	G130M	1291	4	2384	1124.4−1420.8
							0.12	LE2446020	G160M	1600	4	2868	1399.5−1768.3
							0.12	LE2446010	G185M	1913	NA	968	1782.7−2031.0
													1124.4–2031.0
4. J0144+0453	0.00520	15840	le2430coq	162	A	111	1.02	LE2430010	G130M	1291	4	6821	1125.4−1421.7
		14679	ld9p05peq	88	A	283	0.94	LD9P05020	G160M	1623	4	2604	1423.2−1792.4
							0.94	LD9P05010	G185M	1921	NA	2108	1789.5−2037.5
													1125.4–2037.5
5. J0337−0502	0.01352	15193	ldn759r8q	40	A	303	0.38	LDN759010	G130M	1222	4	4580	1052.0−1348.8
			ldn709pnq	40	A	132	0.67	LDN709020	G160M	1623	4	5604	1411.3−1777.8
			ldn759r8q	40	A	303	0.38	LDN759020	G160M	1623	4	5344	1411.3−1777.5
							0.47	LCNE03020	G185M	1835	NA	5674	1688.7−1937.7
		13788	lcne03sgq	510	B	129	NA	lcne03skq	G160M	1611	3	4958	1399.9−1765.9
								lcne03tzq	G185M	1835	NA	5764	1688.7−1937.7
													1052.0–1937.7
6. J0405−3648	0.00280	15840	le2426tiq	221	A	1	1.38	LE2426010	G130M	1291	4	9463	1128.6−1425.0
		14679	ld9p51t5q	88	A	231	1.06	LD9P51020	G160M	1623	4	2664	1426.6−1796.6
								LD9P51010	G185M	1913	NA	2164	1786.8−2036.1
													1128.6–2036.1
7. J0808+3948	0.09123	11727	lb5b03fuq	93	B	231	NA	LB5B03010	G130M	1291	1	5510	1038.0−1314.0
								LB5B03020	G160M	1577	1	6080	1268.9−1607.4
		15840	le2455wgq	87	A	327	0.10	LE2455020	G185M	1900	NA	2304	1627.9−1857.2
								LE2455010	G185M	1971	NA	1764	1695.1−1922.0
													1038.0–1922.0
8. J0823+2806	0.04722	13017	lc3403djq	400	B	136	NA	LC3403010	G130M	1222	2	1059	1018.2−1305.5
								LC3403020	G160M	1577	2	2379	1321.3−1675.1
		15840	le2403ggq	72	A	350	0.29	LE2403010	G185M	1986	NA	1788	1781.5−2017.6
													1018.2–2017.6
9. J0926+4427	0.18067	11727	lb5b05mwq	85	A	338	0.21	LB5B05010	G130M	1300	1	5640	967.7−1222.8
								LB5B05020	G160M	1611	1	6180	1202.2−1515.5
		15840	le2411zjq	72	A	60	0.17	LE2411030	G185M	1835	NA	4928	1449.0−1662.8

Table 2
(Continued)

Target	z_{em}	PID	NUV Acq. Images					FUV Spectra					
			Data Set	t_{exp} (s)	Mirror	PA (deg)	GFWHM (″)	Dataset	Grating	λ_{cen} (Å)	LP	t_{exp} (s)	Rest λ (Å)
								LE2411020	G185M	1864	NA	2304	1474.1−1687.1
							0	LE2411010	G225M	2339	NA	1864	1883.4−2080.6
													967.7–2080.6
10. J0934+5514	0.0025	15193	ldn707a5q	44	A	142	1.35	LDN707010	G130M	1222	1	2352	1063.6−1363.8
		11579	lb7h71btq	44	A	75	1.17	LB7H71010	G130M	1291	1	7761	1129.8−1430.3
			lb7h72ucq	44	A	75		LB7H72010	G130M	1291	4	7761	1129.7−1430.3
		11523	ACQ/SEARCH			341		LB6L1A030	G130M	1291	4	3409	1129.8−1425.4
								LB6L2A0C0	G160M	1589	4	1768	1395.9−1755.6
								LB6L2A0D0	G160M	1600	4	1530	1407.3−1767.0
								LB6L2A0E0	G160M	1611	4	2140	1418.8−1778.6
								LB6L2A0F0	G160M	1623	4	1872	1430.9−1790.7
								LB6L2A0G0	G185M	1900	NA	2098	1772.1−2016.1
								LB6L2A0H0	G185M	1913	NA	4049	1787.1−2030.7
								LB6L2A0I0	G185M	1921	NA	1949	1794.5−2037.8
													1063.6–2037.8
11. J0938+5428	0.1021	11727	lb5b02qjq	162	B	17	0.36	LB5B02010	G130M	1291	1	2280	1027.9−1301.0
								LB5B02020	G160M	1600	1	2990	1277.2−1612.8
		15840	le2417hlq	87	A	109	0.27	LE2417010	G185M	1921	NA	1780	1632.7−1859.0
								LE2417020	G185M	2010	NA	2320	1716.0−1939.5
													1027.9–1939.5
12. J0940+2935	0.00168	15840	le2427rpq	156	A	83	1.29	LE2427010	G130M	1291	4	6863	1129.6−1426.6
		14679	ld9p06ejq	88	A	245	1.26	LD9P06020	G160M	1623	4	2624	1428.1−1798.6
								LD9P06010	G185M	1913	NA	2124	1788.1−2037.8
													1129.6–2037.8
13. J0942+3547	0.01486	15099	ldna02ciq	99	A	321	0.19	LDNA02010	G130M	1291	4	10,754	1115.4−1408.1
		14168	lcy410baq	92	A	112	0.18	LCY410020	G160M	1623	3	2664	1410.1−1775.5
								LCY410010	G185M	1835	NA	2156	1685.8−1934.8
													1115.4–1934.8
14. J0944−0038	0.00478	15840	le2422p1q	223	A	222	0.67	LE2422010	G130M	1291	4	4319	1129.9−1422.2
		14120	lcyc01koq	38	B	329	NA	LCYC01010	G160M	1589	3	5083	1389.4−1757.5
		14168	lcy408buq	43	A	334	0.63	LCY408020	G160M	1623	3	2577	1424.3−1793.5
								LCY408010	G185M	1921	NA	2168	1790.4−2038.6
		15646	ldxt03e2q	43	A	147	0.66	LDXT03010	G160M	1533	4	13,463	1335.6−1693.9
								LDXT04010	G160M	1533	4	13,463	1335.6−1693.9
		15840	le2456s7q	223	A	222	0.67	LE2456010	G130M	1291	4	1767	1127.1−1419.3
													1127.1–2038.6
15. J0944+3442	0.02005	15840	le2448cbq	91	A	94	1.00	LE2448030	G130M	1291	4	3105	1109.1−1400.5
							1.00	LE2448020	G160M	1623	4	3820	1402.5−1766.3
							1.00	LE2448010	G185M	1835	NA	1756	1677.6−1925.2
													1109.1–1925.2

Table 2
(Continued)

Target	z_{em}	PID	NUV Acq. Images					FUV Spectra					
			Data Set	t_{exp} (s)	Mirror	PA (deg)	GFWHM (″)	Dataset	Grating	λ_{cen} (Å)	LP	t_{exp} (s)	Rest λ (Å)
16. J1016+3754	0.00388	15840	le2441hbq	NA	B	94	NA	LE2441020	G130M	1291	4	1138	1127.3−1423.4
		14120	lcyc02s4q	69	B	350	NA	LCYC02010	G160M	1589	3	5216	1390.1−1759.0
		15840		NA			NA	LE2441010	G185M	1913	NA	356	1784.2−2033.2
		15220	ldkm07jxq	8	B	10	NA	LDKM07010	G140L	1105	4	2267	1103.8−2267.2
													1103.8–2267.2
17. J1024+0524	0.03319	15840	le2421rsq	54	A	166	0.26	LE2421010	G130M	1222	4	4296	1032.2−1323.4
		14168	lcy409aoq	75	A	331	0.42	LCY409020	G160M	1577	3	2608	1339.3−1697.8
								LCY409010	G185M	1971	NA	2136	1790.5−2030.1
													1032.2–2030.1
18. J1025+3622	0.1265	13017	lc3405fdq	200	A	7	0.65	LC3405020	G130M	1300	2	2368	1013.7−1281.5
								LC3405010	G160M	1623	2	4400	1270.0−1599.4
		15840	le2410obq	109	A	166	0.52	LE2410020	G185M	1864	NA	2304	1543.9−1767.3
								LE2410010	G225M	2233	NA	7248	1880.4−2089.4
													1013.7–2089.4
19. J1044+0353	0.01287	15840	le2438aaq	146	A	162	0.78	LE2438010	G130M	1291	4	6853	1117.0−1410.9
		15646	ldxt07acq	183	A	338	0.77	LDXT07010	G160M	1533	4	13,182	1322.3−1687.7
		15465	ldsz01v6q	183	A	320	0.78	LDSZ01010	G160M	1589	4	6438	1377.3−1743.3
		15220	ldkm01f5q	0.6	A	319	0.84	LDKM01010	G140L	1105	4	2220	1094.1−2246.4
		13312	ACQ/PEAKD	203	A	320	NA	lcaw13enq	G140L	1280	3	2066	1234.7−2404.9
													1094.1–2404.9
20. J1105+4444	0.02154	15840	le2440kuq	54	B	89	0.64	LE2440020	G130M	1222	4	2388	1044.1−1333.5
		14120	lcyc10ehq	20	B	43	1.09	LCYC10010	G160M	1589	3	8461	1366.3−1728.7
		15840	le2440kuq	54	B	89	0.64	LE2440010	G185M	1941	NA	1828	1780.9−2024.5
													1044.1–2024.5
21. J1112+5503	0.13164	13017	lc3408mbq	150	A	71	0.18	LC3408020	G130M	1300	2	2404	1009.1−1275.5
								LC3408010	G160M	1623	2	4572	1264.5−1592.3
													1009.1–1592.3
22. J1119+5130	0.00446	15840	le2428a2q	83	A	33	0.89	LE2428010	G130M	1291	4	4322	1126.6−1422.5
		14679	ld9p03zzq	88	A	85	1.42	LD9P03020	G160M	1623	4	2800	1424.2−1793.6
								LD9P03010	G185M	1921	NA	2300	1789.1−2037.4
		15220	ldkm05ugq	13	B	173	NA	LDKM05010	G140L	1105	4	2363	1101.8−2265.6
													1101.8–2265.6
23. J1129+2034	0.0047	15840	le2423c2q	146	A	139	0.23	LE2423010	G130M	1291	4	6885	1126.3−1422.4
		14168	lcy402bsq	53	A	6	0.46	LCY402020	G160M	1623	3	2588	1424.4−1793.4
							0.46	LCY402010	G185M	1817	NA	2160	1685.1−1936.9
													1126.3–1936.9
24. J1132+5722	0.00504	15840	LE2429E7Q	369	A	9	0.91	LE2429010	G130M	1291	4	6675	1125.8−1421.8
		14679	ld9p02o8q	88	A	9	1.14	LD9P02020	G160M	1623	4	2852	1423.5−1792.8
								LD9P02010	G185M	1921	NA	2352	1790.0−2038.0
													1125.8–2038.0

Table 2
(Continued)

			NUV Acq. Images					FUV Spectra					
Target	z_{em}	PID	Data Set	t_{exp} (s)	Mirror	PA (deg)	GFWHM ($''$)	Dataset	Grating	λ_{cen} (Å)	LP	t_{exp} (s)	Rest λ (Å)
25. J1132+1411	0.01764	15840	le2432bnq	107	A	142	0.44	LE2432010	G130M	1291	4	4560	1112.3−1404.3
		15185	ldi202e4q	9	A	340	0.32	LDI202020	G160M	1623	3	2604	1405.3−1770.3
								LDI202010	G185M	1941	NA	2264	1785.3−2029.8
		15220	ldkm03wpq	15	B	309	NA	LDKM03010	G140L	1105	4	2415	1102.0−2264.2
													1102.9–2029.8
26. J1144+4012	0.12695	13017	lc3406eoq	200	A	165	0.62	LC3406020	G130M	1300	2	2376	1013.5−1280.8
								LC3406010	G160M	1623	2	4414	1270.1−1598.9
		15840	le2413acq	146	A	317	0.59	LE2413020	G185M	1864	NA	3962	1543.3−1766.5
								LE2413010	G225M	2233	NA	7929	1878.0−2088.4
													1013.5–2088.4
27. J1148+2546	0.04512	15840	le2424t3q	109	A	28	0.85	LE2424010	G130M	1222	4	4552	1020.3−1303.3
		14168	lcy405jhq	95	A	1	0.85	LCY405020	G160M	1589	3	2624	1335.8−1689.9
								LCY405010	G185M	1890	NA	2112	1691.0−1930.8
													1020.3–1930.8
28. J1150+1501	0.00245	15840	le2433i7q	46	B	146	0.79	LE2433010	G130M	1291	4	1970	1128.8−1425.6
		15185	ldi208k7q	42	B	333	0.78	LDI208010	G160M	1623	4	2120	1426.8−1797.1
			ldi203n6q	42	B	333	0.80	LDI203010	G185M	1913	NA	2200	1786.5−2036.0
													1128.8–2036.0
29. J1157+3220	0.01097	15840	le2439ygq	20	B	332	0.79	LE2439010	G130M	1291	4	801	1119.1−1413.3
		14120	lcyc09alq	11	B	344	0.78	LCYC09010	G160M	1589	3	8285	1380.7−1746.8
		15840	le2439ygq	20	B	332	0.79	LE2439020	G185M	1817	NA	660	1673.4−1923.7
													1119.1–1923.7
30. J1200+1343	0.06675	15840	le2449avq	170	A	125	0.17	LE2449010	G130M	1222	4	6790	999.7−1281.8
			le2450bvq	NA	A	125	NA	LE2450010	G160M	1623	4	11,488	1340.7−1688.9
			le2449avq	170	A	125	0.17	LE2449020	G185M	1941	NA	4914	1705.3−1938.5
													999.7–1938.5
31. J1225+6109	0.00234	14120	lcyc08s5q	37	A	27	0.81	LCYC08010	G160M	1589	4	5698	1392.4−1761.8
		15840	le2443l2q	30	A	131	0.83	LE2443020	G130M	1291	3	1202	1128.9−1425.6
								LE2443010	G185M	1900	NA	404	1772.4−2022.2
													1128.9–2022.2
32. J1253−0312	0.02272	15840	le2447gaq	73	A	−22	0.29	LE2447030	G130M	1291	4	2380	1105.2−1396.5
								LE2447020	G160M	1623	4	2848	1398.7−1761.5
								LE2447010	G185M	1941	NA	936	1779.1−2022.2
													1105.2–2022.2
33. J1314+3452	0.00288	15840	le2434txq	259	A	66	0.45	LE2434010	G130M	1291	4	9387	1128.5−1424.7
		15185	ldi205aeq	81	B	120	0.59	LDI205020	G160M	1623	4	2496	1426.4−1796.7
								LDI205010	G185M	1913	NA	2084	1785.3−2034.6
													1128.5–2034.6

Table 2
(Continued)

			NUV Acq. Images					FUV Spectra					
Target	z_{em}	PID	Data Set	t_{exp} (s)	Mirror	PA (deg)	GFWHM (″)	Dataset	Grating	λ_{cen} (Å)	LP	t_{exp} (s)	Rest λ (Å)
34. J1323−0132	0.02246	15840	le2444esq	202	A	338	0.18	LE2444010	G130M	1291	4	6913	1106.7−1397.5
			le2445h5q	202	A	337	0.19	LE2445010	G160M	1623	4	11,391	1398.8−1761.9
			le2444esq	202	A	338	0.18	LE2444020	G185M	1941	NA	4906	1778.5−2022.0
		14628	ldaf11hnq	226	A	355	0.18	LDAF11010	G140L	1280	3	1791	1232.3−2380.1
													1106.7–2380.1
35. J1359+5726	0.03383	12583	lbqe05cbq	139	B	59	0.99	LBQE05010	G130M	1327	1	2166	1135.3−1424.1
		14120	lcyc03l9q	88	B	201	0.84	LCYC03010	G160M	1589	3	8647	1350.1−1708.3
		15840	le2402hpq	89	B	176	0.79	LE2402010	G185M	1864	NA	1776	1684.2−1927.5
		13761	lcp153pgq		B	94	NA	LCP153010	G140L	1105	3	600	1075.0−2164.4
													1075.0–2164.4
36. J1416+1223	0.12316	13017	lc3410ckq	100	A	151	0.15	LC3410020	G130M	1291	2	2379	1008.3−1276.8
								LC3410010	G160M	1611	2	4636	1263.4−1593.7
		15840	le2409s2q	72	A	149	0.15	LE2409010	G185M	1953	NA	1863	1632.5−1851.9
								LE2409020	G225M	2233	NA	2382	1887.4−2097.2
													1008.3–2097.2
37. J1418+2102	0.00855	15840	le2437uqq	159	A	159	0.37	LE2435010	G130M	1291	4	9589	1121.7−1417.0
								LE2437010	G130M	1291	4	6859	1121.7−1416.9
		15465	ldsz02ixq	153	A	326	0.40	LDSZ02010	G160M	1589	4	12,373	1382.9−1750.7
		14628	ldaf02b0q	153	A	133	0.45	LDAF02010	G140L	1280	3	1947	1233.5−2414.6
													1121.7–2414.6
38. J1428+1653	0.18167	13017	lc3411zlq	200	A	182	0.33	LC3411020	G130M	1300	2	2380	966.6−1221.7
								LC3411010	G160M	1611	2	4424	1200.9−1514.8
		15840	le2412bjq	109	A	170	0.25	LE2412020	G185M	1835	NA	6362	1449.9−1661.9
			le2453f9q	109	A	170	0.25	LE2453010	G185M	1864	NA	4332	1473.0−1686.0
			le2412bjq	109	A	170	0.25	LE2412010	G225M	2250	NA	3090	1808.3−2006.9
													966.6–2006.9
39. J1429+0643	0.17350	13017	lc3409v4q	100	A	148	0.16	LC3409020	G130M	1300	2	2380	973.2−1230.0
								LC3409010	G160M	1600	2	4636	1199.1−1515.1
		15840	le2416s0q	146	A	153	0.16	LE2416020	G185M	1941	NA	4914	1550.0−1762.1
								LE2416010	G225M	2233	NA	7024	1804.8−2006.9
													973.2–2006.9
40. J1444+4237	0.00230	15840	le2425mmq	110	A	71	0.78	LE2425010	G130M	1291	4	4566	1129.3−1425.6
		14679	ld9p04nmq	88	A	298	0.90	LD9P04020	G160M	1623	3	2672	1427.5−1797.8
								LD9P04010	G185M	1913	NA	2204	1786.5−2035.9
		15646	ldxt05r3q	88	A	256	0.79	LDXT05010	G160M	1533	4	13,852	1336.4−1705.7
													1129.3–2035.9
41. J1448−0110	0.02741	15840	le2431f0q	80	A	153	0.22	LE2431010	G130M	1222	4	4590	1038.2−1326.0
		15185	ldi209scq	7	A	328	0.21	LDI209020	G160M	1623	4	2596	1392.3−1753.6
								LDI209010	G185M	1953	NA	2260	1781.1−2022.6
													1038.2–2022.6

Table 2
(Continued)

			NUV Acq. Images					FUV Spectra					
Target	z_{em}	PID	Data Set	t_{exp} (s)	Mirror	PA (deg)	GFWHM ($''$)	Dataset	Grating	λ_{cen} (Å)	LP	t_{exp} (s)	Rest λ (Å)
42. J1521+0759	0.09426	13017	lc3412imq	100	A	340	0.36	LC3412020	G130M	1222	2	2379	974.2−1249.1
								LC3412010	G160M	1600	2	4636	1285.7−1624.6
		15840	le2406ieq	87	A	157	0.37	LE2406020	G185M	1921	NA	2300	1644.0−1872.0
								LE2406010	G185M	1986	NA	1760	1705.1−1931.1
													974.2–1931.1
43. J1525+0757	0.07579	13017	lc3404glq	400	B	155	0.27	LC3404010	G130M	1222	2	1059	991.2−1270.8
								LC3404020	G160M	1611	2	2379	1319.0−1663.7
		15840	le2407c8q	72	A	156	0.23	LE2407020	G185M	1890	NA	2300	1644.4−1877.4
								LE2407010	G185M	1941	NA	1784	1690.9−1922.4
													991.2–1922.4
44. J1545+0858	0.03772	15840	le2442y5q	72	A	154	0.38	LE2442020	G130M	1222	4	2787	1030.0−1317.7
		14120	lcyc04oqq	93	A	103	0.45	LCYC04010	G160M	1589	3	4915	1345.2−1702.0
		15840	le2442y5q	72	A	154	0.38	LE2442010	G185M	1971	NA	1215	1784.3−2021.1
													1030.0–2021.1
45. J1612+0817	0.14914	13017	lc3413klq	100	A	342	0.16	LC3413020	G130M	1318	2	2380	1010.3−1272.9
								LC3413010	G160M	1611	2	4636	1234.7−1557.4
		15840	le2414m2q	109	A	160	0.17	LE2414020	G185M	1900	NA	2300	1545.8−1763.7
								LE2414010	G225M	2283	NA	4505	1889.3−2092.4
													1010.3–2092.4

Note. Details of the complete set of archival and new HST/COS observations used for the CLASSY Treasury are listed here. The program IDs (PIDs) for both archival and new observations are listed in column (3). For each PID, the details of the relevant NUV acquisition images are provided, with the data set ID in column (4), the exposure time in column (5), the mirror used in column (6), and the position angle (PA) of the aperture in column (7), and the GFWHM measured from the spatial NUV light profile in column (8). Subsequently, the details of the corresponding FUV spectral data sets are listed; the data set ID is given in column (8), the grating and wavelength settings used are listed in columns (9) and (10), the detector lifetime position (LP) is given in column (12), the total exposure times are in column (13), and the rest-frame wavelength coverage is noted in column (14). The full extent of the contiguous wavelength coverage is bolded in the last row for each galaxy.

(This table is available in machine-readable form.)

Table 3
Nominal and Measured Spectral Resolution of CLASSY Coadded Spectra

Target	Wavelength (Å)	Nominal Resolution (km s^{-1}/resel)				Measured Resolution (km s^{-1}/resel)
		VHR	HR	MR	LR	
1. J0021+0052	1260	14.3	17.4	47.6	119.6	42
2. J0036−3333	1260	14.3	17.4	47.6	119.6	128
3. J0127−0619	1334	13.5	16.4	45.0	112.0	74
4. J0144+0453	1334	13.5	16.4	45.0	112.0	74
5. J0337−0502	1334	13.5	16.4	45.0	112.0	20
6. J0405−3648	1334	13.5	16.4	45.0	112.0	65
7. J0808+3948	1334	13.5	16.4	45.0	112.0	40
8. J0823+2806	1334	13.5	16.4	45.0	112.0	67
9. J0926+4427	1260	14.3	17.4	47.6	119.6	71
10. J0934+5514	1334	13.5	16.4	45.0	112.0	105
11. J0938+5428	1334	13.5	16.4	45.0	112.0	67
12. J0940+2935	1260	14.3	17.4	47.6	119.6	88
13. J0942+3547	1260	14.3	17.4	47.6	119.6	66
14. J0944−0038	1260	14.3	17.4	47.6	119.6	71
15. J0944+3442	1334	13.5	16.4	45.0	112.0	101
16. J1016+3754	1260	14.3	17.4	47.6	119.6	71
17. J1024+0524	1260	14.3	17.4	47.6	119.6	71
18. J1025+3622	1260	14.3	17.4	47.6	119.6	52
19. J1044+0353	1394	12.9	15.7	43.0	107.2	79
20. J1105+4444	1548	11.6	14.2	38.8	96.5	52
21. J1112+5503	1260	14.3	17.4	47.6	119.6	61
22. J1119+5130	1260	14.3	17.4	47.6	119.6	71
23. J1129+2034	1334	13.5	16.4	45.0	112.0	33
24. J1132+5722	1260	14.3	17.4	47.6	119.6	71
25. J1132+1411	1260	14.3	17.4	47.6	119.6	71
26. J1144+4012	1334	13.5	16.4	45.0	112.0	112
27. J1148+2546	1334	13.5	16.4	45.0	112.0	67
28. J1150+1501	1334	13.5	16.4	45.0	112.0	85
29. J1157+3220	1334	13.5	16.4	45.0	112.0	67
30. J1200+1343	1334	13.5	16.4	45.0	112.0	83
31. J1225+6109	1548	11.6	14.2	38.8	96.5	58
32. J1253−0312	1548	11.6	14.2	38.8	96.5	50
33. J1314+3452	1260	14.3	17.4	47.6	119.6	45
34. J1323−0132	1548	11.6	14.2	38.8	96.5	40
35. J1359+5726	1548	11.6	14.2	38.8	96.5	42
36. J1416+1223	1548	11.6	14.2	38.8	96.5	46
37. J1418+2102	1548	11.6	14.2	38.8	96.5	46
38. J1428+1653	1548	11.6	14.2	38.8	96.5	65
39. J1429+0643	1548	11.6	14.2	38.8	96.5	65
40. J1444+4237	1548	11.6	14.2	38.8	96.5	32
41. J1448−0110	1548	11.6	14.2	38.8	96.5	61
42. J1521+0759	1548	11.6	14.2	38.8	96.5	65
43. J1525+0757	1548	11.6	14.2	38.8	96.5	54
44. J1545+0858	1548	11.6	14.2	38.8	96.5	61
45. J1612+0817	1548	11.6	14.2	38.8	96.5	50

Note. Comparison of the nominal (i.e., point-source) spectral resolution of the CLASSY coadded spectra to the measured resolution from Milky Way ISM absorption lines. The best Milky Way ISM feature for each galaxy is listed in column (2), followed by the nominal resolution at that wavelength in kilometers per second per resolution element for each coadded data set in columns (3)–(6). Finally, column (7) lists the Gaussian FWHM in km s^{-1} measured from the HR, Galactic extinction-corrected, binned spectra (extension 9).

(This table is available in machine-readable form.)

Table 4
Ancillary Optical Spectra for the CLASSY Galaxy Sample

Target	Telescope/ Spectrograph	Aperture	Exposure Time (s)	Reference
1. J0021+0052	VLT/MUSE	2.″5 circ.	2449	ESO 0104.D-0503; PI Anderson
2. J0036−3333	VLT/MUSE	2.″5 circ.	2800	ESO 096.B-0923; PI Östlin
3. J0127−0619	VLT/VIMOS	2.″5 circ.	1608, 1488	James et al. (2009)
4. J0144+0453	MMT/BC	1″ × 180″	6300	Senchyna et al. (2019)
5. J0337−0502	VLT/MUSE	2.″5 circ.	5680	ESO 096.B-0690; PI Hayes
6. J0405−3648	VLT/MUSE	2.″5 circ.	2000	ESO 0103.D-0705; PI Brinchmann
7. J0808+3948	LBT/MODS	1″ × 60″	2700	This work
8. J0823+2806	APO/SDSS	3″ circ.	2700	Eisenstein et al. (2011)
9. J0926+4427	APO/SDSS	3″ circ.	2700	Eisenstein et al. (2011)
10. J0934+5514	Keck/KCWI	2.″5 circ.	1200	Rickards Vaught et al. (2021)
11. J0938+5428	APO/SDSS	3″ circ.	2700	Eisenstein et al. (2011)
12. J0940+2935	APO/SDSS	3″ circ.	2700	Eisenstein et al. (2011)
13. J0942+3547	Keck/ESI	1″ × 60″	2700	R. L. Sanders et al. (2022), in preparation
14. J0944−0038	Keck/ESI	1″ × 60″	2700	R. L. Sanders et al. (2022), in preparation
15. J0944+3442	LBT/MODS	1″ × 60″	2700	This work
16. J1016+3754	APO/SDSS	3″ circ.	2700	Eisenstein et al. (2011)
17. J1024+0524	Keck/ESI	1″ × 60″	2700	R. L. Sanders et al. (2022), in preparation
18. J1025+3622	APO/SDSS	3″ circ.	2700	Eisenstein et al. (2011)
19. J1044+0353	VLT/MUSE	2.″5 circ.	4864	ESO 0103.B-0531; PI Erb
20. J1105+4444	APO/SDSS	3″ circ.	2700	Eisenstein et al. (2011)
21. J1112+5503	APO/SDSS	3″ circ.	2700	Eisenstein et al. (2011)
22. J1119+5130	MMT/BC	1″ × 180″	4500	Senchyna et al. (2019)
23. J1129+2034	Keck/ESI	1″ × 60″	2700	R. L. Sanders et al. (2022), in preparation
24. J1132+5722	MMT/BC	1″ × 180″	5400	Senchyna et al. (2019)
25. J1132+1411	APO/SDSS	3″ circ.	2700	Eisenstein et al. (2011)
26. J1144+4012	APO/SDSS	3″ circ.	2700	Eisenstein et al. (2011)
27. J1148+2546	Keck/ESI	1″ × 60″	2700	R. L. Sanders et al. (2022), in preparation
28. J1150+1501	APO/SDSS	3″ circ.	2700	Eisenstein et al. (2011)
29. J1157+3220	APO/SDSS	3″ circ.	2700	Eisenstein et al. (2011)
30. J1200+1343	APO/SDSS	3″ circ.	2700	Eisenstein et al. (2011)
31. J1225+6109	APO/SDSS	3″ circ.	2700	Eisenstein et al. (2011)
32. J1253−0312	APO/SDSS	3″ circ.	2700	Eisenstein et al. (2011)
33. J1314+3452	APO/SDSS	3″ circ.	2700	Eisenstein et al. (2011)
34. J1323−0132	APO/SDSS	3″ circ.	2700	Eisenstein et al. (2011)
35. J1359+5726	APO/SDSS	3″ circ.	2700	Eisenstein et al. (2011)
36. J1416+1223	APO/SDSS	3″ circ.	2700	Eisenstein et al. (2011)
37. J1418+2102	VLT/MUSE	2.″5 circ.	4864	ESO 0103.B-0531; PI Erb
38. J1428+1653	APO/SDSS	3″ circ.	2700	Eisenstein et al. (2011)
39. J1429+0643	APO/SDSS	3″ circ.	2700	Eisenstein et al. (2011)
40. J1444+4237	MMT/BC	1″ × 180″	6300	Senchyna et al. (2019)
41. J1448−0110	APO/SDSS	3″ circ.	2700	Eisenstein et al. (2011)
42. J1521+0759	APO/SDSS	3″ circ.	2700	Eisenstein et al. (2011)
43. J1525+0757	APO/SDSS	3″ circ.	2700	Eisenstein et al. (2011)
44. J1545+0858	LBT/MODS	1″ × 60″	2700	This work
45. J1612+0817	APO/SDSS	3″ circ.	2700	Eisenstein et al. (2011)

Note. Details of the best ancillary optical spectra available to accompany the CLASSY FUV spectra. The telescope and spectrograph of the observations are listed in column (2), and the cumulative exposure time is tabulated in column (4). The apertures listed in column (3) are the ones used to extract the spectra used in this work to determine the nebular properties of the CLASSY sample. For IFU observations, the 1D spectra were extracted to aperture-match the FUV HST/COS spectra. References in column (5) refer to the source of the observations.

(This table is available in machine-readable form.)

Appendix B
CLASSY Sample Properties

Here we present properties of the CLASSY sample galaxies that were derived from the ancillary optical spectra in Table 5 and `Beagle` SED fitting in Table 6. See Section 4 for details of the calculations. Additionally, we characterize the aperture bias of the CLASSY sample in Figure 10 by plotting the fraction of the optical flux measured (from the *u*- and *g*-band SDSS, DES, and PanSTARRS imaging) through a 2.″5 aperture relative to the total flux of the galaxy. The points in Figure 11 are color coded by their optical half-light radii, measured from the same imaging, showing that most of the CLASSY sample is relatively compact with 66% of the galaxies having $r_{50,\mathrm{opt.}} \lesssim 2.''0$. As demonstrated in Figure 2, the extent of the UV light is much more compact than the optical light of the CLASSY sample.

Table 5
CLASSY Galaxy Spectroscopy-derived Properties

Target	Alt. Name	R.A., Decl. (J2000)	z	$F_{\lambda1500}$	12+log(O/H)	n_e (cm^{-3})	O_{32}	$E(B-V)$
1. J0021+0052		00:21:01.03, +00:52:48.08	0.09839	3.94	8.17 ± 0.07 | T_e[O III]	120 ± 40	2.0 ± 0.1	0.131 ± 0.006
2. J0036−3333	Haro 11 knot	00:36:52.68, −33:33:17.24	0.02060	16.6	8.21 ± 0.17 | T_e[S III]	10 ± 10	1.1 ± 0.1	0.298 ± 0.012
3. J0127−0619	Mrk 996	01:27:35.51, −06:19:36.06	0.00540	4.04	7.68 ± 0.02 | T_e[O III]	400 ± 20	1.1 ± 0.1	0.476 ± 0.006
4. J0144+0453	UM133	01:44:41.36, +04:53:25.32	0.00520	1.87	7.76 ± 0.02 | T_e[O III]	40 ± 40	2.1 ± 0.1	0.044 ± 0.030
5. J0337−0502	SBS0335-052 E	03:37:44.06, −05:02:40.19	0.01352	7.99	7.46 ± 0.04 | T_e[S III]	140 ± 40	6.2 ± 0.2	0.053 ± 0.006
6. J0405−3648		04:05:20.46, −36:48:59.14	0.00280	0.96	7.04 ± 0.05 | T_e[S III]	10 ± 10	0.6 ± 0.1	0.106 ± 0.005
7. J0808+3948		08:08:44.28, +39:48:52.51	0.09123	3.42	8.77 ± 0.12 | T_e[N II]	910 ± 160	0.8 ± 0.1	0.241 ± 0.07
8. J0823+2806	LARS9	08:23:54.96, +28:06:21.60	0.04722	3.85	8.28 ± 0.01 | T_e[O III]	140 ± 10	2.0 ± 0.1	0.209 ± 0.004
9. J0926+4427	LARS14	09:26:00.44, +44:27:36.54	0.18067	1.14	8.08 ± 0.02 | T_e[O III]	130 ± 30	3.1 ± 0.1	0.104 ± 0.008
10. J0934+5514	I Zw 18 NW	09:34:02.02, +55:14:28.10	0.00250	15.1	6.98 ± 0.01 | T_e[O III]	120 ± 40	8.7 ± 0.1	0.073 ± 0.007
11. J0938+5428		09:38:13.49, +54:28:25.09	0.10210	3.56	8.25 ± 0.02 | T_e[O III]	80 ± 10	1.9 ± 0.1	0.129 ± 0.006
12. J0940+2935		09:40:12.87, +29:35:30.21	0.00168	1.45	7.66 ± 0.07 | T_e[O III]	10 ± 10	0.7 ± 0.1	0.060 ± 0.010
13. J0942+3547	CG-274, SB 110	09:42:52.78, +35:47:25.98	0.01486	3.80	8.13 ± 0.03 | T_e[O III]	20 ± 10	2.6 ± 0.1	0.055 ± 0.011
14. J0944−0038	CGCG007-025, SB 2	09:44:01.87, −00:38:32.18	0.00478	1.40	7.83 ± 0.01 | T_e[O III]	100 ± 20	2.9 ± 0.1	0.160 ± 0.010
15. J0944+3442		09:44:25.87, +34:42:08.49	0.02005	0.69	7.62 ± 0.11 | T_e[O III]	70 ± 60	1.4 ± 0.1	0.162 ± 0.013
16. J1016+3754	1427-52996-221	10:16:24.48, +37:54:46.08	0.00388	7.07	7.56 ± 0.01 | T_e[O III]	40 ± 20	4.6 ± 0.2	0.070 ± 0.012
17. J1024+0524	SB 36	10:24:29.25, +05:24:51.02	0.03319	4.50	7.84 ± 0.03 | T_e[O III]	20 ± 20	2.1 ± 0.1	0.101 ± 0.016
18. J1025+3622		10:25:48.38, +36:22:58.42	0.12650	1.81	8.13 ± 0.01 | T_e[O III]	100 ± 20	2.4 ± 0.1	0.090 ± 0.006
19. J1044+0353		10:44:57.79, +03:53:13.10	0.01287	1.70	7.45 ± 0.03 | T_e[S III]	200 ± 40	6.8 ± 0.1	0.079 ± 0.007
20. J1105+4444	1363-53053-510	11:05:08.16, +44:44:47.40	0.02154	4.68	8.23 ± 0.01 | T_e[O III]	100 ± 10	2.0 ± 0.1	0.167 ± 0.005
21. J1112+5503		11:12:44.05, +55:03:47.01	0.13164	1.91	8.45 ± 0.06 | T_e[N II]	390 ± 80	0.9 ± 0.1	0.225 ± 0.016
22. J1119+5130		11:19:34.36, +51:30:12.02	0.00446	2.63	7.57 ± 0.04 | T_e[O III]	10 ± 10	2.0 ± 0.1	0.095 ± 0.008
23. J1129+2034	SB 179	11:29:14.15, +20:34:52.01	0.00470	1.87	8.28 ± 0.04 | T_e[O III]	90 ± 20	1.8 ± 0.1	0.227 ± 0.011
24. J1132+5722	SBSG1129+576	11:32:02.64, +57:22:36.39	0.00504	2.57	7.58 ± 0.08 | T_e[O III]	120 ± 30	0.8 ± 0.1	0.095 ± 0.008
25. J1132+1411	SB 125	11:32:35.35, +14:11:29.83	0.01764	1.75	8.25 ± 0.01 | T_e[O III]	90 ± 20	2.7 ± 0.1	0.127 ± 0.008
26. J1144+4012		11:44:22.28, +40:12:21.19	0.12695	1.20	8.43 ± 0.20 | T_e[N II]	130 ± 30	0.6 ± 0.1	0.223 ± 0.010
27. J1148+2546	SB 182	11:48:27.34, +25:46:11.77	0.04512	2.07	7.94 ± 0.01 | T_e[O III]	120 ± 30	3.7 ± 0.1	0.096 ± 0.021
28. J1150+1501	SB 126, Mrk 0750	11:50:02.73, +15:01:23.48	0.00245	12.6	8.14 ± 0.01 | T_e[O III]	90 ± 10	2.3 ± 0.1	0.039 ± 0.004
29. J1157+3220	1991-53446-584	11:57:31.68, +32:20:30.12	0.01097	14.4	8.43 ± 0.02 | T_e[O III]	70 ± 10	1.2 ± 0.1	0.079 ± 0.006
30. J1200+1343		12:00:33.42, +13:43:07.95	0.06675	1.38	8.26 ± 0.02 | T_e[O III]	260 ± 30	5.1 ± 0.1	0.146 ± 0.006
31. J1225+6109	0955-52409-608	12:25:05.41, +61:09:11.30	0.00234	9.50	7.97 ± 0.01 | T_e[O III]	50 ± 20	4.7 ± 0.1	0.110 ± 0.005
32. J1253−0312	SHOC391	12:53:05.96, −03:12:58.84	0.02272	9.11	8.06 ± 0.01 | T_e[O III]	390 ± 50	8.0 ± 0.2	0.158 ± 0.008
33. J1314+3452	SB 153	13:14:47.37, +34:52:59.81	0.00288	3.72	8.26 ± 0.01 | T_e[O III]	180 ± 10	2.3 ± 0.1	0.140 ± 0.006
34. J1323−0132		13:23:47.52, −01:32:51.94	0.02246	1.33	7.71 ± 0.04 | T_e[O III]	600 ± 140	37.8 ± 3.0	0.128 ± 0.042
35. J1359+5726	Ly 52, Mrk 1486	13:59:50.88, +57:26:22.92	0.03383	6.34	7.98 ± 0.01 | T_e[O III]	60 ± 20	2.6 ± 0.1	0.091 ± 0.006
36. J1416+1223		14:16:12.87, +12:23:40.42	0.12316	2.62	8.53 ± 0.11 | T_e[N II]	270 ± 20	0.8 ± 0.1	0.246 ± 0.008
37. J1418+2102		14:18:51.12, +21:02:39.84	0.00855	1.17	7.75 ± 0.02 | T_e[S III]	50 ± 20	4.7 ± 0.1	0.084 ± 0.006
38. J1428+1653		14:28:56.41, +16:53:39.32	0.18167	1.25	8.33 ± 0.05 | T_e[O III]	90 ± 20	1.2 ± 0.1	0.144 ± 0.008
39. J1429+0643		14:29:47.00, +06:43:34.95	0.17350	1.62	8.10 ± 0.03 | T_e[O III]	230 ± 70	4.2 ± 0.2	0.116 ± 0.012
40. J1444+4237	HS1442+4250	14:44:11.46, +42:37:35.57	0.00230	2.08	7.64 ± 0.02 | T_e[O III]	90 ± 40	4.1 ± 0.1	0.081 ± 0.053
41. J1448−0110	SB 61	14:48:05.38, −01:10:57.72	0.02741	4.08	8.13 ± 0.01 | T_e[O III]	150 ± 20	8.0 ± 0.1	0.148 ± 0.005
42. J1521+0759		15:21:41.52, +07:59:21.77	0.09426	3.52	8.31 ± 0.14 | T_e[N II]	90 ± 30	1.5 ± 0.1	0.153 ± 0.008
43. J1525+0757		15:25:21.84, +07:57:20.30	0.07579	3.52	8.33 ± 0.04 | T_e[O II]	210 ± 20	0.5 ± 0.1	0.246 ± 0.008
44. J1545+0858	1725-54266-068	15:45:43.44, +08:58:01.34	0.03772	4.37	7.75 ± 0.03 | T_e[O III]	130 ± 20	8.6 ± 0.3	0.110 ± 0.036
45. J1612+0817		16:12:45.52, +08:17:01.01	0.14914	2.70	8.18 ± 0.19 | T_e[N II]	340 ± 60	0.7 ± 0.1	0.290 ± 0.008

Note. The CLASSY sample is composed of UV bright, nearby galaxies covering a range of metallicity, mass, SFR, and gas density. Columns (1)−(4) give the target name used in this work, alternative names used, coordinate R.A. and decl., and redshift. Column (5) gives the continuum flux at 1500 Å in units of 10^{-15} erg s^{-1} cm^{-2} $Å^{-1}$, from the CLASSY coadded spectra. Columns (6)–(9) list additional nebular properties derived from the optical spectra, namely the direct T_e-method oxygen abundance (12+log(O/H)) and the ion temperature used, the [S II] electron density, [O III] λ5007/[O II] λ3727 flux ratio, and the $E(B-V)$ reddening value determined from the Balmer decrement.

(This table is available in machine-readable form.)

Table 6
CLASSY Galaxy Photometry-derived Properties

Target	R.A., Decl. (J2000)	z	L_D (Mpc)	r_{50} ($''$)	Aper. log $M_\star$ ($M_\odot$)	Tot. log $M_\star$ ($M_\odot$)	Aper. log SFR ($M_\odot$ yr^{-1})	Tot. log SFR ($M_\odot$ yr^{-1})
1. J0021+0052	00:21:01.03, +00:52:48.08	0.09839	452	0.78	$8.88\pm^{0.23}_{0.36}$	$9.09\pm^{0.18}_{0.38}$	$0.99\pm^{0.21}_{0.14}$	$1.07\pm^{0.14}_{0.11}$
2. J0036-3333	00:36:52.68, -33:33:17.24	0.02060	89	2.85	$8.77\pm^{0.25}_{0.30}$	$9.14\pm^{0.26}_{0.23}$	$0.10\pm^{0.28}_{0.27}$	$1.01\pm^{0.19}_{0.21}$
3. J0127-0619	01:27:35.51, -06:19:36.06	0.00540	23	2.37	$7.38\pm^{0.23}_{0.30}$	$8.74\pm^{0.18}_{0.15}$	$-1.06\pm^{0.27}_{0.33}$	$-0.75\pm^{0.15}_{0.13}$
4. J0144+0453	01:44:41.36, +04:53:25.32	0.00520	23	2.85	$5.61\pm^{0.32}_{0.35}$	$7.65\pm^{0.24}_{0.29}$	$-1.86\pm^{0.11}_{0.09}$	$-0.81\pm^{0.29}_{0.46}$
5. J0337-0502	03:37:44.06, -05:02:40.19	0.01352	58	1.43	$6.89\pm^{0.29}_{0.34}$	$7.06\pm^{0.24}_{0.21}$	$-0.57\pm^{0.15}_{0.13}$	$-0.32\pm^{0.07}_{0.11}$
6. J0405-3648	04:05:20.46, -36:48:59.14	0.00280	11	3.56	$5.34\pm^{0.27}_{0.33}$	$6.61\pm^{0.28}_{0.28}$	$-2.96\pm^{0.28}_{0.22}$	$-1.81\pm^{0.31}_{0.27}$
7. J0808+3948	08:08:44.28, +39:48:52.51	0.09123	417	1.11	$8.85\pm^{0.32}_{0.23}$	$9.12\pm^{0.30}_{0.17}$	$0.94\pm^{0.20}_{0.22}$	$1.26\pm^{0.18}_{0.25}$
8. J0823+2806	08:23:54.96, +28:06:21.60	0.04722	209	2.12	$8.47\pm^{0.28}_{0.27}$	$9.38\pm^{0.33}_{0.19}$	$0.57\pm^{0.26}_{0.23}$	$1.48\pm^{0.15}_{0.32}$
9. J0926+4427	09:26:00.44, +44:27:36.54	0.18067	875	0.89	$8.75\pm^{0.31}_{0.28}$	$8.76\pm^{0.30}_{0.26}$	$0.97\pm^{0.18}_{0.15}$	$1.03\pm^{0.13}_{0.13}$
10. J0934+5514	09:34:20.02, +55:14:28.10	0.00250	12	2.61	$5.48\pm^{0.37}_{0.39}$	$6.27\pm^{0.15}_{0.20}$	$-2.09\pm^{0.11}_{0.08}$	$-1.52\pm^{0.09}_{0.07}$
11. J0938+5428	09:38:13.49, +54:28:25.09	0.10210	470	1.10	$8.98\pm^{0.23}_{0.46}$	$9.15\pm^{0.18}_{0.29}$	$1.07\pm^{0.25}_{0.26}$	$1.05\pm^{0.20}_{0.17}$
12. J0940+2935	09:40:12.87, +29:35:30.21	0.00168	8	5.15	$5.05\pm^{0.36}_{0.21}$	$6.71\pm^{0.23}_{0.40}$	$-3.05\pm^{0.19}_{0.12}$	$-2.01\pm^{0.42}_{0.37}$
13. J0942+3547	09:42:52.78, +35:47:25.98	0.01486	65	1.33	$6.75\pm^{0.43}_{0.40}$	$7.56\pm^{0.21}_{0.29}$	$-0.90\pm^{0.14}_{0.11}$	$-0.76\pm^{0.19}_{0.12}$
14. J0944-0038	09:44:01.87, -00:38:32.18	0.00478	21	0.98	$5.58\pm^{0.38}_{0.21}$	$6.83\pm^{0.44}_{0.25}$	$-1.49\pm^{0.21}_{0.15}$	$-0.78\pm^{0.19}_{0.16}$
15. J0944+3442	09:44:25.87, +34:42:08.49	0.02005	87	2.46	$7.62\pm^{0.31}_{0.28}$	$8.19\pm^{0.40}_{0.23}$	$-0.83\pm^{0.27}_{0.43}$	$-0.01\pm^{0.28}_{0.65}$
16. J1016+3754	10:16:24.48, +37:54:46.08	0.00388	18	1.84	$5.98\pm^{0.28}_{0.36}$	$6.72\pm^{0.27}_{0.22}$	$-1.62\pm^{0.13}_{0.10}$	$-1.17\pm^{0.18}_{0.18}$
17. J1024+0524	10:24:29.25, +05:24:51.02	0.03319	145	1.33	$7.51\pm^{0.37}_{0.28}$	$7.89\pm^{0.37}_{0.24}$	$-0.01\pm^{0.19}_{0.12}$	$0.21\pm^{0.14}_{0.12}$
18. J1025+3622	10:25:48.38, +36:22:58.42	0.12650	592	0.84	$8.81\pm^{0.27}_{0.25}$	$8.87\pm^{0.25}_{0.27}$	$0.80\pm^{0.21}_{0.16}$	$1.04\pm^{0.14}_{0.18}$
19. J1044+0353	10:44:57.79, +03:53:13.10	0.01287	55	1.20	$6.13\pm^{0.23}_{0.09}$	$6.80\pm^{0.41}_{0.26}$	$-0.90\pm^{0.07}_{0.11}$	$-0.59\pm^{0.11}_{0.14}$
20. J1105+4444	11:05:08.16, +44:44:47.40	0.02154	93	2.65	$7.76\pm^{0.35}_{0.25}$	$8.98\pm^{0.29}_{0.24}$	$-0.05\pm^{0.22}_{0.17}$	$0.69\pm^{0.28}_{0.22}$
21. J1112+5503	11:12:44.05, +55:03:47.01	0.13164	618	0.92	$9.55\pm^{0.26}_{0.28}$	$9.59\pm^{0.33}_{0.19}$	$1.39\pm^{0.22}_{0.30}$	$1.60\pm^{0.20}_{0.25}$
22. J1119+5130	11:19:34.36, +51:30:12.02	0.00446	20	1.87	$6.24\pm^{0.25}_{0.28}$	$6.77\pm^{0.15}_{0.28}$	$-2.02\pm^{0.26}_{0.17}$	$-1.58\pm^{0.21}_{0.12}$
23. J1129+2034	11:29:14.15, +20:34:52.01	0.00470	21	3.10	$5.75\pm^{0.36}_{0.40}$	$8.09\pm^{0.37}_{0.27}$	$-1.74\pm^{0.15}_{0.12}$	$-0.37\pm^{0.38}_{0.56}$
24. J1132+5722	11:32:02.64, +57:22:36.39	0.00504	23	7.29	$6.02\pm^{0.18}_{0.35}$	$7.31\pm^{0.23}_{0.26}$	$-2.31\pm^{0.28}_{0.19}$	$-1.07\pm^{0.27}_{0.35}$
25. J1132+1411	11:32:35.35, +14:11:29.83	0.01764	76	2.25	$6.79\pm^{0.41}_{0.28}$	$8.68\pm^{0.28}_{0.19}$	$-0.58\pm^{0.13}_{0.10}$	$0.44\pm^{0.24}_{0.27}$
26. J1144+4012	11:44:22.28, +40:12:21.19	0.12695	594	1.16	$9.41\pm^{0.29}_{0.22}$	$9.89\pm^{0.18}_{0.29}$	$1.09\pm^{0.29}_{0.41}$	$1.51\pm^{0.20}_{0.29}$
27. J1148+2546	11:48:27.34, +25:46:11.77	0.04512	199	0.87	$7.39\pm^{0.46}_{0.23}$	$8.14\pm^{0.34}_{0.24}$	$0.29\pm^{0.18}_{0.15}$	$0.53\pm^{0.17}_{0.14}$
28. J1150+1501	11:50:02.73, +15:01:23.48	0.00245	11	1.76	$5.69\pm^{0.38}_{0.30}$	$6.84\pm^{0.28}_{0.30}$	$-1.70\pm^{0.11}_{0.09}$	$-1.33\pm^{0.29}_{0.23}$
29. J1157+3220	11:57:31.68, +32:20:30.12	0.01097	48	2.89	$7.33\pm^{0.41}_{0.31}$	$9.04\pm^{0.32}_{0.18}$	$-0.47\pm^{0.19}_{0.13}$	$0.97\pm^{0.21}_{0.42}$
30. J1200+1343	12:00:33.42, +13:43:07.95	0.06675	300	0.98	$7.46\pm^{0.59}_{0.21}$	$8.12\pm^{0.47}_{0.42}$	$0.38\pm^{0.21}_{0.15}$	$0.75\pm^{0.20}_{0.16}$
31. J1225+6109	12:25:05.41, +61:09:11.30	0.00234	11	2.60	$5.79\pm^{0.35}_{0.28}$	$7.12\pm^{0.34}_{0.24}$	$-1.81\pm^{0.15}_{0.13}$	$-1.08\pm^{0.26}_{0.26}$
32. J1253-0312	12:53:05.96, -03:12:58.84	0.02272	99	1.08	$7.46\pm^{0.33}_{0.25}$	$7.65\pm^{0.51}_{0.23}$	$0.37\pm^{0.15}_{0.18}$	$0.56\pm^{0.15}_{0.15}$
33. J1314+3452	13:14:47.37, +34:52:59.81	0.00288	13	1.77	$5.28\pm^{0.25}_{0.17}$	$7.56\pm^{0.30}_{0.21}$	$-1.78\pm^{0.14}_{0.14}$	$-0.67\pm^{0.23}_{0.55}$
34. J1323-0132	13:23:47.52, -01:32:51.94	0.02246	97	0.70	$6.22\pm^{0.12}_{0.09}$	$6.31\pm^{0.26}_{0.10}$	$-0.78\pm^{0.10}_{0.09}$	$-0.72\pm^{0.08}_{0.09}$
35. J1359+5726	13:59:50.88, +57:26:22.92	0.03383	148	1.40	$8.11\pm^{0.36}_{0.30}$	$8.41\pm^{0.31}_{0.26}$	$0.20\pm^{0.25}_{0.18}$	$0.42\pm^{0.20}_{0.14}$
36. J1416+1223	14:16:12.87, +12:23:40.42	0.12316	575	0.99	$9.46\pm^{0.23}_{0.30}$	$9.59\pm^{0.32}_{0.26}$	$1.23\pm^{0.24}_{0.26}$	$1.57\pm^{0.21}_{0.25}$
37. J1418+2102	14:18:51.12, +21:02:39.84	0.00855	37	1.13	$5.71\pm^{0.48}_{0.21}$	$6.22\pm^{0.49}_{0.35}$	$-1.38\pm^{0.13}_{0.15}$	$-1.13\pm^{0.15}_{0.16}$
38. J1428+1653	14:28:56.41, +16:53:39.32	0.18167	880	0.93	$9.50\pm^{0.19}_{0.30}$	$9.56\pm^{0.15}_{0.23}$	$1.14\pm^{0.27}_{0.23}$	$1.22\pm^{0.26}_{0.19}$
39. J1429+0643	14:29:47.00, +06:43:34.95	0.17350	836	0.86	$8.46\pm^{0.37}_{0.21}$	$8.80\pm^{0.35}_{0.21}$	$1.29\pm^{0.11}_{0.12}$	$1.42\pm^{0.11}_{0.17}$
40. J1444+4237	14:44:11.46, +42:37:35.57	0.00230	11	2.76	$4.91\pm^{0.33}_{0.23}$	$6.48\pm^{0.17}_{0.17}$	$-2.41\pm^{0.11}_{0.11}$	$-1.94\pm^{0.11}_{0.08}$
41. J1448-0110	14:48:05.38, -01:10:57.72	0.02741	119	1.07	$7.29\pm^{0.54}_{0.30}$	$7.61\pm^{0.41}_{0.24}$	$0.06\pm^{0.20}_{0.13}$	$0.39\pm^{0.13}_{0.14}$
42. J1521+0759	15:21:41.52, +07:59:21.77	0.09426	432	0.98	$8.90\pm^{0.35}_{0.26}$	$9.00\pm^{0.29}_{0.30}$	$0.85\pm^{0.21}_{0.21}$	$0.95\pm^{0.16}_{0.17}$
43. J1525+0757	15:25:21.84, +07:57:20.30	0.07579	343	1.32	$9.13\pm^{0.31}_{0.24}$	$10.06\pm^{0.28}_{0.42}$	$0.87\pm^{0.28}_{0.34}$	$1.00\pm^{0.69}_{0.24}$
44. J1545+0858	15:45:43.44, +08:58:01.34	0.03772	166	1.08	$7.39\pm^{0.24}_{0.20}$	$7.52\pm^{0.43}_{0.26}$	$0.32\pm^{0.19}_{0.18}$	$0.37\pm^{0.13}_{0.17}$
45. J1612+0817	16:12:45.52, +08:17:01.01	0.14914	708	0.88	$9.74\pm^{0.18}_{0.26}$	$9.78\pm^{0.28}_{0.26}$	$1.43\pm^{0.27}_{0.28}$	$1.58\pm^{0.28}_{0.24}$

Note. CLASSY sample properties derived from UV+optical photometry, as described in Section 4.6. Columns (1)−(3) give the target name used in this work, coordinate R.A. and decl., and redshift. Column (4) lists the luminosity distance, corrected for the Hubble flow using the velocity field model of Masters (2005). Column (5) gives the half-light radii in arcseconds, as derived from the optical imaging (see Figure 2). Columns (6) and (7) list the stellar masses derived using `Beagle` SED fitting for both the light within the COS aperture and the entire galaxy, respectively, of a given target. Similarly, columns (8) and (9) provide the SED-derived SFRs.

(This table is available in machine-readable form.)

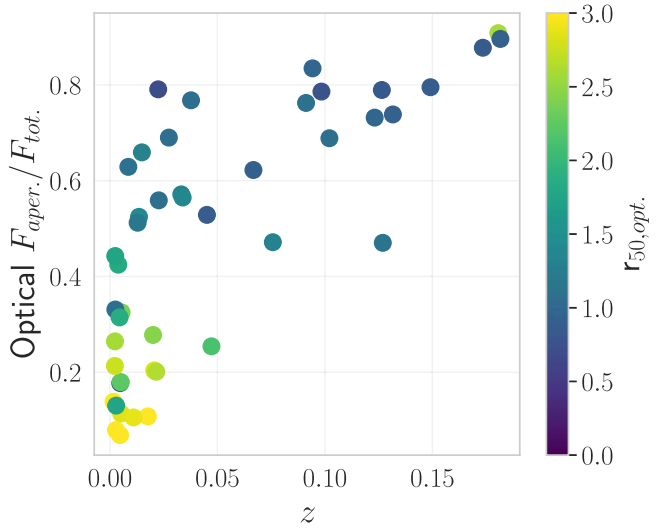

Figure 10. Aperture fraction of optical flux vs. redshift for the CLASSY sample. The points are color coded by the optical half-light radii in arcseconds.

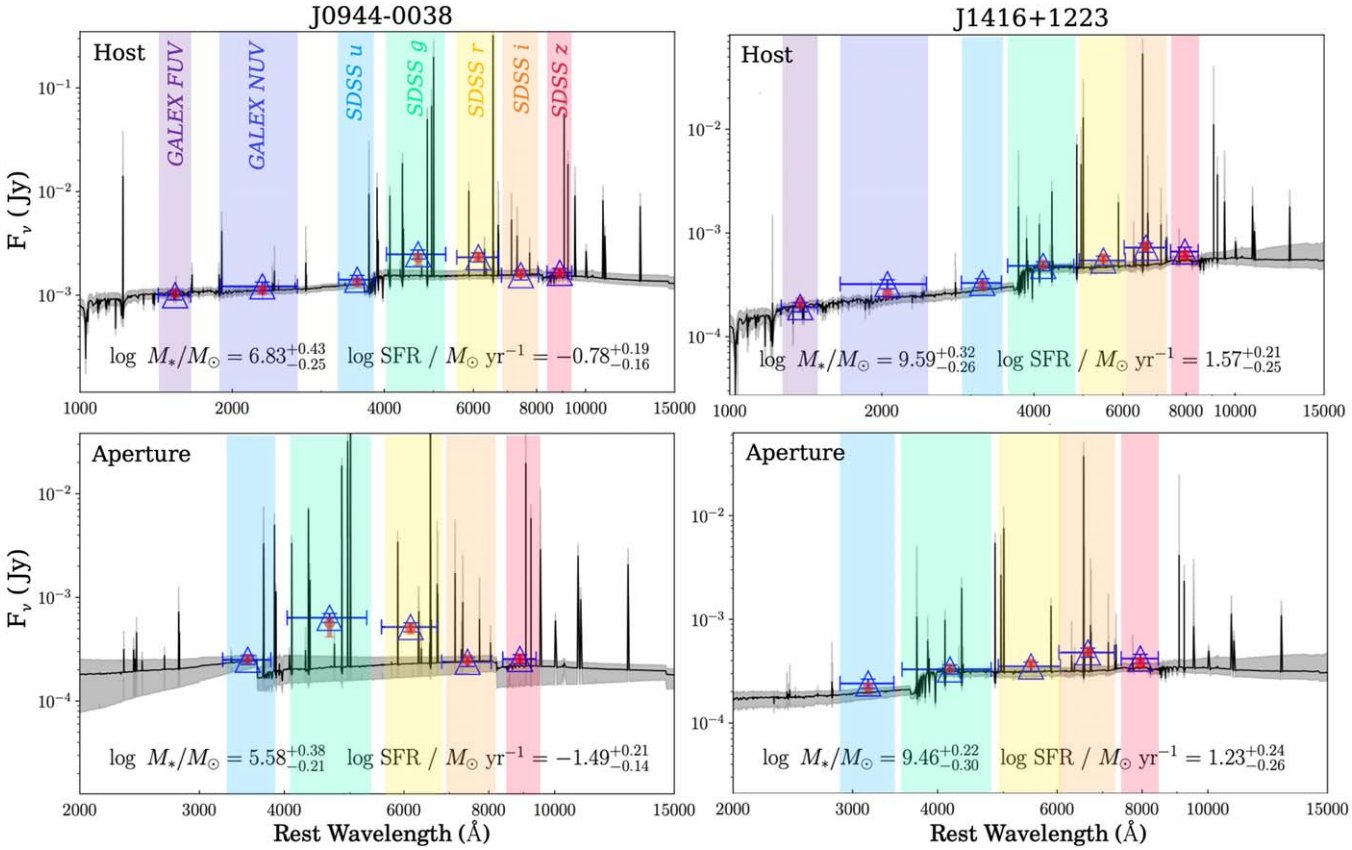

Figure 11. Example SED fits for two of the CLASSY galaxies, one local dwarf galaxy (J0944-0038, left) and one emission-line galaxy at $z \approx 0.1$ (J1416+1223, right). The fits to host galaxies are shown in the top row while the aperture fits are in the bottom. Blue triangles are the measured fluxes from broadband photometry, and red circles give BEAGLE predictions. The median BEAGLE SED and 16th and 84th percentiles of posterior distribution are shown in black line and gray-shaded area, respectively. The significant excess to the broadband flux in the *gr* bands of J0944-0038 and *r* band of J1416+1223 is due to strong nebular emission lines, which are accounted for by BEAGLE.

Appendix C
SED Fitting

Here we further describe the SED fitting method used to determine the stellar masses and SFRs presented in Section 4.7. SED fitting was performed using the Bayesian Analysis of Galaxy SEDs (BEAGLE, v0.24.0; Chevallard & Charlot 2016). BEAGLE is a new-generation SED tool that incorporates several novel approaches over past codes. First, the modular design of BEAGLE allows a physically consistent combination of different prescriptions for the production of

starlight in galaxies and its transfer through the ISM (absorption and emission by gas, attenuation by dust) and the IGM (absorption by gas). Second, BEAGLE uses a flexible parameterization of several prescriptions to describe the star formation and chemical enrichment histories of galaxies, ranging from simple analytic functions to the predictions of sophisticated galaxy formation models, to interpret the combinations of photometric and spectroscopic observation of galaxies. As a result, BEAGLE fits can provide a physically consistent description of the contributions by stars, gas, and dust to the integrated emission from a galaxy. Note that this updated SED fitting approach is particularly important for the subset of CLASSY galaxies with very strong nebular continuum and line emission as BEAGLE self-consistently accounts for these contributions in the synthetic model spectrum. Using BEAGLE, two sets of stellar mass and SFR parameters were computed: (1) an aperture set that provides insights for the star-forming regions specifically targeted within the COS 2.″5 aperture and (2) a host galaxy set that better characterizes the properties of the entire galaxies.

C.1. Choice of Photometry

The SDSS provides optical imaging in *ugriz* for 42 galaxies in the CLASSY sample. For the other three, J0036-3333 and J0405-3648 have *grizY* images from the DES (Abbott et al. 2021), and J0337-0502 is observed by the Pan-STARRS1 (Chambers et al. 2016). For the UV, 43 galaxies (all but J0337-0502 and J1157+3220) have imaging in the NUV and FUV available from GALEX (Martin et al. 2005). Additionally, Wide-field Infrared Survey Explorer (WISE) W1 and W2 near-infrared (NIR) data are also available for the entire CLASSY sample. However, WISE photometry introduces large model uncertainties due to the contribution of post-main-sequence stars to NIR light (e.g., Salim et al. 2016) and does not significantly affect the CLASSY stellar mass ($\Delta_{\log M_\star} < 0.31$ dex) and SFR ($\Delta_{\log \mathrm{SFR}} < 0.21$ dex) measurements, and so it was not included in the CLASSY SED fitting.

C.2. New Flux Measurements

Due to the irregular morphologies and range of redshifts of the CLASSY sample, the SDSS catalog photometry can have large uncertainties when a simple, symmetric model is assumed or only a portion (e.g., a single H II region) of a host galaxy is measured. We, therefore, remeasured the GALEX and SDSS fluxes.

For the aperture stellar mass and SFR determinations, *ugriz* or *grizY* photometry was measured for targeted star-forming regions in a 3″ aperture, well matched to the size of COS aperture convolved with typical SDSS seeing (see, e.g., Senchyna et al. 2019). The sky background was estimated in a 1″ wide circular annulus located at 1′ using the median flux values after σ-clipping (low 10σ, high 3σ). Corrections for Galactic foreground extinction were then applied, assuming an $R_V = 3.1$ and Milky Way extinction curve Cardelli et al. (1989). The GALEX UV imaging was not used for these aperture calculations due to its relatively poor resolution (4.″5–6.″0 FWHM).

For the total stellar mass and SFR determinations of each galaxy, the total fluxes in the UV and optical were measured, but with a more sophisticated method to account for the irregular morphologies and potential contamination from nearby objects. First, segmentation maps were produced for each galaxy using the Photutils package (Bradley et al. 2021). For the optical imaging, *g*-band segmentation was computed, which includes strong optical emission lines such as [O III] and (or) Hβ for the majority of the CLASSY sample. This maximizes the ability to probe the often faint and extended nebular emission, which are incorporated into the BEAGLE models. To produce the *g*-band segmentation maps, a minimum of eight connected pixels at 2σ above the background after the image is smoothed by a 2D Gaussian kernel (FWHM = 10 pix) is required. Similarly, NUV segmentation was computed for the UV photometry, but using a Gaussian kernel with FWHM = 3 pix. Each map was visually inspected to ensure an adequate segmentation that captures the total galaxy light in both the optical and UV. If a map failed the visual inspection, the segmentation parameters were adjusted, and source deblending was implemented in Photutils to exclude contamination. Second, the *g*-band and NUV segmentations were used to measure the optical photometry in *ugriz* (or *grizY*) and NUV and FUV photometry, respectively. In a similar manner as the aperture determinations, background subtraction and Galactic extinction corrections were applied. In general, we found that the 3″ aperture flux accounts for ∼25% of the total g-band flux at $z \sim 0.01$, and ∼80% at $z \sim 0.17$.

Finally, the galaxy distances and absolute magnitudes were determined. Since nearly half of the sample (20/45) are very nearby galaxies with optical spectroscopic redshifts of $z < 0.02$, they may have peculiar motions that will bias the luminosity distances derived from redshifts. To uniformly estimate their distances, the heliocentric redshifts were first converted to the cosmic microwave background (CMB) frame using the CMB dipole measured by Lineweaver et al. (1996). The local velocity field modeled by Masters (2005) was then adopted to compute the flow-corrected luminosity distances, with the amount of correction ranging from < 1% to 20% (median 6%).

C.3. SED Model Assumptions

With the redshifts, corrected luminosity distances, and photometry for both the targeted regions and entire galaxies in hand, the $M_\star$ and SFRs can be self-consistently constrained with the BEAGLE code. Briefly, the Gutkin et al. (2016) model was adopted, which self-consistently incorporates the stellar emission from the latest version of the Bruzual & Charlot (2003) SPS results and the nebular emission output by the photoionization code Cloudy (Ferland et al. 2013). We assumed a Chabrier (2003) Galactic disk IMF (mass range 0.1–100 $M_\odot$), the two-component attenuation model from Charlot & Fall (2000), and a constant SFH. Free parameters are thus the stellar mass, age, metallicity, gas ionization parameter, log *U*, and effective attenuation $\hat{\tau}_V$. The interstellar (dust+gas-phase) metallicity was matched to the stellar metallicity of the constant star formation. Of the three choices of dust-to-metal mass ratio provided by BEAGLE ($\xi_d = 0.1, 0.3, 0.5$), we assume $\xi_d = 0.3$ as the value closest to the solar value ($\xi_d = 0.36$ Gutkin et al. 2016).

The BEAGLE SED fits for two CLASSY galaxies, local dwarf galaxy J0944-0383 and $z \sim 0.1$ emission-line galaxy J1416+1223, are shown in Figure 11. For comparison, the fit to the host galaxy UV+optical photometry is shown in the top panels relative to the aperture optical photometry fit in the bottom panels. Contamination to the broadband flux from strong emission lines is clearly seen in the *gr* bands for local

systems (e.g., J0944-0038) or r band for those at slightly high redshift (e.g., J1416+1223). These models demonstrate the importance of properly accounting for strong nebular emission in our SED fitting with a self-consistent program like BEAGLE.

From the output posterior distribution, the $M_\star$ and SFRs were computed for both the targeted aperture regions and the entire galaxies. The resulting stellar masses and SFRs are reported in Table 6 in Appendix B for both the aperture and total host galaxy sets.

C.4. Choice of Star Formation History

It is very difficult to recover accurate values of the SFRs through SED fitting for realistic galaxies, in large part due to their unconstrained SFHs. Fortunately, the previous SED fits using a constant SFH were shown to perform well for a subset of the CLASSY sample (Senchyna et al. 2017, 2019), and allowed for a consistent comparison with the SED fitting conducted for high-redshift galaxies. Following this method, we have assumed a constant SFH, which benefits from having the least free parameters, yet it provides satisfying fits to the broadband photometry even when strong emission lines are present. However, an important caveat is the potentially hidden old stellar populations in the CLASSY galaxies, especially outside the burst of star formation targeted by the COS aperture. Our assumption of a simple constant SFH thus inevitably introduces additional systematic uncertainties to our estimates, often leading to a lower stellar mass compared to other more complicated SFHs.

C.5. Exploration of SED Systematics

To better understand the accuracy and precision of our SED-derived galaxy properties and to provide consistency checks, we performed the following tests:

1. Impact of assumed SFH. We investigated the impact of assuming just a simple constant SFH by comparing to more complicated models. First, we allowed composite SFHs consisting of a constant SFH plus a single burst in the fit in order to allow the maximum flexibility for BEAGLE to properly account for any possible old stellar populations. In most cases, BEAGLE favored either a dominant constant SFH component or a dominant SSP component. The resulting fitted masses are larger relative to the values assuming a constant SFH by $0.01^{+0.05}_{-0.04}$ dex. Second, since a red component from an older stellar population would primarily arise from stars outside the aperture, we also tested fitting the flux inside and outside the aperture separately using two populations of constant star formation, one inside and one outside the aperture. Using the four sources in our sample showing the most extreme extended components outside, we found the differences in both stellar masses and SFRs to be $\lesssim 1\sigma$ and within the uncertainties. However, Lower et al. (2020) recently investigated the impact of SFH on SED fitting and found that assuming a constant SFH can underestimate the stellar mass by 0.48 ± 0.61 dex. Unfortunately, other simple parametric models such as a delayed-τ SFH[49] also performed poorly in this work; only complicated, nonparametric SFHs produce realistic values. Thus, for simplicity and for consistent comparison with high-redshift galaxies, a simple constant SFH was adopted for the CLASSY SED fitting, resulting in relatively large uncertainties.

2. Comparisons to other catalogs. We compared the stellar masses and SFRs to the values from the MPA-JHU catalog.[50] On average, the CLASSY stellar masses are smaller by -0.28 dex, while the 16th and 84th percentile differences from the MPA-JHU values are -0.60 and 0.40 dex, respectively. For the SFRs, the CLASSY values are larger on average by 0.18 dex, while the 16th and 84th percentile differences from the MPA-JHU values are -0.09 and 0.63 dex, respectively. While we find generally good agreement with the MPA-JHU values, there are some significant outliers due to many differing assumptions in the photometry and SED modeling. However, dust extinction is unlikely to be the cause given the strong agreement between the CLASSY aperture (host) values of effective optical depth ($\tau_{V,\rm eff}$) and those derived from optical spectra ($\Delta\tau_{V,\rm eff} = -0.06^{+0.14}_{-0.10}$ ($0.09^{+0.53}_{-0.22}$)).

We also compared to the GALEX-SDSS-WISE Legacy Catalog (GSWLC) of Salim et al. (2016). The GSWLC contains SDSS galaxies more distant on average than the CLASSY sample at $0.01 < z < 0.30$ and $r_{\rm petro} < 18$. These distances ensure that the SDSS photometry is safe to use for SED fitting. A cross-match between the CLASSY sample and GSWLC yields 22 matches, of which 12 have GSWLC SED fits with $\chi_{\rm reduced} > 30$. For the remaining 10 galaxies, 4 have GSWLC SED fits with $\chi_{\rm reduced} > 10$. The large fraction of poor fits in GSWLC are likely due to its inability to account for large broadband excess caused by strong nebular emission lines. For the 6 galaxies with GSWLC $\chi_{\rm reduced} < 10$, we find differences (Δ=CLASSY values $-$ GSWLC values) of $\Delta M_{\star,\rm host} = -0.27^{+0.33}_{-0.39}$ dex and $\Delta SFR_{\rm host} = 0.12^{+0.13}_{-0.11}$ dex. On average, the CLASSY SFRs are larger by $\sim$0.1 dex compared to GSWLC1 SED SFRs, but smaller by $\sim$0.2 dex compared to GSWLC1 WISE SFRs. Extreme outliers and the sources of such discrepancies will be explored in a future paper.

3. Comparison to Hα SFRs. We calculated SFRs in another way, using the reddening-corrected Hα flux measured from the optical spectra, the luminosity distances listed in Table 6, and the SFR calibration from Kennicutt & Evans (2012). For galaxies with optical spectra from the SDSS, we use the Hα flux values from the MPA-JHU catalog, where each spectrum has been tied back to the SDSS r-band fibermag. Note that this Hα SFR calibration assumes a Kroupa & Weidner (2003) IMF, which is consistent with the Chabrier (2003) IMF used for the SED fitting (e.g., Chomiuk & Povich 2011). In comparison to the SED-derived SFRs, we find the Hα SFRs to be larger on average, with a typical percent difference of 8%, and a few strong outliers extending from -202% to $+48\%$.

4. Comparison to nebular properties. Finally, we compared the 12+log(O/H) and log$U$ values from the BEAGLE SED fits to those derived from the optical spectra (see Sections 4.5 and 4.6). Of our three comparisons (other catalogs, SFRs, and nebular properties), the latter shows the largest discrepancies, where the SED metallicities (ionization parameters) are systematically lower (higher) than the measured values, with

[49] The common τ-model, parameterized by $\dot{M}_\star \propto e^{-t/\tau}$, has an exponentially declining SFH with some characteristic e-folding time, τ. The delayed-τ model, parameterized by $\dot{M}_\star \propto t \cdot e^{-t/\tau}$, is an expansion of the τ-model such that it allows for linear growth at early times in addition to exponential decline at later times.

[50] Data catalogs are available at http://www.mpa-garching.mpg.de/SDSS/. The Max Plank Institute for Astrophysics/The Johns Hopkins University (MPA/JHU) SDSS database was produced by a collaboration of researchers (currently or formerly) from the MPA and the JHU. The team is made up of Stephane Charlot (IAP), Guinevere Kauffmann and Simon White (MPA), Tim Heckman (JHU), Christy Tremonti (U. Wisconsin-Madison, formerly JHU), and Jarle Brinchmann (Universidade do Porto, formerly MPA).

median differences of 0.37 dex (−0.36 dex). However, the BEAGLE values have large uncertainties (>0.5 dex) by design that give it the flexibility necessary to test large parameter space and thus are still generally consistent with the measured CLASSY values. Note that the choice to not fix metallicity, ionization parameter, or dust extinction to spectroscopic values was deliberate in order to not introduce other systematic biases (i.e., the burst of star formation within the spectroscopic aperture may have different ISM conditions than the outer regions of a galaxy).

Appendix D
Notes on Individual Galaxies

For transparency and to improve the usability of the CLASSY HLSPs, we mention here any unique notes for individual galaxies.

J0036-3333. J0036-3333 is also commonly known as the galaxy Haro 11, which contains multiple stellar populations. The CLASSY coadded spectrum only focuses on knot C (Vader et al. 1993). Knot C is the most UV luminous source and main contributor to the Lyα emission from Haro 11 (Hayes et al. 2007).

J0127-0619. The common name of J0127-0619 is Mrk 996. This galaxy is known to have complex emission line kinematics, a large Wolf–Rayet population, and a high electron density within its inner core region (James et al. 2009; Telles et al. 2014).

J0144+0453. J0144+0453 is more commonly known as UM133 and has an extended tail to the N.

J0337-0502. J0337-0502 is part of the well-known, metal-poor galaxy SBS 0335-052 that has two main star-forming clusters, E and W. The CLASSY coadded spectrum only contains light from the E region. It also combines data from the COS FUV detector lifetime positions 3 and 4. SBS 0335-052E consists of six young (10 < Myr) star clusters (Adamo et al. 2010), four of which fall within the COS aperture (Wofford et al. 2021).

J0405-3648. J0405-3648 is fairly extended, with many small ionized clumps seen in the optical imaging. The CLASSY coadded spectrum combines data taken at position angles that are offset by 50°.

J0808+3948. The CLASSY coadded spectrum combines data taken at position angles that are offset by 84°.

J0823+2806. J0823+2806 is part of the Lyman Alpha Reference Sample (LARS; Hayes et al. 2014; Östlin et al. 2014) and is identified as LARS9. The CLASSY coadded spectrum combines data taken at position angles that are offset by 34°. The COS aperture is dominated by emission from a single massive star cluster.

J0926+4427. J0926+4427 is part of the LARS and is identified as LARS14. LARS14 is classified as a Lyman break analog (Heckman et al. 2011), and also a Green Pea galaxy (Henry et al. 2015). The CLASSY coadded spectrum combines data taken at position angles that are offset by 82°.

J0934+5514. This is the famous low-metallicity dwarf galaxy, I Zw 18. I Zw 18 has two main components that have been heavily studied: the NW and SE components. The CLASSY coadded spectrum only contains light from the NW region. It also combines data from COS FUV detector lifetime positions 1 and 4 and data taken at position angles that are offset by 67°.

J0938+5428. J0938+5248, also known as SBS 0934+546, is part of the LARS (Hayes et al. 2014; Östlin et al. 2014) and is identified as LARS12. The CLASSY coadded spectrum combines data taken at position angles that are offset by 88°.

J0940+2935. J0940+2935 has extended optical emission. The CLASSY coadded spectrum combines data taken at position angles that are offset by 18°.

J0942+3547. This galaxy is also known as CG-274 and SB 110 in Senchyna et al. (2017). The CLASSY coadded spectrum combines data from COS FUV detector lifetime positions 3 and 4. The CLASSY coadded spectrum combines data taken at position angles that are offset by 29°.

J0944-0038. J0944-0038, more commonly known as CGCG 007-025, is part of LMLVL (Berg et al. 2012). It is also known as SB2 in Senchyna et al. (2017). The CLASSY coadded spectrum combines data from COS FUV detector lifetime positions 3 and 4. The CLASSY coadded spectrum combines data taken at position angles that are offset by 68°.

J0944+3424. J0944+3424 has extended optical emission. The CLASSY coadded spectrum combines data taken at position angles that are offset by 76°.

J1016+3754. The CLASSY coadded spectrum combines data from COS FUV detector lifetime positions 3 and 4 and combines data taken at position angles that are offset by 84°.

J1024+0524. This galaxy is also known as SB 36 in (Senchyna et al. 2017). The CLASSY coadded spectrum combines data from COS FUV detector lifetime positions 3 and 4.

J1025+3622. The CLASSY coadded spectrum combines data taken at position angles that are offset by 21°.

J1044+0353. The CLASSY coadded spectrum combines data taken at position angles that are offset by 23°. This galaxy is denoted as an extreme emission-line galaxy in Berg et al. (2021).

J1105+4444. J1105+445, more commonly known as Mrk 162, has extended optical emission. The CLASSY coadded spectrum combines data from COS FUV detector lifetime positions 3 and 4 and combines data taken at position angles that are offset by 46°.

J1112+5503. The COS G185M and G225M observations for J1112+5503 were executed with an error, but were not reacquired, so no MR extensions are available in the CLASSY coadds.

J1119+5130. J1119+5130, commonly known as Arp's Galaxy, has extended optical emission. The CLASSY coadded spectrum combines data taken at position angles that are offset by 88°.

J1129+2034. This galaxy is identified in the NASA/IPAC Extragalactic Database as IC 700, but is also known as SB 179 in (Senchyna et al. 2017), and is denoted as an extreme emission-line galaxy. The CLASSY coadded spectrum combines data from COS FUV detector lifetime positions 3 and 4. The CLASSY coadded spectrum combines data taken at position angles that are offset by 47°.

J1132+5722. J1132+5722, also known as SBSG1129+576, has extended optical emission. The CLASSY coadded spectrum combines data from COS FUV detector lifetime positions 3 and 4.

J1144+4012. The CLASSY coadded spectrum combines data taken at position angles that are offset by 28°.

J1148+2546. This galaxy is also known as SB 182 in Senchyna et al. (2017). The CLASSY coadded spectrum

combines data from COS FUV detector lifetime positions 3 and 4 and data taken at position angles that are offset by 27°.

J1150+1501. J1150+1501 is more commonly known as Mrk 750.

J1157+3220. J1157+3220 has extended optical emission. The CLASSY coadded spectrum combines data from COS FUV detector lifetime positions 3 and 4.

J1225+6109. J1225+6109, also known as SBS 1222+614, has extended optical emission. The CLASSY coadded spectrum combines data from COS FUV detector lifetime positions 3 and 4 and data taken at position angles that are offset by 76°.

J1253-0312. J1253-0312 is more commonly known as SHOC 391.

J1314+3452. This galaxy is also known as SB 153 in Senchyna et al. (2017) and is denoted as an extreme emission-line galaxy. The CLASSY coadded spectrum combines data taken at position angles that are offset by 54°.

J1323-0132. J1323-0132, also known as UM 570, has extended optical emission. The CLASSY coadded spectrum combines data from COS FUV detector lifetime positions 3 and 4.

J1359+5726. J1359+5726, also commonly known as Mrk 1486 and part of the LARS sample with ID Ly52, has extended optical emission. The CLASSY coadded spectrum combines data from COS FUV detector lifetime positions 1 and 3 and data taken at position angles that are offset by 82°.

J1418+2102. The CLASSY coadded spectrum combines data from COS FUV detector lifetime positions 3 and 4 and data taken at position angles that are offset by 26°. This galaxy is denoted as an extreme emission line galaxy in Berg et al. (2021).

J1444+4237. J1444+4237 is also known as HS1442+4250. The CLASSY coadded spectrum combines data from COS FUV detector lifetime positions 3 and 4 and data taken at position angles that are offset by 47°. Note that an additional data set, LDXT06010, was not used in the CLASSY coadd because there was a data quality note that the Take Data Flag was not on throughout the observation, so the COS light path was blocked during the exposure.

J1545+0858. The CLASSY coadded spectrum combines data from COS FUV detector lifetime positions 3 and 4 and data taken at position angles that are offset by 51°.

Appendix E
CLASSY Coadded Spectra

In Figure 12, we display one of the moderate- or low-resolution coadded spectra for each of the 45 galaxies in the CLASSY sample. The rest-frame, Galactic-extinction-corrected, binned, moderate-resolution spectrum is plotted in gray when available. For galaxies with archival G140L spectra, the low-resolution coadd is shown. In order to visually detect emission and absorption features more easily, the spectrum has also been convolved with a 1D Gaussian two-element kernel and overplotted in black. The most prominent absorption and emission features are labeled in the top panel of each spectrum, with nebular (dashed pink lines) and fine structure (solid pink lines) emission features marked above the spectra, while ISM (solid blue lines), stellar wind (dotted–dashed green lines), and photospheric (solid green lines) are marked below the spectra. Contamination from geocoronal and O I emission and Milky Way ISM absorption are whited-out. The bottom panel plots the S/N ratio as a function of wavelength, where each vertical shaded bar shows the average S/N within its wavelength

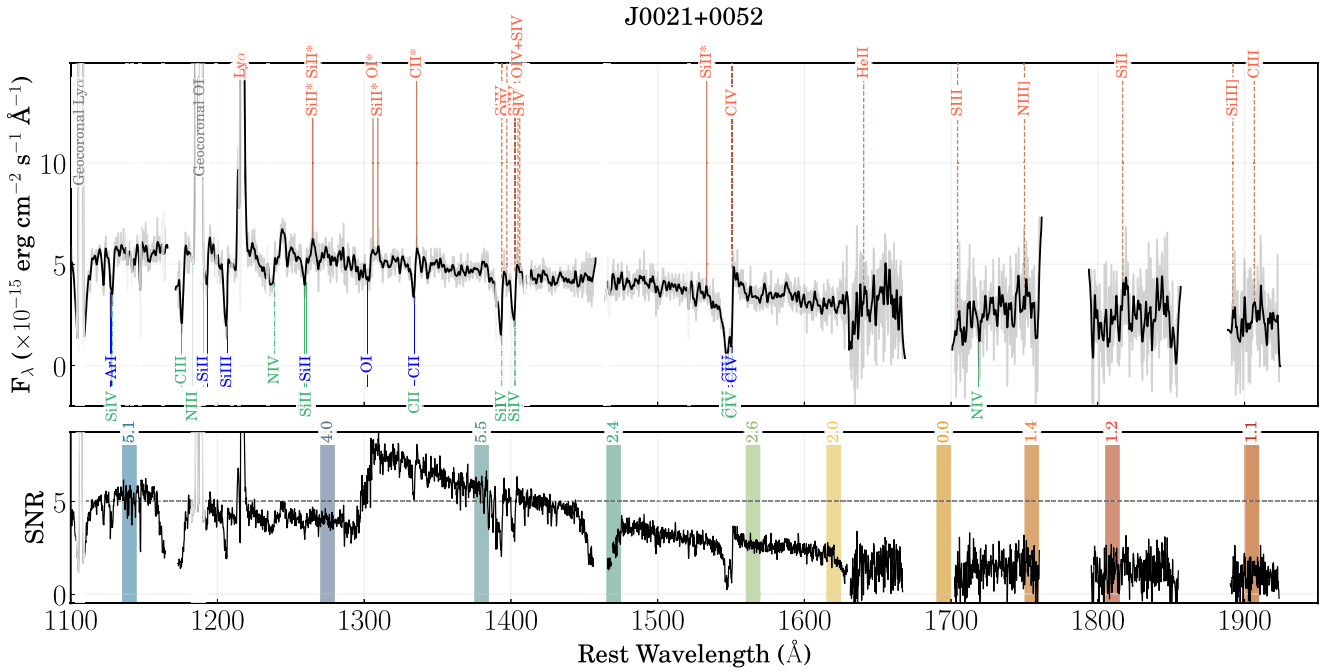

Figure 12. Moderate-resolution coadded spectrum of J0021+0052, highlighting the full FUV spectral range covered in the CLASSY atlas. The binned, Galactic-extinction-corrected, rest-frame spectrum is shown in gray, and the smoothed version that has been convolved with a 1D Gaussian two-element kernel is overplotted in black to make spectral features more apparent. Prominent absorption and emission features are labeled in the top panel. The bottom panel shows the S/N as a function of wavelength, where the colored vertical bands note the S/N value at their respective locations. Coadded spectra for all 45 galaxies in the CLASSY sample are provided in the figure set.

(The complete figure set (45 images) is available.)

coverage. Since the plotted spectrum is binned by the 6 pixels of a resolution element, these S/N values are per resel.

ORCID iDs

Danielle A. Berg https://orcid.org/0000-0002-4153-053X
Bethan L. James https://orcid.org/0000-0003-4372-2006
Teagan King https://orcid.org/0000-0003-0834-4150
Meaghan McDonald https://orcid.org/0000-0003-0557-3433
Zuyi Chen https://orcid.org/0000-0002-2178-5471
John Chisholm https://orcid.org/0000-0002-0302-2577
Timothy Heckman https://orcid.org/0000-0001-6670-6370
Crystal L. Martin https://orcid.org/0000-0001-9189-7818
Dan P. Stark https://orcid.org/0000-0001-6106-5172
Alessandra Aloisi https://orcid.org/0000-0003-4137-882X
Ricardo O. Amorín https://orcid.org/0000-0001-5758-1000
Karla Z. Arellano-Córdova https://orcid.org/0000-0003-2589-762X
Matthew Bayliss https://orcid.org/0000-0003-1074-4807
Rongmon Bordoloi https://orcid.org/0000-0002-3120-7173
Jarle Brinchmann https://orcid.org/0000-0003-4359-8797
Stéphane Charlot https://orcid.org/0000-0003-3458-2275
Jacopo Chevallard https://orcid.org/0000-0002-7636-0534
Ilyse Clark https://orcid.org/0000-0003-3334-4267
Dawn K. Erb https://orcid.org/0000-0001-9714-2758
Anna Feltre https://orcid.org/0000-0001-6865-2871
Max Gronke https://orcid.org/0000-0003-2491-060X
Matthew Hayes https://orcid.org/0000-0001-8587-218X
Alaina Henry https://orcid.org/0000-0002-6586-4446
Svea Hernandez https://orcid.org/0000-0003-4857-8699
Anne Jaskot https://orcid.org/0000-0002-6790-5125
Tucker Jones https://orcid.org/0000-0001-5860-3419
Lisa J. Kewley https://orcid.org/0000-0001-8152-3943
Nimisha Kumari https://orcid.org/0000-0002-5320-2568
Claus Leitherer https://orcid.org/0000-0003-2685-4488
Mario Llerena https://orcid.org/0000-0003-1354-4296
Michael Maseda https://orcid.org/0000-0003-0695-4414
Themiya Nanayakkara https://orcid.org/0000-0003-2804-0648
Masami Ouchi https://orcid.org/0000-0002-1049-6658
Adele Plat https://orcid.org/0000-0003-0390-0656
Richard W. Pogge https://orcid.org/0000-0003-1435-3053
Swara Ravindranath https://orcid.org/0000-0002-5269-6527
Jane R. Rigby https://orcid.org/0000-0002-7627-6551
Ryan Sanders https://orcid.org/0000-0003-4792-9119
Claudia Scarlata https://orcid.org/0000-0002-9136-8876
Peter Senchyna https://orcid.org/0000-0002-9132-6561
Evan D. Skillman https://orcid.org/0000-0003-0605-8732
Charles C. Steidel https://orcid.org/0000-0002-4834-7260
Allison L. Strom https://orcid.org/0000-0001-6369-1636
Yuma Sugahara https://orcid.org/0000-0001-6958-7856
Stephen M. Wilkins https://orcid.org/0000-0003-3903-6935
Aida Wofford https://orcid.org/0000-0001-8289-3428
Xinfeng Xu https://orcid.org/0000-0002-9217-7051

References

Abbott, T. M. C., Adamów, M., & Aguena, M. 2021, ApJS, 255, 20
Adamo, A., Zackrisson, E., Östlin, G., & Hayes, M. 2010, ApJ, 725, 1620
Alam, S., Albareti, F. D., Allende Prieto, C., et al. 2015, ApJS, 219, 12
Arellano-Córdova, K. Z., Berg, D. A., Chisholm, J., et al. 2022, ApJ, in press, (arXiv:2206.04280)
Astropy Collaboration, Price-Whelan, A. M., Sipőcz, B. M., et al. 2018, AJ, 156, 123
Astropy Collaboration, Robitaille, T. P., Tollerud, E. J., et al. 2013, A&A, 558, A33
Berg, D. A., Chisholm, J., Erb, D. K., et al. 2019a, ApJL, 878, L3
Berg, D. A., Chisholm, J., Erb, D. K., et al. 2021, ApJ, 922, 170
Berg, D. A., Erb, D. K., Henry, R. B. C., Skillman, E. D., & McQuinn, K. B. W. 2019b, ApJ, 874, 93
Berg, D. A., Pogge, R. W., Skillman, E. D., et al. 2020, ApJ, 893, 96
Berg, D. A., Skillman, E. D., Croxall, K., et al. 2015, ApJ, 806, 16
Berg, D. A., Skillman, E. D., Marble, A., et al. 2012, ApJ, 754, 98
Bianchi, L., Conti, A., & Shiao, B. 2014, AdSpR, 53, 900
Bordoloi, R., Rigby, J. R., Tumlinson, J., et al. 2016, MNRAS, 458, 1891
Bouché, N., Dekel, A., Genzel, R., et al. 2010, ApJ, 718, 1001
Bradley, L., Sipöcz, B., Robitaille, T., et al. 2021, astropy/photutils: 1.1.0, v1.1.0, Zenodo, doi:10.5281/zenodo.4624996
Brinchmann, J., Charlot, S., White, S. D. M., et al. 2004, MNRAS, 351, 1151
Bruzual, G., & Charlot, S. 2003, MNRAS, 344, 1000
Byler, N., Dalcanton, J. J., Conroy, C., et al. 2018, ApJ, 863, 14
Byler, N., Kewley, L. J., Rigby, J. R., et al. 2020, ApJ, 893, 1
Calzetti, D., Armus, L., Bohlin, R. C., et al. 2000, ApJ, 533, 682
Cardelli, J. A., Clayton, G. C., & Mathis, J. S. 1989, ApJ, 345, 245
Carnall, A. C. 2017, arXiv:1705.05165
Carr, C., Scarlata, C., Henry, A., & Panagia, N. 2021, ApJ, 906, 104
Carr, C., Scarlata, C., Panagia, N., & Henry, A. 2018, ApJ, 860, 143
Chabrier, G. 2003, PASP, 115, 763
Chambers, K. C., Magnier, E. A., Metcalfe, N., et al. 2016, arXiv:1612.05560
Chandar, R., Leitherer, C., & Tremonti, C. 2004, ApJ, 604, 153c
Chang, Y.-Y., van der Wel, A., da Cunha, E., & Rix, H.-W. 2015, ApJS, 219, 8
Charlot, S., & Fall, S. M. 2000, ApJ, 539, 718
Chevallard, J., & Charlot, S. 2016, MNRAS, 462, 1415
Chisholm, J., Gazagnes, S., Schaerer, D., et al. 2018, A&A, 616, A30
Chisholm, J., Rigby, J. R., Bayliss, M., et al. 2019, ApJ, 882, 182
Chisholm, J., Tremonti, C. A., Leitherer, C., et al. 2015, ApJ, 811, 149
Chisholm, J., Tremonti, C. A., Leitherer, C., & Chen, Y. 2017, MNRAS, 469, 4831
Chomiuk, L., & Povich, M. S. 2011, AJ, 142, 197
Curti, M., Mannucci, F., Cresci, G., & Maiolino, R. 2020, MNRAS, 491, 944
Davé, R., Finlator, K., & Oppenheimer, B. D. 2012, MNRAS, 421, 98
de Mello, D. F., Leitherer, C., & Heckman, T. M. 2000, ApJ, 530, 251
Dekel, A., & Silk, J. 1986, ApJ, 303, 39
Dopita, M. A., Kewley, L. J., Heisler, C. A., & Sutherland, R. S. 2000, ApJ, 542, 224
Eisenstein, D. J., Weinberg, D. H., Agol, E., et al. 2011, AJ, 142, 72
Eldridge, J. J., Stanway, E. R., Xiao, L., McClelland, L. A. S., et al. 2017, PASA, 34, e058
Erb, D. K., Quider, A. M., Henry, A. L., & Martin, C. L. 2012, ApJ, 759, 26
Fan, X., Carilli, C. L., & Keating, B. 2006, ARA&A, 44, 415
Feltre, A., Charlot, S., & Gutkin, J. 2016, MNRAS, 456, 3354
Ferland, G. J., Porter, R. L., van Hoof, P. A. M., et al. 2013, RMxAA, 49, 137
Fernandes, I. F., Gruenwald, R., & Viegas, S. M. 2005, MNRAS, 364, 674
Finkelstein, S. L., D'Aloisio, A., Paardekooper, J.-P., et al. 2019, ApJ, 879, 36
Finley, H., Bouché, N., Contini, T., et al. 2017, A&A, 608, A7
Fletcher, T. J., Tang, M., Robertson, B. E., et al. 2019, ApJ, 878, 87
Garnett, D. R. 1992, AJ, 103, 1330
Götberg, Y., de Mink, S. E., Groh, J. H., et al. 2018, A&A, 615, A78
Green, G. 2018, JOSS, 3, 695
Green, G. M., Schlafly, E., Zucker, C., Speagle, J. S., & Finkbeiner, D. 2019, ApJ, 887, 93
Green, G. M., Schlafly, E. F., Finkbeiner, D. P., et al. 2015, ApJ, 810, 25
Grimes, J. P., Heckman, T., Aloisi, A., et al. 2009, ApJS, 181, 272
Gronke, M. 2017, A&A, 608, A139
Gronke, M., Bull, P., & Dijkstra, M. 2015, ApJ, 812, 123
Gronke, M., & Dijkstra, M. 2014, MNRAS, 444, 1095
Gutkin, J., Charlot, S., & Bruzual, G. 2016, MNRAS, 462, 1757
Harshan, A., Gupta, A., Tran, K.-V., et al. 2020, ApJ, 892, 77
Hayes, M., Östlin, G., Atek, H., et al. 2007, MNRAS, 382, 1465
Hayes, M., Östlin, G., Duval, F., et al. 2014, ApJ, 782, 6
Heckman, T. M., Alexandroff, R. M., Borthakur, S., Overzier, R., & Leitherer, C. 2015, ApJ, 809, 147
Heckman, T. M., & Borthakur, S. 2016, ApJ, 822, 9
Heckman, T. M., Borthakur, S., Overzier, R., et al. 2011, ApJ, 730, 5
Henry, A., Scarlata, C., Martin, C. L., & Erb, D. 2015, ApJ, 809, 19
Hill, J. M., Green, R. F., Ashby, D. S., et al. 2010, Proc. SPIE, 7733, 77330C
Izotov, Y. I., Worseck, G., Schaerer, D., et al. 2018, MNRAS, 478, 4851

James, B. L., Berg, D. A., King, T., et al. 2022, ApJ, in press, (arXiv:2206.01224)
James, B. L., Pettini, M., Christensen, L., et al. 2014, MNRAS, 440, 1794
James, B. L., Tsamis, Y. G., Barlow, M. J., et al. 2009, MNRAS, 398, 2
Jaskot, A. E., Dowd, T., Oey, M. S., Scarlata, C., & McKinney, J. 2019, ApJ, 885, 96
Jaskot, A. E., & Ravindranath, S. 2016, ApJ, 833, 136
Jones, T., Stark, D. P., & Ellis, R. S. 2012, ApJ, 751, 51
Kaasinen, M., Bian, F., Groves, B., Kewley, L. J., & Gupta, A. 2017, MNRAS, 465, 3220
Kelly, B. C. 2007, ApJ, 665, 1489
Kennicutt, R. C., & Evans, N. J. 2012, ARA&A, 50, 531
Kennicutt, R. C. J., Lee, J. C., Funes, S. J., et al. 2008, ApJS, 178, 247
Kinney, A. L., Bohlin, R. C., Calzetti, D., Panagia, N., & Wyse, R. F. G. 1993, ApJS, 86, 5
Kluyver, T., Ragan-Kelley, B., Pérez, F., et al. 2016, in Positioning and Power in Academic Publishing, ed. F. Loizides & B. Schmidt (Amsterdam: IOS Press), 87
Kroupa, P., & Weidner, C. 2003, ApJ, 598, 1076
Kulas, K. R., Shapley, A. E., Kollmeier, J. A., et al. 2012, ApJ, 745, 33
Le Fèvre, O., Tasca, L. A. M., Cassata, P., et al. 2015, A&A, 576, A79
Lee, J. C., Gil de Paz, A., Tremonti, C., et al. 2009, ApJ, 706, 599
Leitherer, C., Li, I. H., Calzetti, D., & Heckman, T. M. 2002, ApJS, 140, 303
Leitherer, C., Ortiz Otálvaro, P. A., & Bresolin, F. O. 2010, ApJS, 189, 309
Leitherer, C., Schaerer, D., Goldader, J. D., et al. 1999, ApJS, 123, 3
Leitherer, C., Tremonti, C. A., Heckman, T. M., & Calzetti, D. 2011, AJ, 141, 37
Levesque, E. M., Leitherer, C., Ekstrom, S., Meynet, G., & Schaerer, D. 2012, ApJ, 751, 67
Lineweaver, C. H., Tenorio, L., Smoot, G. F., et al. 1996, ApJ, 470, 38
Lower, S., Narayanan, D., Leja, J., et al. 2020, ApJ, 904, 33
Luridiana, V., Morisset, C., & Shaw, R. A. 2012, in IAU Symp. 283, Planetary Nebulae: An Eye to the Future (Cambridge: Cambridge Univ. Press), 422
Luridiana, V., Morisset, C., & Shaw, R. A. 2015, A&A, 573, A42
Madau, P., & Dickinson, M. 2014, ARA&A, 52, 415
Mannucci, F., Cresci, G., Maiolino, R., Marconi, A., & Gnerucci, A. 2010, MNRAS, 408, 2115
Markwardt, C. B. 2009, in ASP Conf. Ser. 411, Astronomical Data Analysis Software and Systems XVIII, ed. D. A. Bohlender, D. Durand, & P. Dowler (San Francisco, CA: ASP), 251
Martin, C. L. 1999, ApJ, 513, 156
Martin, C. L., Dijkstra, M., Henry, A., et al. 2015, ApJ, 803, 6
Martin, C. L., Shapley, A. E., Coil, A. L., et al. 2012, ApJ, 760, 127
Martin, D. C., Fanson, J., Schiminovich, D., et al. 2005, ApJL, 619, L1
Mason, C. A., Naidu, R. P., Tacchella, S., & Leja, J. 2019, MNRAS, 489, 2669
Mason, C. A., Treu, T., Dijkstra, M., et al. 2018, ApJ, 856, 2
Masters, K. L. 2005, PhD thesis, Cornell Univ.
McGaugh, S. S., Rubin, V. C., & de Blok, W. J. G. 2001, AJ, 122, 2381
McLure, R. J., Pentericci, L., Cimatti, A., et al. 2018, MNRAS, 479, 25
Michel-Dansac, L., Blaizot, J., Garel, T., et al. 2020, A&A, 635, A154
Mingozzi, M., Berg, D. A., Chisholm, J., et al. 2022, ApJ, submitted
Moustakas, J., Kennicutt, R. C. J., Tremonti, C. A., et al. 2010, ApJS, 190, 233
Murray, N., Quataert, E., & Thompson, T. A. 2005, ApJ, 618, 569
Naidu, R. P., Tacchella, S., Mason, C. A., et al. 2020, ApJ, 892, 109
Nakajima, K., Schaerer, D., Le Fèvre, O., et al. 2018, A&A, 612, A94
Nanayakkara, T., Brinchmann, J., Boogaard, L., et al. 2019, A&A, 624, A89
Noeske, K. G., Weiner, B. J., Faber, S. M., et al. 2007, ApJL, 660, L43
Oke, J. B. 1990, AJ, 99, 1621
Olivier, G. M., Berg, D. A., Chisholm, J., et al. 2021, arXiv:2109.06725
Orlitová, I., Verhamme, A., Henry, A., et al. 2018, A&A, 616, A60
Östlin, G., Hayes, M., Duval, F., et al. 2014, ApJ, 797, 11
Ouchi, M., Mobasher, B., Shimasaku, K., et al. 2009, ApJ, 706, 1136
Peeples, M., Tumlinson, J., Fox, A., et al. 2017, The Hubble Spectroscopic Legacy Archive, Instrument Science Report, COS 2017-4
Pogge, R. W., Atwood, B., Brewer, D. F., et al. 2010, Proc. SPIE, 7735, 77350A
Prochaska, J. X., Kasen, D., & Rubin, K. 2011, ApJ, 734, 24
Ravindranath, S., Monroe, T., Jaskot, A., Ferguson, H. C., & Tumlinson, J. 2020, ApJ, 896, 170
Rickards Vaught, R. J., Sandstrom, K. M., & Hunt, L. K. 2021, ApJL, 911, L17
Rigby, J. R., Bayliss, M. B., Gladders, M. D., et al. 2015, ApJL, 814, L6
Rigby, J. R., Bayliss, M. B., Sharon, K., et al. 2018, AJ, 155, 104
Robertson, B. E., Ellis, R. S., Furlanetto, S. R., & Dunlop, J. S. 2015, ApJL, 802, L19
Robertson, B. E., Furlanetto, S. R., Schneider, E., et al. 2013, ApJ, 768, 71
Salim, S., Lee, J. C., Janowiecki, S., et al. 2016, ApJS, 227, 2
Salim, S., Rich, R. M., Charlot, S., et al. 2007, ApJS, 173, 267
Salpeter, E. E. 1955, ApJ, 121, 161
Sanders, R. L., Shapley, A. E., Kriek, M., et al. 2016, ApJ, 816, 23
Savage, B. D., Wakker, B., Jannuzi, B. T., et al. 2000, ApJS, 129, 563
Scarlata, C., & Panagia, N. 2015, ApJ, 801, 43
Schaerer, D., Izotov, Y. I., Nakajima, K., et al. 2018, A&A, 616, L14
Schmidt, K. B., Kerutt, J., Wisotzki, L., et al. 2021, A&A, 654, A80
Senchyna, P., Stark, D. P., Chevallard, J., et al. 2019, MNRAS, 488, 3492
Senchyna, P., Stark, D. P., Vidal-García, A., et al. 2017, MNRAS, 472, 2608
Seyfert, C. K. 1943, ApJ, 97, 28
Shapley, A. E., Steidel, C. C., Pettini, M., & Adelberger, K. L. 2003, ApJ, 588, 65
Shirazi, M., Vegetti, S., Nesvadba, N., et al. 2014, MNRAS, 440, 2201
Steidel, C. C., Bogosavljević, M., Shapley, A. E., et al. 2018, ApJ, 869, 123
Steidel, C. C., Strom, A. L., Pettini, M., et al. 2016, ApJ, 826, 159
Strömgren, B. 1939, ApJ, 89, 526
STScI Development Team, Lim, P. L., Diaz, R. I., & Laidler, V. 2013, pysynphot: Synthetic Photometry Software Package, Astrophysics Source Code Library, ascl:1303.023
Telles, E., Thuan, T. X., Izotov, Y. I., & Carrasco, E. R. 2014, A&A, 561, A64
Thuan, T. X., Izotov, Y. I., & Lipovetsky, V. A. 1996, ApJ, 463, 120
Tinsley, B. M. 1980, FCPh, 5, 287
Tremonti, C. A., Heckman, T. M., Kauffmann, G., et al. 2004, ApJ, 613, 898
Vader, J. P., Frogel, J. A., Terndrup, D. M., & Heisler, C. A. 1993, AJ, 106, 1743
Verhamme, A., Orlitová, I., Schaerer, D., et al. 2017, A&A, 597, A13
Verhamme, A., Orlitová, I., Schaerer, D., & Hayes, M. 2015, A&A, 578, A7
Verhamme, A., Schaerer, D., Atek, H., & Tapken, C. 2008, A&A, 491, 89
Verhamme, A., Schaerer, D., & Maselli, A. 2006, A&A, 460, 397
Vidal-García, A., Charlot, S., Bruzual, G., & Hubeny, I. 2017, MNRAS, 470, 3532
Wang, B., Heckman, T. M., Zhu, G., & Norman, C. A. 2020, ApJ, 894, 149
Whitaker, K. E., Franx, M., Leja, J., et al. 2014, ApJ, 795, 104
Wild, V., Groves, B., Heckman, T., et al. 2011, MNRAS, 410, 1593
Wofford, A., Vidal-García, A., Feltre, A., Chevallard, J., et al. 2021, MNRAS, 500, 2908
Xu, X., Heckman, T., Henry, A., et al. 2022, ApJ, 933, 222
Yates, R. M., Schady, P., Chen, T. W., Schweyer, T., & Wiseman, P. 2020, A&A, 634, A107